Exploring Few-body Scattering Resonances in a Bose-Fermi Mixture: from Feshbach Dimers to Efimov Trimers
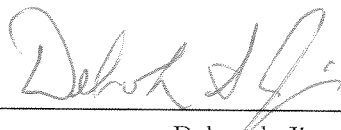
by

Tyler Dunnington Cumby

B.A., Washington State University, 2004

A thesis submitted to the

Faculty of the Graduate School of the

University of Colorado in partial fulfillment

of the requirements for the degree of

Doctor of Philosophy

Department of Physics

2012

This thesis entitled:
Exploring Few-body Scattering Resonances in a Bose-Fermi Mixture: from Feshbach Dimers to
Efimov Trimers
written by Tyler Dunnington Cumby
has been approved for the Department of Physics

_____
Deborah Jin

_____
Eric Cornell

Date __10/5/12__

The final copy of this thesis has been examined by the signatories, and we find that both the
content and the form meet acceptable presentation standards of scholarly work in the above
mentioned discipline.

Cumby, Tyler Dunnington (Ph.D., Physics)

Exploring Few-body Scattering Resonances in a Bose-Fermi Mixture: from Feshbach Dimers to

Efimov Trimers

Thesis directed by Prof. Deborah Jin

This thesis presents experiments exploring Feshbach molecules and Efimov trimers in an ultracold Bose-Fermi atomic gas mixture of ^{40}K and ^{87}Rb. These bound states are accessed via scattering resonances, called Fano-Feshbach resonances, which arise as a consequence of a bound state being tuned through degeneracy with the threshold energy of colliding atoms. In addition to allowing the tunability of interactions, the Fano-Feshbach resonance allows for a weakly bound molecule state, called the Feshbach molecule state, to be populated. The efficiency of conversion to the Feshbach molecule state depends upon the rate with which the bound state energy is swept through degeneracy with atomic threshold energy. In regions of large scattering lengths, three-body bound states, called Efimov states, also influence inelastic Bose-Bose-Fermi collisions and boson+molecule collisions in our system. The work presented in this thesis utilizes a magnetically tunable Fano-Feshbach resonance to study Feshbach molecule creation in the perturbative limit (the limit of fast magnetic-field sweeps) and the saturated limit (the limit of slow sweeps), where a phenomenological model is applied to understand the conversion efficiency as well as the quantum degeneracy of the molecules. In addition, I present a study of boson+molecule collision rates and Bose-Bose-Fermi collision rates in order to observe signatures of Efimov states and compare against results in the gas mixture ^{41}K-^{87}Rb to address the question of universality of the three-body parameter in heteronuclear gas mixtures.

Dedication

To my father, Clifton L. Cumby, 1950-2008.

Acknowledgements

Although the work in this thesis involves the manipulation of atoms at ultralow vacuum pressures, my time here was not spent in a vacuum. During my years here I have had the privilege to work with many excellent scientists. First, I would like to thank my advisor, Debbie Jin, for giving me the opportunity to join one of her labs and be taught how to be an effective physicist. Debbie's labs are also closely associated with Eric Cornell and his labs, and so I've been the benefactor of his questions and thoughtful and thought-provoking insights. When I joined the lab, Michele Olsen was still in the process of rebuilding the experiment after the K sources were depleted. Her efforts produced an apparatus that is still going strong today, albeit with a few upgrades. Along the way a post-doc, John Perreault, joined us and contributed tremendously to the lab with his experimental and theoretical knowledge, as well as his infectious inquisitiveness.

Later John and I were joined by Ruth Shewmon. Ruth has always impressed me with her determined quest to understand the world at large. This drive, coupled with her keen wit, led to numerous insights, both scientific and otherwise (e.g. she once hypothesized that the price of soy milk was driven by the fact that it is quite challenging to milk a soy bean) while we were manning the experiment. Next we had the luck to have Ming-Guang Hu join the lab after he was lured away from Condensed Matter theory to AMO experiment. Our lab benefitted greatly from Ming-Guang's quick wit and remarkable ingenuity. With Ruth and Ming-Guang at the helm of this apparatus, I am confident that many great experiments are in store.

I would be remiss to not thank the many other graduate students that I had the fortune of associating with during my time at JILA. In my early years, I benefited greatly from the friendly

Contents

Chapter

Tables

Table

Figures

Figure

Chapter 1

Introduction

The matter that we interact with in our day-to-day lives (which, as a whole, astoundingly constitutes only 4.6 % [91] of the matter-energy in the universe[1]) can be classified into two categories[2] according to the statistics of the particles. The first class of particles, which possess half-integer spins, obey Fermi-Dirac statistics [58, 44] and are named fermions. Belonging to this class are electrons, protons, neutrons, and all atoms with an odd number of neutrons (e.g. ^{3}He, ^{6}Li, ^{40}K, and ^{87}Sr). A consequence of Fermi-Dirac statistics is that two identical fermions cannot occupy the same quantum state. This restriction, called the Pauli exclusion principle [125], creates a pressure in the system and is responsible for preventing neutron stars from collapsing to a black hole and allowing for chemistry and life as we know it. In contrast, the second class of particles called bosons, obey Bose-Einstein statistics [16, 51, 52], which imposes no such restriction. To this class belong the force-carrying particles such as photons, W bosons, Z bosons, as well as composite bosons (i.e. atoms with an even number of neutrons). Examples of bosonic atoms include ^{4}He, ^{7}Li, ^{23}Na, ^{87}Rb, and ^{133}Cs.

For an ensemble of atoms, the statistics of the atoms only comes to the forefront when the ensemble is cold and sufficiently dense (sufficiently dense for our atom clouds is still 5-6 orders of magnitude less dense than air) such that the extent of the atoms' wavefunctions becomes of order of the interparticle spacing. This criterion is expressed in terms of the phase-space density

---

[1] Discovery and explanation of the remaining 95.4% will be left as an exercise for the reader.
[2] In reduced dimensionalities quasi-particles which do not belong in either category are theorized to exist [97].

defined as $\mathfrak{D} = n\,\lambda_{dB}^3$, where λ_{dB} is the thermal de Broglie wavelength of the atom[3] As the atoms' wavefunctions begin to overlap, the statistics of the particles becomes important as it dictates how the ensemble wavefunction is symmetrized. When the ensemble reaches $\mathfrak{D} \sim 1$, many interesting phenomena are laid bare. For bosons, a macroscopic number of atoms pile into the ground state creating a coherent form of matter know as a Bose-Einstein Condensate (BEC), which was theoretically predicted in 1924 [16, 51, 52] and then realized experimentally in 1995 [3, 31] in ultracold atomic gases. In following years, researchers were able to demonstrate the coherence and long-range correlations of this new form of matter [4] as well as the production of vortices [106] with quantized circulation and shortly thereafter superfluidity in a BEC of a Na atomic gas [118, 131]. These discoveries with weakly interacting BECs further cemented the utility of atomic gas experiments as they were able to delve into idealized aspects of physics of superfluid liquid ^{4}He without the strong interactions inherent in ^{4}He that make it theoretically challenging to describe.

Similarly, atomic Fermi gas experiments showed similar excitement with the production of a degenerate (large value of $\mathfrak{D}$) Fermi gas [34] followed by the creation of degenerate bosonic molecules by binding two fermions together [144, 61], and later the mapping of the BCS-BEC cross-over [133], which is a theory that supplies a possible interpretation for the pseudogap phase in high-Tc superconductors [22]. These early fermion experiments relied upon cooling two spin states of the fermions to ensure that the atoms always have a collision partner and can thermalize. However, another method to cool the fermions emerged: evaporate a bosonic atom gas in contact with the fermionic gas and sympathetically cool the fermionic gas [148, 139]. While the Bose-Fermi mixture was initially another method to create a degenerate Fermi gas, they became interesting in their own right.

---

[3] The thermal de Broglie wavelength [124] is defined as $\lambda_{dB} = \dfrac{h}{\sqrt{2\pi\,m\,k_B T}}$ where h is Planck's constant, m is the atomic mass, k_B is Boltzmann's constant, and T is the temperature of the atoms.
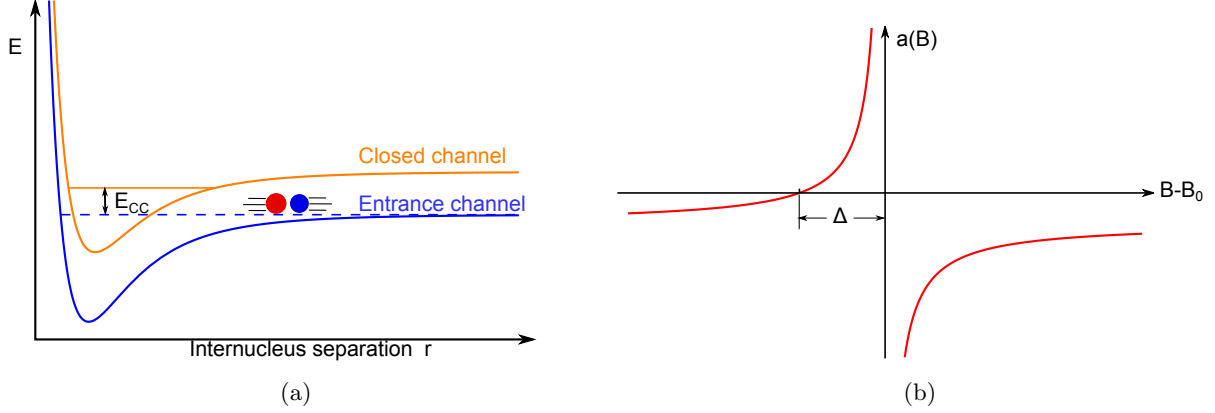
Figure 1.1: a) A simplified model of a Feshbach resonance where atoms colliding in the entrance, or open, channel threshold are brought into degeneracy with a bound state in the closed channel where the energy of the colliding atoms differs from the bound state energy by E_{cc}. b) A plot of the scattering length as a function of magnetic field near a Feshbach resonance located at $B = B_0$. The resonance width is characterized by Δ, which is the difference in magnetic field between the field at which $a = 0$ and B_0.

1.1   Bose-Fermi interactions

Many of the experiments since the first generation of quantum degenerate atom gases have involved the controllable interactions possible in these systems. The source of this novel control are Fano-Feshbach resonances, which are scattering resonances most commonly controlled with a magnetic field. Fano-Feshbach resonances were discovered first in Bose gas systems [78, 26, 154] and later in Fermi gas systems [100, 40, 115, 82] and in ^{40}K – ^{87}Rb Bose-Fermi mixture [79]. These Fano-Feshbach resonances occur when a molecular state (denoted the 'closed channel' in Fig. 1.1a) that can couple to the threshold collision state of the atoms (denoted the 'open channel' in Fig. 1.1a) is tuned into degeneracy with the threshold state. The introduction of a new bound state in the system causes a divergence of the scattering length, which, at ultracold temperatures, is often the sole parameter characterizing the interaction strength between two atoms.

Near a Feshbach resonance, the scattering length has the form $a = a_{bg}[1 - \Delta/(B - B_0)]$ [109] where a_{bg} is the background scattering length (i.e. the scattering length far from resonance), Δ the zero-crossing resonance width, and B_0 is the resonance location. A plot of the scattering length is shown in Fig. 1.1b for $\Delta < 0$ and $a_{bg} < 0$. As can be seen, the scattering length can take positive

and negative values, which correspond to repulsive and attractive interactions, respectively. As the divergence in the scattering length is due to the presence of a molecular state of the appropriate character to interact with the open channel, there is also an associated two-body bound state that can be populated by the atoms from the open channel.

When the search for Feshbach resonances commenced in heteronuclear Bose-Fermi systems, it was noted that with overlapping Feshbach resonances involving the same boson but different fermion states, these systems could emulate boson-mediated Cooper pairing [14, 70, 50]. Additionally, the possibility of producing ground state polar molecules was raised [6, 167, 30], which were ultimately created and spurred a new field of inquiry. However, the first step of the creation of ground-state polar molecules required the creation of Feshbach molecules.

1.1.1 Two-body bound states

The new two-body bound state that appears near a Fano-Feshbach resonance is called the Feshbach molecule state and only exists on the side of the resonance with positive scattering length. Near the Feshbach resonance, the Feshbach molecule has a binding energy $E_d = \hbar^2/2\mu_{2b}a^2$ where μ_{2b} is the reduced mass of the two atoms in the molecule. Feshbach molecules were first generated in Na [169] by sweeping the magnetic field from the negative to the positive scattering length side of the resonance. Feshbach molecules were also created in ^{6}Li [144] and ^{40}K [134], where a Bose-Einstein condensate was formed when starting with a strongly degenerate Fermi atom gas [61]. A phenomenological model (later called the 'Stochastic Phase-Space Sampling' (SPSS) model [164]) was developed to explain the governing physics in molecule formation for adiabatic magnetic field sweeps [75]. The basic assumption was that in order for an atom pair to efficiently associate into a molecule, the atoms would need to be 'close enough' in relative phase space because the adiabatic magnetic field sweep, by its very nature, would not change the occupation in phase space. The cutoff for atoms being 'close enough' was determined by the sole fitting parameter in the model. This model was applied to formation of ^{85}Rb$_2$ Feshbach molecules and ^{40}K$_2$ molecules, where experiments demonstrated that the Feshbach molecule formation efficiency (i.e. the ratio of

molecules to atoms) was governed solely by the phase-space density of the constituent atoms [75]. Furthermore, the fitting parameters for the ^{85}Rb molecules and the ^{40}K molecules agreed, hinting that this model could be applicable also to heteronuclear molecules [75].

Heteronuclear molecules were first created in ^{40}K – ^{87}Rb [119] and later in many other systems as the desire for other polar molecule candidates surged [4] . The SPSS model was applied to ^{85}Rb $-^{87}$Rb [123], ^{40}K – ^{87}Rb [174], and ^{6}Li $-^{40}$K [142] using the parameter values from Ref. [75] and found to accurately describe the molecule creation efficiency in the limit of slow magnetic field sweeps. However, unlike in the homonuclear molecules, the creation efficiency for ^{40}K – ^{87}Rb is quite small for the typical conditions used at the time. An important question was whether or not there was a fundamental limit for fermionic Feshbach molecule creation efficiency and also whether a higher phase-space density of molecules could be made with the available conditions. A separate question was whether the molecule creation efficiency in the perturbative limit(the limit of fast sweeps) followed the predictions developed for single-species gases [25].

1.1.2   Three-body bound states

Two-body bound states are not the end of the story, though. In 1970 Vitaly Efimov predicted, for resonantly interacting systems[5] , that three-body bound states would also exist [48]. Unlike the two-body case, there was predicted to be a semi-infinite ladder of states bounded by the energy corresponding to the length scale of the two-body potential. The three-body bound states also were predicted to remain bound even for negative scattering lengths where the two-body system does not support a bound state. The three-body bound states exhibit a discrete scaling symmetry between the different 'rungs' of the ladder of states (see an example of discrete scaling in Fig. 1.2a). The scattering lengths at which these bound states appear, a_-, demonstrate this scaling through the relation between adjacent bound states $a_-^{(n+1)} = \zeta\, a_-^{(n)}$, where ζ is the scaling factor [48]. The three-body binding energies also exhibit the discrete scaling as seen in Fig. 1.2b, where the solid

---

[4] To date heteronuclear Feshbach molecules have been reported in ^{85}Rb $-^{87}$Rb [123],^{6}Li $-^{40}$K [150, 142] , ^{87}Rb $-^{133}$Cs [146], and ^{23}Na $-^{40}$K [168]

[5] These are systems for which the scattering length is large in magnitude compared to the two-body potential length scale.
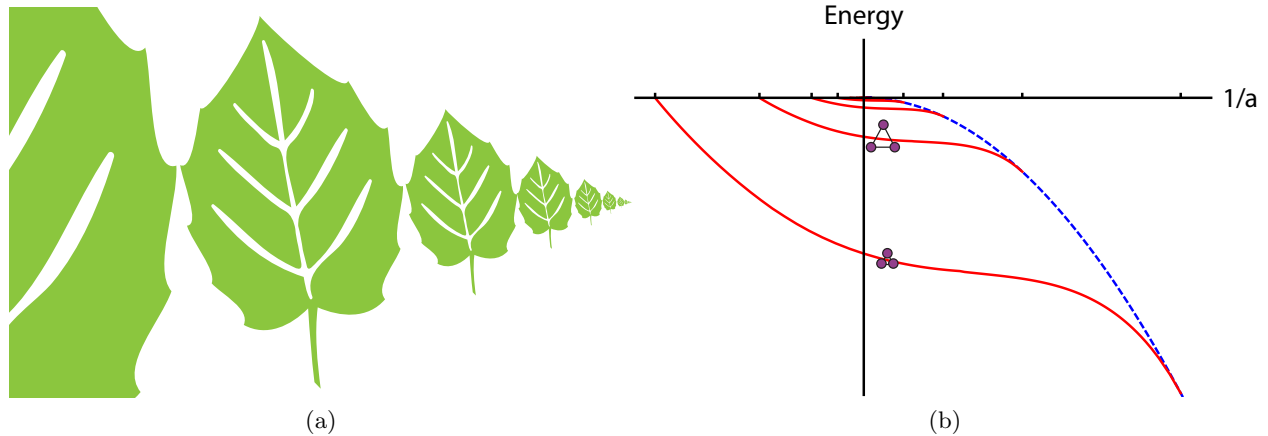
Figure 1.2: a) A series of discretely scaled leaves with a scaling factor of 1/2 between leaves. b) Energy levels for the three-body system shown as a function of the two-body scattering length. The three-body bound states predicted by Efimov are shown as the thick solid curves. The three-body bound states begin at the three-atom collision threshold (Energy = 0) at negative scattering lengths and then asymptotically approaches the atom+molecule threshold given by the molecule energy (dashed line). The scattering lengths at which the three-body states reaches the three-atom threshold are related by a discrete scaling factor, which was artificially chosen to be two for this diagram.

curves are the different trimer states, the dashed line is the two-body bound state energy, and the zero energy level corresponds to the three-atom collision threshold energy.

Although Efimov originally derived this result in the context of bound states within nuclei[6], they were first observed in an ultracold Cs gas system in 2005 [92]. Observation of these trimer states was made from the influence of the trimer states on three-body inelastic collisions: at scattering lengths corresponding to where the trimer binding energies meet the three-atom collision threshold, a_-, there is a resonant enhancement in three-body recombination. Following this was the observation of resonances in a gas of ^{7}Li [64, 129] and in a three spin-state mixture in fermionic ^{6}Li [122, 165, 77]. Efimov resonances were observed in a gas of ^{39}K [170], where the discrete scaling of the Efimov states was confirmed. In ^{6}Li [101] and ^{7}Li [105] the trimer binding energy was directly measured by rf-association into the trimer state and observing the rapid loss.

One looming question in this line of research was 'what sets the location of the lowest Efimov

[6] Specifically three-nucleon bound states within ^{3}H and three α-particle bound states within ^{12}C.

resonance'? Initially it was thought that the three-body parameter, which sets the location of a_-, is a mixture of two-body and three-body physics and is not knowable a priori for a particular atomic system. Experiments in ^{7}Li located Efimov resonances in two different spin states whose locations agreed [66]. Furthermore, in ^{133}Cs, four Efimov resonances were found using a variety of Feshbach resonances (two were a consequence of a g-wave resonance that couples to the s-wave scattering length) [12]. The locations of these four Efimov resonances clustered about a mean value of $a_- = -9.1(4)\, r_{vdW}$ [12] (the van der Waals lengths, r_{vdW}, is the characteristic length scale for the two-body potential) with a spread that was substantially smaller than the scaling factor between different Efimov resonances in the same series [12]. This suggested that the location of the first Efimov resonances were universally determined for broad Feshbach resonances such as those used in ^{133}Cs. The ansatz was made that the location of the first Efimov resonance was universally determined by the length scale of the two-body potential, a view which was corroborated by Efimov resonances in ^{6}Li, ^{85}Rb, and ^{7}Li, where the locations were also close to -9.1 r_{vdW} [23]. Theoretical explanations of this observation soon followed for the case of broad Feshbach resonances [155]. With the observation of Efimov resonances in the heteronuclear Bose-Bose system ^{41}K – ^{87}Rb [7, 8], it is natural to ask the question does a similar universality apply to heteronuclear systems as well.

1.2   Contents of this thesis

In this thesis I address the questions described above with measurements in a ultracold Bose-Fermi mixture of fermionic ^{40}K atoms and bosonic ^{87}Rb atoms.

Chapter 2 discusses the apparatus and the process by which we create the ultracold mixture. Two previous theses discussed this experiment in detail, and so I make the discussion brief, but include discussion of the various upgrades and improved understanding that have happened along the way.

Chapter 3 contains our work on Feshbach molecule creation. Following a short overview of the physics behind Feshbach resonances, I discuss our work to understand molecule creation in the perturbative limit, where the magnetic field is swept quickly through the resonance, and in

the saturated limit, where the magnetic field is swept slowly enough that the molecule number has saturated. Additionally, we look at the expansion energy of the molecules, and the chapter concludes with predictions on how to create molecules with the minimum temperature and T/T_F.

Chapter 4 discusses our efforts to measure Efimov resonances in the ^{40}K – ^{87}Rb system through measurements of inelastic collision rates. In particular, we compare our results with the published ^{41}K – ^{87}Rb resonances and address the question of universality of the three-body parameter in heteronuclear systems. The chapter begins with a overview of the relevant physics and details how we analyze our data to extract the three-body event rate coefficients. Our measurements of three-body recombination do not uncover any Efimov resonances, unlike in ^{41}K – ^{87}Rb, but we do find a feature in Rb+molecule collisions. The chapter concludes with a comparison of the ^{40}K – ^{87}Rb and ^{41}K – ^{87}Rb systems to address possible reasons as to why the Efimov spectra are so strikingly different.

In Chapter 5 I discuss the design and construction of a new Ioffe-Pritchard magnetic trap for our experiment. I discuss basic scaling laws for coils to motivate the coil geometry as well as the various physical restraints imposed on the design by the apparatus. The size of the trap coils was more restricted by the apparatus compared to others in JILA, and so it necessitated using smaller diameter tubing to build the magnets than used previously. This poses the question of whether or not water flow sufficient to cool the magnets is possible, and so I discuss the phenomenological models used to describe fluid flow through helical tubes as well as some sample data to verify the equations. The chapter ends with construction details and other information about the trap.

Chapter 6 ends the thesis with a conclusions and offers possible future directions for the experiment.

Chapter 2

Creating an ultracold Bose-Fermi mixture

While it is often taken for granted in the day-to-day operation of experiments such as this one, it is an amazing feat to be able to catch a cloud of atoms with sufficient isolation from the room-temperature environment to be able to produce a sample so cold and dense that the quantum mechanical nature of the sample is brought to light. Through steady efforts to advance the field technically and scientifically, we, as a field, can delve deeper and explore more complicated phenomena. The subject of this chapter is the process by which we generate our ultracold mixture of bosons and fermions as well as the various improvements we have made to the apparatus along the way. In Sec. 2.1 we discuss the upgraded laser setup, which is an integral part of any modern atomic physics lab. Following in Sec. 2.2, we discuss briefly how our atom clouds are generated and in Sec. 2.3 we discuss how we characterize the performance of our fast magnetic coils system, which we rely upon for the measurements presented in Chapters 3 and 4. The chapter ends with a discussion of a few improvements we have made to our imaging and state control in Sec. 2.4 and a calibration of atom number in Sec. 2.5 using the BEC transition for Rb number calibration, and comparing Rb and K atom numbers in bound molecules to calibrate the K atom number.

2.1 New Rb and K laser setups

Nearly all experiments like this one begin and end with lasers. Diagrams of our setup and frequency locking schemes for K and Rb lasers are shown in Fig. 2.1. The K laser system has been revamped since Michele Olsen's thesis [116] to eliminate the need for the K trap slave laser, which

was run at $-40°$C, and to replace the K trap master, which was run at $-10°$C. The K slave laser was particularly painful to use because of the need to warm the laser up to room temperature to clean out ice and then cool the laser back down slowly such that the diode does not stress fracture. In their stead, we have a K trap External Cavity Diode Laser (ECDL) and a K repump ECDL, which both use the AR-coated diode from Eagleyard (EYP-RWE-0790-04000-0750-SOT01-0000). These two lasers supply the power to directly inject the K tapered amplifier (K TA in Fig. 2.1, Eagleyard EYP-TPA-0765-01500-3006-CMT03-0000) as well as for the various probe and optical pumping beams. We find that the K repump to trap power ratio for the MOT needs to be at least 1:2. This is in rough agreement with what one would expect from off resonant transitions to other excited states due to the trap laser. We run these lasers at a balmy $17°$C, which is both below the room temperature and above the dew point of the majority of the year. Although these lasers are a definite improvement over the old setup, their mode-hop free tuning range does degrade over the time scale of a few years. This seems to indicate that the AR coating on the diodes degrades for K frequencies, which is a view supported by the manufacturer.

The Rb laser system has been partially upgraded as well with the replacement of the Rb trap master with a laser that uses the same AR coated diode as the K lasers[1] . The Rb trap master supplies the power for the optical pumping and probing (including the new Rb high B imaging system with the 400 MHz double-passed AOM (Brimrose TEF-400-100-.780) in place of the triple pass system [116]) as well as injection locking the Rb slave laser. The Rb slave laser, in turn injects the Rb tapered amplifier (Rb TA in Fig. 2.1). The other new laser in the setup is the Rb repump DBR (Distributed Bragg Reflector) from Photodigm (PH780DBR). Over the several months of use we have had from this laser, it has proven to be remarkably robust and rarely falls out of lock[2] .

---

[1] The mode-hop free tuning range of this laser curiously does not degrade as do the K trap and repump lasers.

[2] This stability is due in part to the feedback the diode receives from the Bragg grating built into the diode structure itself. However, we find that the laser requires at least 60 dB of optical isolation to block light that travels back to the laser from the TA and various reflections
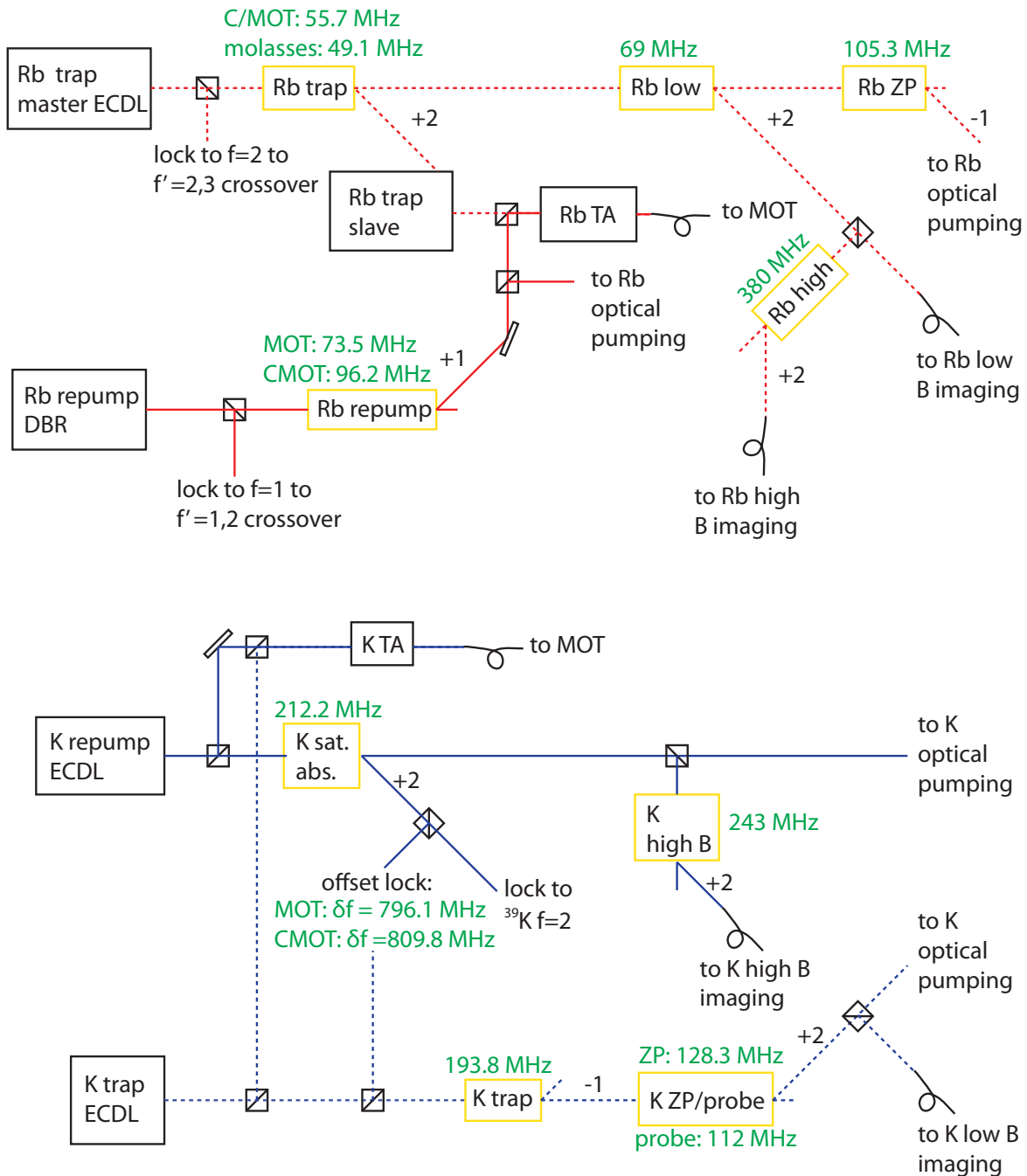
Figure 2.1: Diagrams of Rb and K laser setup and locking scheme. Light is supplied by the various lasers and tapered amplifiers (TA) and the light frequencies are shifted by acousto-optic modulators (AOM)(yellow squares). All of the light for the MOT and all probe beams are coupled into optical fibers (black loops) to be sent to the apparatus, whereas the optical pumping beams are propagated through free-space. Frequencies for the AOMs and the offset lock are shown for the various stages of the experiment.

2.2   Bose-Fermi mixture: onward and downward to the ultracold regime

The details of how we generate an ultracold Bose-Fermi mixture from the atomic vapor in our vacuum chamber is discussed in John Goldwin's thesis [60] and Michele Olsen's thesis [116], and so are only briefly summarized here. A CAD rendering of the apparatus is shown in Fig. 2.2. The experiment begins by slowing a portion of the atomic vapor in the collection cell using a magneto-optical trap. The atomic vapor comes from a commercial Rb alkali dispenser and a home-made K alkali dispenser [35] (the two 'rabbit ears' on the collection cell) wherein an electrical current drives a redox reaction which in turn releases alkali into the collection cell. The MOT is able to capture $\sim 10^9$ Rb atoms and $\sim 1.4 \times 10^8$ K atoms, with the higher power produced by the K TA (¿100 mW after fiber coupling), compared to $\sim 5 \times 10^7$ with the old K slave laser ($\approx$40 mW after fiber coupling).

The next stage involves loading the atom clouds into the Quadrupole trap (Q-pole trap), whose coils are the same as used to supply the magnetic-field gradient for the MOT. In order to reduce the amount of potential energy the atoms would gain from the load into the Q-pole trap, we must reduce the sizes of the Rb and K clouds before releasing the MOT. The Rb cloud is compressed by reducing the radiation pressure due to radiation trapping of the trap light. This is accomplished by allowing Rb atoms to go 'dark' to the trap light by reducing the intensity of the repump light as well as detuning the repump light further from resonance. Following the release from the MOT is a stage of Doppler cooling for K, a stage of molasses cooling for Rb, and then optical pumping to pump Rb into the $|2, 2\rangle$ state and K into the $|9/2, 9/2\rangle$ state. The atoms are then loaded into the nearly full-strength Q-pole trap (147 G/cm in direction perpendicular to the plane of the coils), whose coils are mounted on a movable cart. The cart is attached to a motor-driven linear positioning stage whose motion is governed by Aerotech's Soloist HLe 10-60-A controller [3]. The cart transports the Q-pole trap to the science cell in 1.25 s for the roughly 1 m of travel.

---

[3] This new controller has a linear power supply to drive the motor, as well as optically isolated inputs. Whereas the old cart controller nearly brought the experiment to its knees due to the amount of rf it polluted the lab with, this new controller is whisper quiet in the rf.

TOP VIEW

Science cell

Q-pole trap coils

Collection cell

Cart track
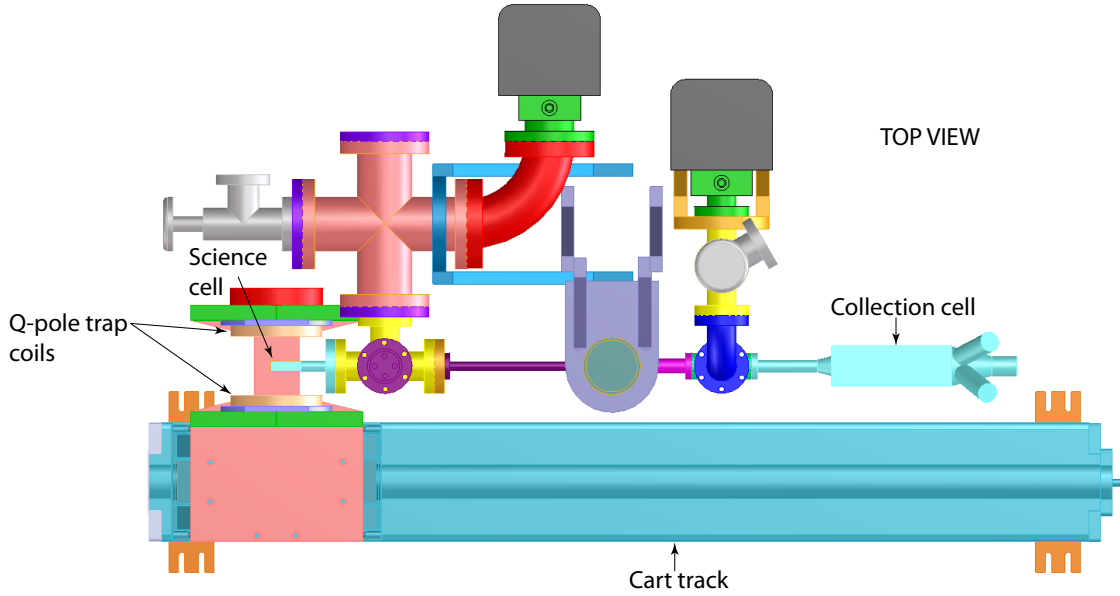
Figure 2.2: CAD rendering of the apparatus without the Ioffe-Pritchard trap (IP trap), which surrounds the science cell. At the start of an experiment, the Quadrupole-trap coils (Q-pole trap) are located at the collection cell where they supply the magnetic-field gradient for the MOT. After the MOT stage, the atom clouds are compressed and cooled and then loaded into the Q-pole trap. The Q-pole trap coils are mounted on a movable cart (cart track is 1.2 m long) which whisks them away to the science cell where the atoms are loaded into the IP trap for further cooling.

Before the atoms enter the science cell, the magnetic-field gradient is lowered to 29 G/cm (30.6 G/cm is necessary to support $|2, 1\rangle$ and $|1, -1\rangle$ atoms at rest) for 200 ms to spin purify the clouds such that only the Rb atoms in the $|2, 2\rangle$ state are supported against gravity; K in the $|9/2, -9/2\rangle$, $|9/2, -7/2\rangle$ states also remain trapped.

Once in the science cell, the atoms are transferred into a Ioffe-Pritchard [80, 130] magnetic trap in which the bulk of the cooling is performed. In this trap, the Rb is cooled by forced rf evaporation and K is cooled sympathetically through collisions with Rb. The process begins with 5×10^8 Rb atoms and 4×10^6 K atoms[4] at 600 μK and ends with $1 - 2 \times 10^6$ atoms of each species at 1 μK ($f_{\text{radial}} = 122$ Hz, $f_{\text{axial}} = 25$ Hz). Since the atomic spin states that are needed for the work

---

[4] Because of the low density of K atoms, it is difficult to measure the K atom number at early stages in our experiment; this number is based on what is measured after the evaporation has commenced.

described in Chapters 3 and 4 are not able to be trapped magnetically, the atoms are transferred to an far off-resonance trap (FORT), which, by the nature of the large detuning from the atomic transitions, is insensitive to the hyperfine state of the atom. This trap is formed from the focus (waist = 22 μm) of a single beam from a laser that produces light at 1090 nm (SPI SP-10C). To load the atoms into the FORT, the IP trap current is slowly ramped off in 100 ms after the FORT is at its full load strength. This new loading procedure results in substantially less heating than the old procedure where the IP trap was abruptly shut off[5] . Next, Rb and K are transferred into the $|1,1\rangle$ and $|9/2, -9/2\rangle$ spin states via adiabatic rapid passage (ARP) pulse sequences discussed below in Sec. 2.3. The atoms then undergo the last stage of cooling as the large bias field [6] ramps close to the field needed for the work described in Chapters 3 and 4. To further cool the atoms, the FORT power is lowered, allowing hot atoms to spill out of the trap. To bias the evaporation towards losing more Rb in order to preserve as much K in the FORT as possible, a small magnetic-field curvature (from the pinch coils of the IP trap) is added that preferentially enhances the trapping frequency, and thus trap depth, of K compared to Rb, which in $|1,1\rangle$ has half the magnetic moment that K in the $|9/2, -9/2\rangle$ state possesses. At the end of the evaporation, the FORT power is ramped up by a factor of ~ 2 to ensure that the atom temperature is not at the trap depth. This results in a sample of several 10^5 of each species at 200-500 nK in a trap with axial and radial trap frequencies of 5 Hz and 420 Hz, for Rb, and 6 Hz and 550 Hz for K.

2.3   Characterizing the Fast B coil circuit time response

The next stage of our experiment utilizes a low inductance coil pair, called the *Fast B* coils, to rapidly change the magnetic field on microsecond to tens of milliseconds time scales. The Fast B system is integral to the experiments detailed in Chapters 3 and 4, which required the ability to rapidly sweep the magnetic field through a magnetically-tunable scattering resonance, known as a

---

[5] Previously atoms were heated all the way to the trap depth (4 μK) with the old loading procedure. By ramping the IP trap off slowly, the load temperature is 2.3 μK, which is nearly what one would expect due to adiabatic compression alone (1.8 μK).

[6] This field is provided by the Q-pole trap coils with one of the coils having its current direction switched.

(a)   (b)
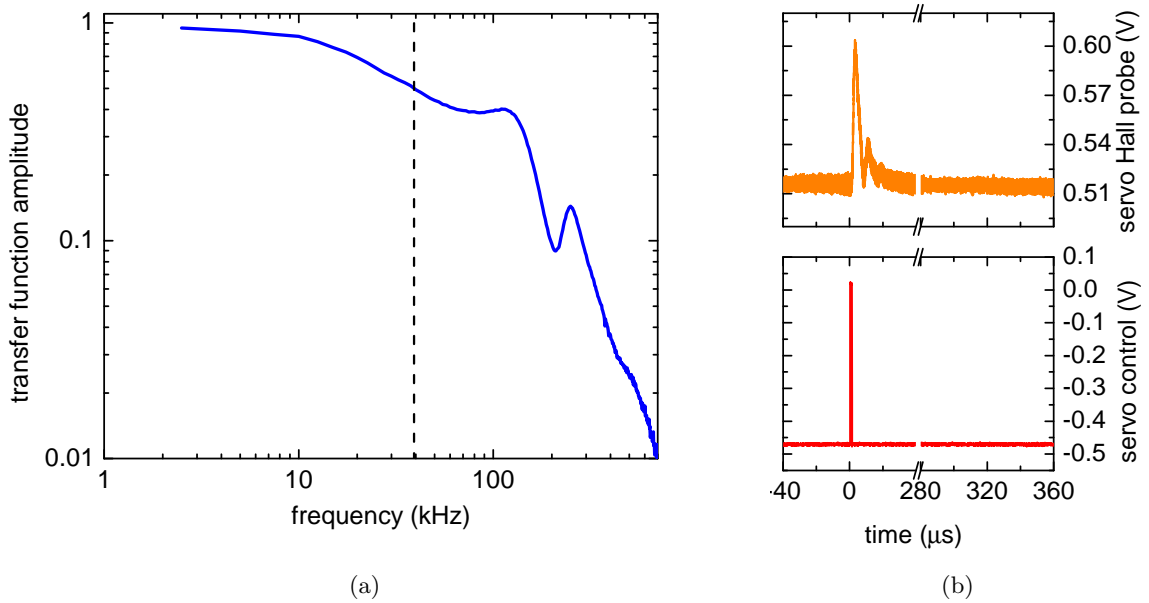
Figure 2.3: a) Calculated closed-loop transfer function for the Fast B servo from measurements of the input waveform and measured response. The bandwidth of the servo, as measured by the -3dB frequency, is 39.2 kHz (dashed line). The peaks in the transfer function are likely resonances in our Hall-effect current transducers (LEM Ultrastab-866). b) Measured servo control voltage (lower plot, denoted f(t) below) and servo Hall-effect current transducer (upper plot, denoted g(t) below). Both plots have been undersampled from the actual data by a factor of 100. Note that the servo's small response compared to the control voltage is a signature of its limited bandwidth.

Fano-Feshbach resonance [78]. Our system has the added complication of strong eddy fields (with decay times of order 1 ms) due to the copper cooling blocks onto which the IP trap and Fast B coils are epoxied [7] . The details of our open-loop compensation of these eddy fields are provided in Michele Olsen's thesis [116]. In view of these requirements and constraints, we need to thoroughly characterize how well the Fast B system performs.

2.3.1   Fast B closed-loop transfer function

The first step is to characterize how the full Fast B system (i.e. the servo electronics and high-current path) responds to time-varying control signals. This response is more often analyzed

---

[7] Although the cooling blocks do have slots that cut into them to stave off the largest eddy current paths, the amount of copper left unobstructed is sufficient to be a problem.

in the frequency domain by measuring the transfer function for the system [96]. The transfer function, H, is defined as the impulse-response function for a system (in Physics parlance this is a Green's function for the system). Suppose we input a time varying function f(t) to our system and measure its response, g(t). The output is the convolution of f(t) with our transfer function, H. In the frequency domain the input and output functions can be related using linear response theory. The relation between the input and output is

$$\tilde{g}(\omega) = H(\omega)\tilde{f}(\omega) \tag{2.3.1}$$

where $\tilde{g}(\omega)$ and $\tilde{f}(\omega)$ are the Fourier transforms of g(t) and f(t), respectively. Therefore the system can be characterized by measuring input and output response and then numerically calculating $H(\omega) = \dfrac{\tilde{g}(\omega)}{\tilde{f}(\omega)}$. We can perform this measurement in either a spectrally narrow manner where f(t) $=\sin(\omega_0 t)$ and $\tilde{f}(\omega) \propto \delta(\omega - \omega_0) - \delta(\omega - \omega_0)$ and map out the response versus frequency or in a spectrally broad manner[8] with f(t) $=\delta(t)$ and $\tilde{f}(\omega) \propto 1$.

Shown in Fig. 2.3a is the amplitude of our closed-loop transfer function calculated from measured servo input signal and servo Hall-effect current transducer (Hall probe) output shown in Fig. 2.3b. For values of the transfer function amplitude near unity, the servo is able to faithfully reproduce the control signal. The -3dB frequency, which is a measurement of the system bandwidth, is $f_{-3dB} = 39.2$ kHz. The transfer function amplitude also exhibits two peaks, which are likely due to resonances in the Hall probe that is used to measure the current.

2.3.2   Measuring the Fast B magnetic-field sweep rate in situ

Now that we have a good measurement of how the Fast B system performs, we need to measure the limit on how fast we can sweep the magnetic field. To measure the sweep rate we

---

[8] A true δ function cannot realized and in reality the output is more correctly a Heaviside Π function f(t) = $\Pi(at)$ (width of the pulse is $1/a$) such that $\tilde{f}(\omega) \propto \text{sinc}(\omega/a)$. The function $\text{sinc}(\omega/a)$ sports zeros at $\omega = 2\pi n a$, for n $= 1, 2, 3, \ldots$, and so the spectral width is limited to $\omega = 2\pi a$. At this point the calculated transfer function could exhibit numerical instabilities as we are dividing by zero and so the pulse length should be short compared to any frequencies of interest in the system. For the data shown in Fig. 2.3 a 1 μs pulse was used, which limits the measurement to frequencies below 1000 kHz. In this regard, driving the system with a step function might be a better input waveform as its Fourier transform does not have any finite zeros.

rely on our atoms for the magnetometery signal by using the magnetically-sensitive $|F, m_F\rangle =$ $|9/2, -9/2\rangle \rightarrow |9/2, -7/2\rangle$ transition in K and looking at the adiabaticity of a Landau-Zener sweep.

By applying rf resonant with this transition at a given field, the $|9/2, -9/2\rangle$ and $|9/2, -7/2\rangle$ states are coupled together and the true eigenstates of the system then exhibit a Landau-Zener avoided-crossing [172]. This problem is a classic two-level problem with a Hamiltonian given by

$$H = \begin{pmatrix} \epsilon_1 & \hbar\Omega/2 \\ \hbar\Omega/2 & \epsilon_2 \end{pmatrix} \tag{2.3.2}$$

where Ω is the on-resonance Rabi frequency, ϵ_i is the energy of the bare (uncoupled) state i. With the applied rf, the eigenenergies of this Hamiltonian are no longer that of the bare state energies, and are given by

$$E_\pm = \frac{\epsilon_1 + \epsilon_2}{2} \pm \frac{1}{2}\sqrt{(\epsilon_1 - \epsilon_2)^2 + (\hbar\Omega)^2}. \tag{2.3.3}$$

A diagram of the coupled system is shown in Fig. 2.4a where we have assumed that ϵ_1 from Eqn. (2.3.2) varies linearly with magnetic field with an assumed value for Ω. In this diagram, the bare states ϵ_1 and ϵ_2 (dashed lines) represent the uncoupled $|9/2, -9/2\rangle$ and $|9/2, -7/2\rangle$ states. With the application of rf resonant with the $|9/2, -9/2\rangle \rightarrow |9/2, -7/2\rangle$ transition at B_0, the two states become coupled and the eigenstates of the system are E_+ and E_- (solid curves). If we begin with the magnetic field infinitely far away from B_0, where the bare states and eigenstates are identical, and with the system initialized in ϵ_2, for example, then as we ramp the magnetic field slowly down through B_0, then the system will adiabatically follow E_- ultimately ending with the system transferred to state ϵ_1 once the magnetic field is infinitely far from B_0. This process is known as Adiabatic Rapid Passage (ARP). If the ramp is not slow, then the system with end as a mixture of atoms in E_+ and E_-. The probability of the system undergoing a transition between
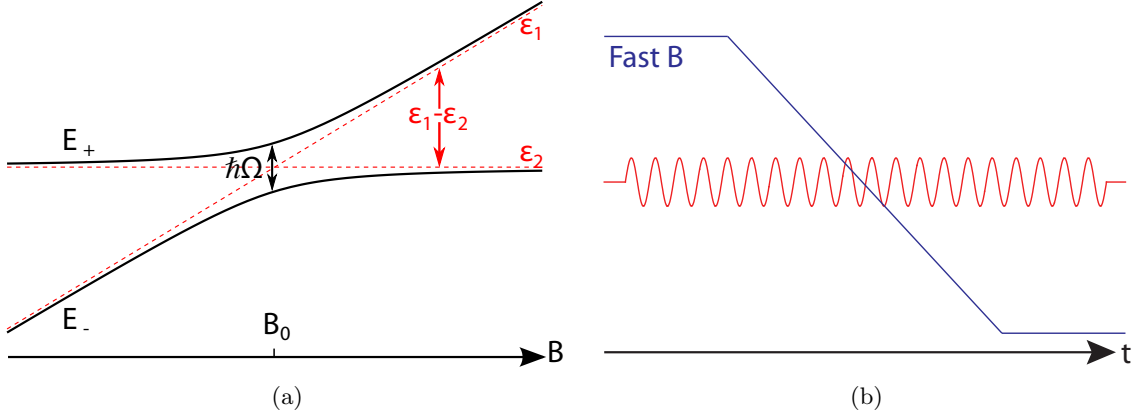
Figure 2.4: a) Energy diagram for a coupled two-level system as discussed in the text. b) Timing diagram for a magnetic field ARP where the rf (red sinusoidal curve) is turned on while the magnetic field is initially far from resonance and the magnetic field later sweeps linearly down through the resonance.

E_- and E_+ as the magnetic field transits through B_0 is [172]

$$P_{1\to 2} = \exp\left(-\frac{\pi}{2} \frac{\hbar\Omega^2}{|\frac{d}{dt}(\epsilon_1 - \epsilon_2)|}\right)$$
$$= \exp\left(-\frac{\pi}{2} \frac{\hbar\Omega^2}{|\delta\mu\frac{dB}{dt}|}\right) \tag{2.3.4}$$

where $\delta\mu$ is the magnetic-moment difference between states ϵ_1 and ϵ_2. The Rabi frequency is proportional to a dipole matrix element, and so Ω^2 is proportional to the rf power.

To measure the sweep rate, we begin with a polarized sample of K in the $|9/2, -9/2\rangle$ state with the magnetic field 5 G away from field at which the rf is resonant. Since we are most concerned with the ramp rate at the center, we fix the rf frequency to be resonant with the $|9/2, -9/2\rangle \to |9/2, -7/2\rangle$ transition at this field. As shown in Fig. 2.4b, we perform the magnetic field ARP by applying the rf at a constant frequency and sweeping the magnetic field, after which we measure the remnant $|9/2, -9/2\rangle$ population. These measurements were performed at fields near 550 G where the imaging transition for the $|9/2, -7/2\rangle$ is roughly 13 natural line-widths detuned from the probe light for the $|9/2, -9/2\rangle$ imaging. As a consequence the atoms in the $|9/2, -7/2\rangle$ do not create a significant imaging background. The magnetic-field sweep rate can be measured by performing the same field sweep for various rf powers and independently measuring the Rabi frequency for each

power from on-resonance Rabi flopping. An example of such a field ARP measurement is shown in Fig. 2.5c for an inverse field sweep rate of 10 μs/G for a ramp that spans 10 G. For this data, the current ramp sent to the Fast B servo includes an eddy current correction. The data were fit to an decaying exponential of the form $N = N_0 \exp(-p/p_{1/e}) + y_0$. From the fitted value of $p_{1/e}$ and Eqn. (2.3.2), the magnetic-sweep rate is measured, where $\delta\mu = h \times 66$kHz/G near 550 G. Fig. 2.5d shows the fidelity of our Fast B system for a small range of sweep rates, showing that we can trust inverse sweep rates as low as 3 μs/G.

2.4 Imaging and state control improvements

The last stage of the experiment involves imaging the atoms, and perhaps molecules, using standard absorption imaging. This process, although simple in principle, requires careful calibration of experimental parameters and is also subject to various systematic errors [135, 98, 15]. In this Section I focus on the various systematic effects in order to understand how well we know our atom number and I include discussion of various improvements to apparatus.

To take an image, the gas of atoms and molecules is released from the optical trap and allowed to expand. We take an image of the atoms[9] by shining a probe beam resonant with either the $|9/2, -9/2\rangle \rightarrow |11/2', -11/2\rangle$ transition when imaging K, or the $|2, 2\rangle \rightarrow |3', 3\rangle$ transition when imaging Rb[10] . The atoms absorb light from the probe beam casting a shadow onto the camera which records the image. Additionally, we take an image of the intensity profile without atoms and an image of the dark counts on the camera when no probe beam is applied. From these images we calculate the optical depth of the cloud at each pixel from $OD = \ln \frac{I_L - I_D}{I_S - I_D}$ where I_L, I_S, and I_D are the intensities of the light image, the shadow image, and the dark image, respectively. The optical depth of the cloud is proportional to the column density (i.e. the result integrating the full three-dimensional density through the probe direction) [107], and from the cloud sizes and column density

---

[9] Molecules are imaged by first dissociating the molecules and then imaging their constituent atoms. This requires that we remove unpaired atoms of the type we will be imaging in the molecules. If we image the dissociated K atoms, we first shift the unpaired K atoms into the $|9/2, -7/2\rangle$ state. Imaging of dissociated Rb involves shifting unpaired Rb into $|2, 2\rangle$ and then blasting them away with light resonant with $|2, 2\rangle \rightarrow |3', 3\rangle$.

[10] This requires that we transfer Rb atoms from $|1, 1\rangle$ to $|2, 2\rangle$, which is achieved with a microwave ARP.

(a)

(b)

(c)

(d)
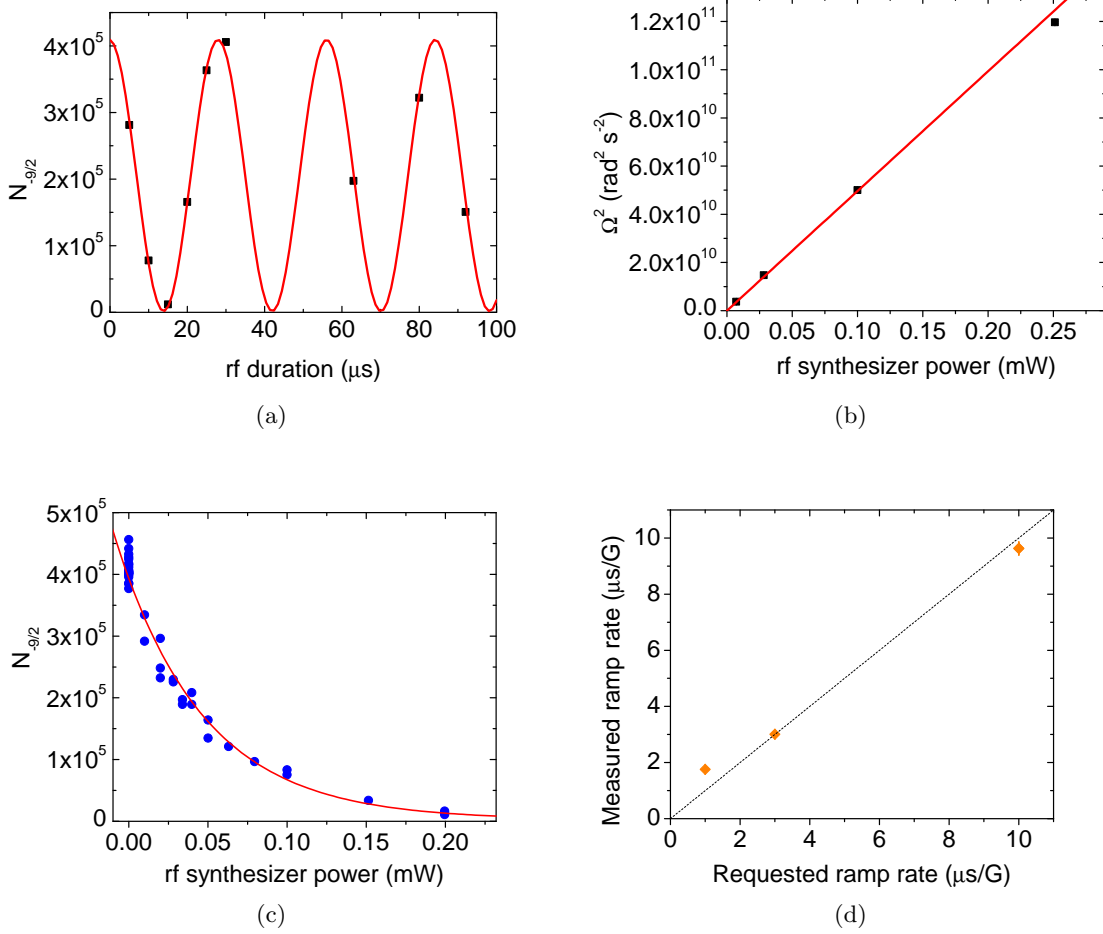
Figure 2.5: a) On resonance Rabi flopping between $|9/2, -9/2\rangle$ and $|9/2, -7/2\rangle$ at a synthesizer power of 0.1 mW and an rf frequency of 80.0378 MHz. b) Calibration of the Rabi frequency versus synthesizer power. The fit of Ω^2 versus power to a line returns a slope of $4.97(13) \times 10^{11}\text{rad}^2\,\text{s}^{-2}\,\text{mW}^{-1}$. c) Sample measurement of the 10 μs/G ramp with a 10 G span. The number of atoms remaining in the $|9/2, -9/2\rangle$ Zeeman state are plotted as a function of the rf synthesizer power and then fit to an decaying exponential of the form $N = N_0 \exp(-p/p_{1/e}) + y_0$. From the fitted value of $p_{1/e}$ and Eqn. (2.3.2), the magnetic-sweep rate is measured, where $\delta\mu = h \times 66\text{kHz/G}$ near 550 G. d) Collection of measurements such as c) plotted against the inverse ramp rate requested of the servo and a line with a slope of 1. The measured ramp rate was calculated from c) using a calibration of the Rabi frequency measured from Rabi flopping.

we can calculate the atom number and temperature, as well as other thermodynamic quantities [33].

There are various systematic errors that impact the number extracted from an absorption image. Here I discuss two systematic effects due to stray light in the image and intensity saturation

(a)   (b)
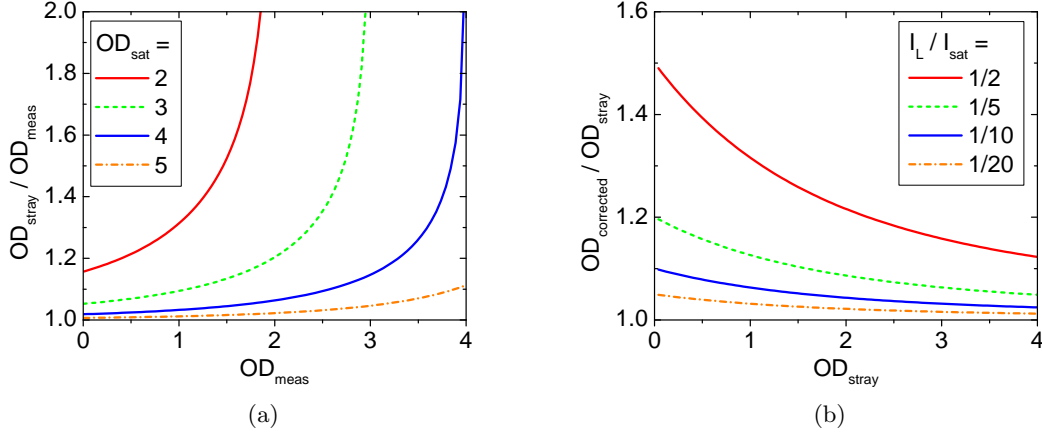
Figure 2.6: a) Fractional correction of the measured OD (OD_{meas}) due to OD saturation effects caused by unabsorbed light. b) Fractional correction of the OD_{stray} due to intensity saturation effects.

of the probe transition. First let's consider the situation where a portion of the probe light is not absorbed by the atoms, either because it has the wrong frequency or polarization to be absorbed, or the light simply scatters off of some structure in the vacuum chamber and hits the camera. The measured optical depth is then

$$OD_{meas} = \ln \frac{I_L + I_{NA}}{I_S + I_{NA}} \qquad (2.4.1)$$

where we have ignored the dark image for simplicity and I_{NA} is the intensity of the unabsorbed light. The amount of unabsorbed light imposes an upper limit on the OD_{meas}, denoted OD_{sat}, given by

$$OD_{sat} = \ln \frac{I_L + I_{NA}}{I_{NA}}. \qquad (2.4.2)$$

This OD saturation can severely distort the imaged profile of dense samples, but also causes one to underestimate the atom density and number. The significance of this effect can be determined by solving Eqn. (2.4.1) for the true optical depth [98], which results in

$$OD_{stray} = \ln \frac{1 - e^{-OD_{sat}}}{e^{-OD_{meas}} - e^{-OD_{sat}}}, \qquad (2.4.3)$$

where OD_{stray} represents the OD after correcting for the effects of stray, or un-absorbed, light. Fig. 2.6a consists of plots of Eqn. (2.4.3) divided by OD_{meas} for various values of OD_{sat}. For
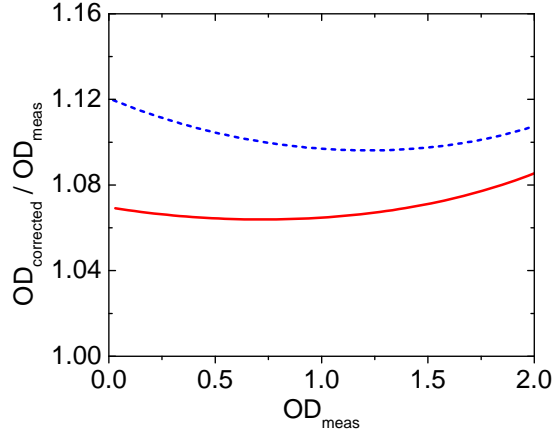
Figure 2.7: Plot of Eqn. (2.4.4) using Eqn. (2.4.3) for $OD_{sat} = 4$ and $\frac{I_L}{I_{sat}} = 1/10$ (dashed line) and $\frac{I_L}{I_{sat}} = 1/20$ (solid line).

small values of OD_{sat} the correction for the OD is significant [11] and so it is desirable to eliminate sources of unabsorbed light. After upgrading our imaging system with higher quality polarizing beam splitter cubes and waveplates from CVI, our OD_{sat} increased to $OD_{sat} = 4$ from 3.

An additional correction is a consequence of saturation of the probe transition due to high probe intensity. After integrating the Beer-Lambert law [107], the corrected OD is

$$OD_{corrected} = OD_{stray} + (1 - e^{-OD_{stray}})\frac{I_L}{I_{sat}} \qquad (2.4.4)$$

under the assumption that the probe laser is on resonance with the atomic transition with I_{sat} denoting the saturation intensity for the probe transition[12] . Fig. 2.6b shows the extent of this correction for various values of I_L/I_{sat}. In most circumstances it is advisable to image with $I_L/I_{sat} \leq$ 1/10. Fig. 2.7 shows the combination of these two systematic effects assuming $OD_{sat} = 4$ for our typical range of $\frac{I_L}{I_{sat}} = 1/10$ (dashed line) to 1/20 (solid line). For the range of OD we typically measure (OD = 0.2 to 1.5) these corrections imply that our measured OD is low by 7% to 11 %.

---

[11] In the limit of low OD, the ratio $OD_{stray}/OD_{meas} = \dfrac{1}{1 - e^{-ODsat}}$.

[12] The low OD limit for $OD_{corrected}/OD_{stray} = 1 + \dfrac{I_L}{I_{sat}}$.

2.4.1 Measuring imaging magnification

Since an accurate measurement of the atom number relies on knowing the physical size of the cloud in the OD image, we need an accurate and precise measure of the imaging system's magnification. Previously, we had relied upon mapping the position of a falling cloud as a function of time to calibrate the magnification, but this is complicated by the magnetic curvatures present while our clouds drop. Efforts were also made to measure the magnification from a knife-edge diffraction pattern, but results between different probe beams were inconsistent, which hinted that the measurement was being influenced by the phase curvature of the beams. The method which gave the best result, which also agreed with our model of the optics, was suggested to us by a visiting scientist in the Cornell labs. It was to image a commercial resolution target onto the camera. After the camera was focused onto the atom clouds, the test target (Melles Griot 04 TRP 003) was back lit with a halogen lamp. The image was projected through our optics setup with an added mirror and onto the camera. A 780nm notch filter was placed on the camera to block the broad spectrum of the halogen lamp and thus avoid having to correct for the dispersion of the achromatic lenses in the imaging system. A sample image is shown in Fig. 2.8 from which we extract a magnification of M = 2.51(3) using the manufacturer's measurements of the line spacing[13] . The error bar in the measured magnification is due to the width of the edges of the features. The magnification measured from the test target agrees with magnification measured from watching Rb atoms in the $|2, 0\rangle$ state fall at low fields (M = 2.49(3)).

2.4.2 The new and nimble Rb microwave setup

For some of the work described in Chapter 4, we needed to be able to quickly shuttle Rb atoms to different hyperfine states at multiple fields in rapid succession using ARPs. The microwave synthesizer we use (Agilent E8251A) is programmed over GPIB and so takes of order 100 ms to reprogram the center frequency of a frequency sweep. Additionally, the center frequency difference at the different fields was large enough that it could not be accommodated by increasing the

---

[13] This test target has the standardized USAF 1951 resolution target pattern
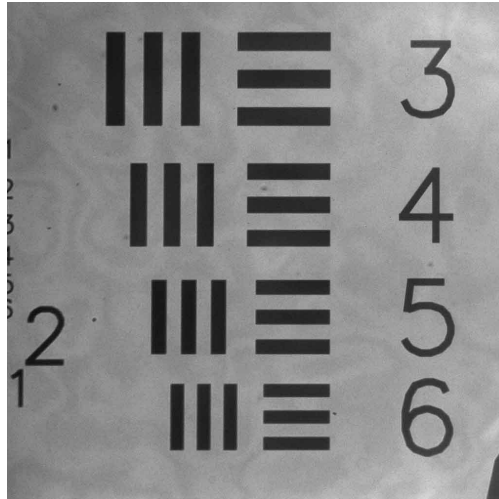
Figure 2.8: Sample image of the back-lit test target taken using our imaging system.

frequency span of the ARP. What was needed was a more nimble microwave system.

Our solution to this was to mix our microwave source with a Direct Digital Synthesizer (DDS), as shown in Fig. 2.9. This DDS (Toptica VFG-150) can be programmed with multiple rf pulse sequences and rapidly triggered between them and so performs the nimble tasks needed of the system. The microwave and rf are mixed with using a single-sideband mixer (Marki Microwave SSB-0618LXW-1) for which one frequency sideband is suppressed by 23dB through destructive interference. The microwaves then pass through a microwave solid-state switch (Narda SP123DHTS) and then through a high-power microwave amplifer (AML L0608-41-T479, -1 dB compression point at 41 dBm=12.5 W). Lastly, the microwaves pass through an isolator and then to a doubly stub-tuned microwave antenna (resonant at 6.8 GHz and 8 GHz) that was built in-house and tuned in situ. The system operates with the carrier (supplied by the E8251A) far detuned and allows us to perform some additional checks on K number calibration discussed below. With this new microwave setup we can switch frequencies as fast as 100 ns according to the manufacturer, which is substantially faster than our typical ARP durations of 100 μs to 2 ms.
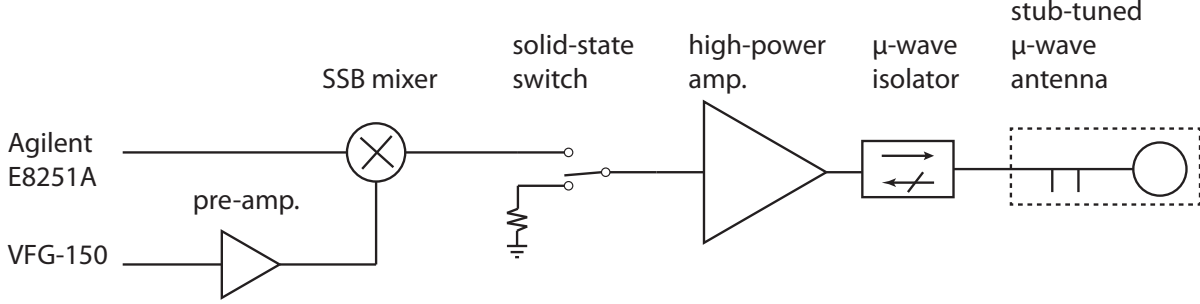
Figure 2.9: Circuit diagram for the new Rb microwave setup. We mix the stable microwave source (Agilent E8251A) with a pre-amplified (Mini-circuits ZFL-1000LN+) rf source from a DDS (Toptica VFG-150) using a single-sideband mixer (Marki Microwave SSB-0618LXW-1) that suppresses the higher frequency sideband power by 23 dB. The pulse length of this source is controlled by an absorptive solid state switch (Narda SP123DHTS) which in turn feeds a high-power (41 dBm) microwave amplifer (AML L0608-41-T479). Lastly, the microwaves travel through an isolator (Narda 4914) and to our double stub-tuned microwave antenna that was built in-house.

2.5   Calibrating the Rb atom number

Measurement of the condensate transition temperature provides a means to estimate the accuracy of other measured quantities in the system (e.g. atom number, temperature). For an ideal Bose gas in a harmonic potential, the transition temperature in the thermodynamic limit, (T_c), is given by

$$k_b\, T_c = \hbar\, \overline{\omega}\, (N/\zeta(3))^{(1/3)} \tag{2.5.1}$$

where k_b is Boltzmann's constant, $\overline{\omega}$ the geometric mean trap frequency, and $\zeta(3) \approx 1.20206$ the Riemann zeta function. The ideal Bose gas condensation temperature in a harmonic potential is related to the condensate fraction by

$$\frac{N_0}{N} = 1 - \left(\frac{T}{T_c}\right)^3, \tag{2.5.2}$$

where N_0 is the number of atoms in the condensate and T the temperature of the cloud. The strong dependence of condensate fraction on $\mathrm{T/T_c}$ yields a sharp signature of the transition, which is useful for calibration purposes.

This ideal Bose gas treatment ignores the importance of atom-atom interactions in ^{87}Rb (as well as finite number effects [29]). Although the Rb-Rb background scattering length is small ($a_{bg} \approx$

$100a_0$), the sharpness of the condensation transition is "smoothed" by the repulsive interactions between the condensed and thermal atoms. This effect was modeled in Ref. [112] where the condensate atoms were treated in the Thomas-Fermi limit and the potential for the thermal atoms was a sum between the harmonic potential and mean-field repulsion of the condensate atoms. The authors derived an implicit expression for the condensate fraction in terms of T/T_c, which, to the first non-trivial order in the interaction parameter η, is given by [112]

$$\frac{N_0}{N} = 1 - \left(\frac{T}{T_c}\right)^3 - \eta\frac{\zeta(2)}{\zeta(3)}\left(\frac{T}{T_c}\right)^2\left(\frac{N_0}{N}\right)^{2/5} \tag{2.5.3}$$

with η defined as

$$\eta = \frac{1}{2}\zeta(3)^{1/3}\left(N^{1/6}\frac{a}{a_{HO}}\right)^{2/5}, \tag{2.5.4}$$

where a is the scattering length and $a_{HO} = \sqrt{\hbar/m\omega}$ is the harmonic oscillator length for an atom of mass m in a harmonic trap of frequency ω.

To use Eqn. (2.5.3) as a test of how well the atom number is being counted, we first prepare a series of Rubidium clouds with varying degrees of condensation. The clouds are imaged using standard absorption imaging and the images of partially condensed clouds are processed into an optical depth (OD) image and then fit to a sum of a Thomas-Fermi parabola and a Bose distribution with the fugacity forced to one. The OD image fit returns peak OD's and cloud sizes, from which the atom number and temperature can be calculated from the following equations:

$$N_0 = \frac{2\pi}{5\,\sigma_0}(1+4\delta^2)OD_{pk,BEC}\,\sigma_{y,BEC}\,\sigma_{x,BEC}\left(\frac{pix}{M}\right)^2 \tag{2.5.5}$$

$$N_{th} = \frac{2\pi}{\sigma_0}(1+4\delta^2)OD_{pk,th}\,\sigma_{y,th}\,\sigma_{x,th}\left(\frac{pix}{M}\right)^2 \tag{2.5.6}$$

$$T_i = m_{Rb}\,\omega_i^2\frac{\sigma_{i,th}^2}{1+\omega_i^2\,t^2}\left(\frac{pix}{M}\right)^2 \tag{2.5.7}$$

where the photon scattering cross-section $\sigma_0 = \frac{3\lambda_{Rb}^2}{2\pi}$ for photons with wavelengths resonant with the Rb transition, λ_{Rb}, δ is the probe light detuning from resonance, $\sigma_{i,BEC}$ the BEC size in the i-th direction, m_{Rb} is the Rubidium atom mass, t the time of flight for the cloud, ω_i the harmonic trap frequency in the i-direction, and $\frac{pix}{M}$ is the ratio of the camera pixel size[14] (pix) to the imaging

[14] The pixel size for our Princeton Instrument Pixis camera is 13 μm.
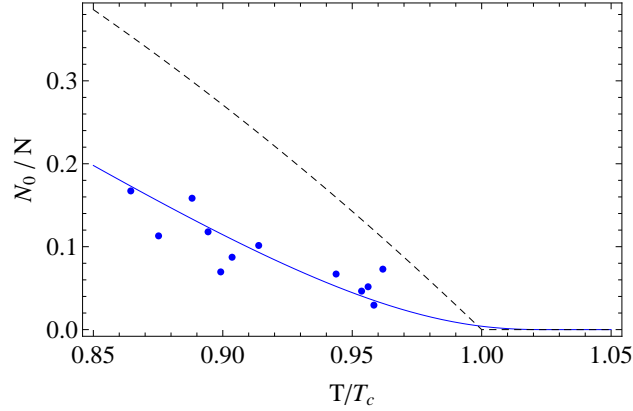
Figure 2.10: Measured condensate fraction after corrections for the various effects listed in the text. Fitting to Eqn. (2.5.3) with a scaling parameter for the horizontal axis returns the solid curve for which predicts the transition temperature to be T $= 1.025(6)(20)$ T$_c$ where T$_c$ is defined in Eqn. (2.5.1) and the first and second errors are the statistical and systematic errors, respectively. The dashed line is a plot of the condensate fraction for a non-interacting system (Eqn. 2.5.2).

system magnification, M. From the calculated number and temperature, T_c can be calculated from Eqn. (2.5.1) and then $\frac{T}{T_c}$ can be calculated. As can be seen from Eqns. (2.5.5−2.5.7,2.5.1), the calculated quantities depend strongly on the magnification, as well as the harmonic trap frequency in the case of T_c.

Shown in Fig. 2.10 is a single parameter fit of Eqn. (2.5.3) (solid blue curve) to the measured condensate fraction (blue points) compared to the ideal Bose gas prediction (dashed black curve). The fit of Eqn. (2.5.3) assumed a rescaled condensation temperature $T_c' = b\,T_c$, where T_c is the measured condensation temperature assuming the experimental calibrations and b is the sole fit parameter to account for a miscalibration of the atom number. The BEC transition occurs at $T/T_c' = 1$ and therefore the measured transition point is $\frac{T}{T_c} = b$ in terms of experimentally calibrated quantities. The fit returns $b = 1.025(6)(20)$, after correcting the data for the non-negligible frequency width of the probe laser [15] . The first error is purely statistical and the second a combination of trap frequency calibration error, imaging magnification, and probe laser frequency width error. This value of b implies that the number is being under-counted by $7(2)(5)\%$, in agreement with Section 2.4. The Rb numbers presented in this thesis are left uncorrected for

---

[15] Our Rb probe lineshape are generally 6.6 MHz wide, compared to the natural linewidth of 6.0666*(18) [143]. This amounts to a 10% correction on the Rb number [15].
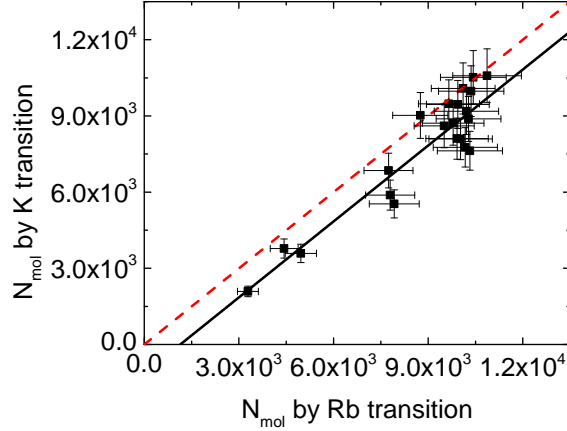
Figure 2.11: Plot of the molecule number measured using the bound K and bound Rb transitions in the same experiment run. The data were fit to a line (solid line) with a horizontal offset which gave a slope of 1.00(5) and a horizontal offset of $1.3(7) \times 10^3$. If we fit the data without an offset, the fit returns a slope of 0.83(3). For comparison, the dashed line is a line with slope of 1 and no offset.

the 7% systematic error.

The dominant sources of atom number measurement uncertainty can be separated into two categories: uncertainties in the properties of the apparatus and uncertainties intrinsic to the imaging process. From Eqns. (2.5.5−2.5.7, 2.5.1), the trap frequency and the ratio pix/M are the most critical parameters from the apparatus. The linewidth of the probe laser also can reduce the measured OD if it is a significant fraction of the natural linewidth of the transition (see discussion in Ref. [15]). Additional mechanisms include radiation trapping of probe light within the cloud and Doppler shifting of atoms' transition due to probe photon recoil [135], which are a small correction (1% OD correction) for typical conditions of this experiment.

2.5.1   Calibrating K atom number

Calibration of the K atom number is more complicated, as the K gas does not have a sharp phase transition. However, when we generate KRb molecules, as in Chapter 3, we know that a single K atom has bonded with a single Rb atom. The K atom number can be calibrated by imaging the bound K and bound Rb in the same experiment run. This required a new Rb microwave setup

as we have to quickly remove unbound Rb with a series of ARPs and kill pulses and then ARP the once-bound Rb into the imaging state after the molecules are dissociated shortly thereafter. Shown in Fig. 2.11 are the results of this measurement performed by generating a variable number of KRb molecules using methods discussed in Chapter 3. Fitting the data to a line with horizontal offset returns a slope of $1.00(5)$ and offset of $1.3(7) \times 10^3$. The offset was due to an imperfect kill pulse that left unbound Rb atoms in the $|2, 2\rangle$ state, which were imaged with the bound Rb[16] . Therefore our K and Rb number calibration agree to within 5 %.

---

[16] The imperfect kill pulse was confirmed by running the same magnetic field sequence with Rb present. After the kill pulse, atoms remaining in the $|2, 2\rangle$ state were observed.

Chapter 3

Feshbach molecules in the perturbative and saturated limits

Using ultracold samples of atoms, atomic physics has answered fundamental questions in physics, including some that cross over into particle physics and condensed matter. This was made possible by the years of work put into learning how to create ultracold atomic sample, as well as the more recent ability to control the sign and strength of atom-atom interactions. Tuning the atom-atom interaction has led to new understanding of the BCS-BEC crossover, observation of a fermionic superfluid, new understandings of few-body collisions, and many others.

This control of the atomic interaction strength is made possible by a Feshbach resonance, which results from coupling colliding atoms to one or more bound states in other inter-atomic potentials. In Fig. 3.1, a simplified picture of the potentials involved in a Feshbach resonance is shown. Only a single bound state is considered as represented by the solid orange line within the closed channel in Fig. 3.1. Initially the atoms are colliding at a low energy above the dissociation threshold of the entrance channel (denoted by the dashed blue line). If the closed channel has the correct quantum numbers, then the bound state will couple to the entrance channel and thus 'dress' the entrance channel. The energy of the bound state is nominally separated by an amount E_{CC} relative to the threshold of the entrance channel. When the experimentalist is able to vary E_{CC}, then as E_{CC} passes through zero the presence of a new bound state in the dressed state of the atoms causes a divergence in the dominant low-energy interaction-strength parameter, the s-wave scattering length.

One method of manipulating the relative energies of the entrance and closed channel is to use
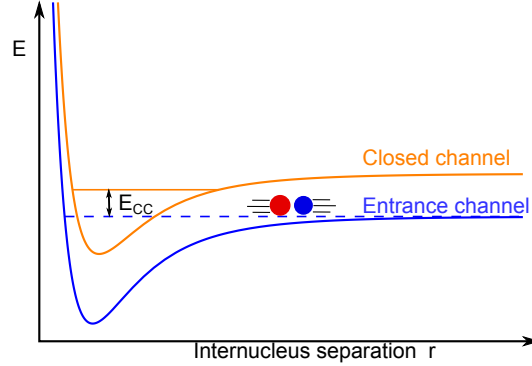
Figure 3.1: Two-channel model of a Feshbach resonance.

a homogeneous magnetic field and take advantage of the differential Zeeman shifts when the closed channel has a magnetic moment that differs from that of the open channel. The s-wave scattering length near a Feshbach resonance has a simple relation to the magnetic-field given by [109]

$$a = a_{bg} \left(1 - \frac{\Delta}{B - B_0} \right), \tag{3.0.1}$$

where a_{bg} is the non-resonant scattering length associated with the entrance channel, Δ is the zero-crossing resonance width, and B_0 is the location of the Feshbach resonance. Fig. 3.2 is a plot of (3.0.1) for the case of a_{bg}, $\Delta < 0$. By varying the magnetic field in the vicinity of a Feshbach resonance, the interaction strength can be varied over a large range.

The atoms can also be transferred into the bound state creating an extremely weakly bound molecule called a Feshbach molecule. In this chapter, Feshbach molecules created via a magnetically tunable Feshbach resonances will be discussed. In this context, the entrance and closed channels have different magnetic moments allowing E_{CC} to be tuned by applying a homogeneous magnetic field of varying strengths. Feshbach molecules have been generated in numerous homonuclear and heteronuclear systems [1] . Bosonic Feshbach molecules composed of two fermions [134] have been made to Bose condense [61]. Coherent oscillations between atoms and molecules have been observed in a homonuclear [46, 145] and a heteronuclear system [117]. Feshbach molecules have also proven

---

[1] To date Feshbach molecules have been observed in ^{6}Li [144, 82], ^{23}Na [169], ^{39}K [37], ^{40}K [134], ^{52}Cr [9], ^{85}Rb [75], ^{87}Rb [47], ^{133}Cs [74], ^{40}K-^{87}Rb [119], ^{41}K-^{87}Rb [159], ^{85}Rb-^{87}Rb [123], ^{87}Rb-^{133}Cs [32], ^{6}Li-^{40}K [150, 142], ^{23}Na-^{40}K [168], and ^{23}Na-^{6}Li [73].
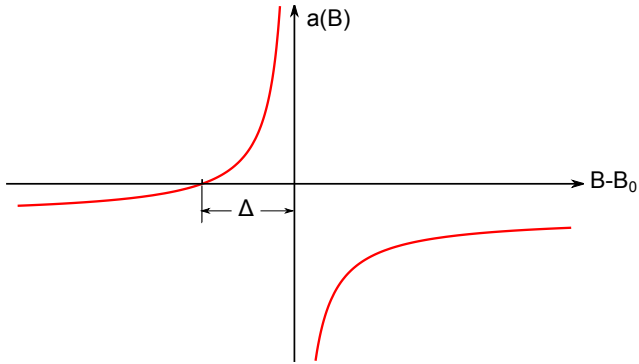
Figure 3.2: S-wave scattering-length near a Feshbach resonance.

to be an efficient starting point for the generation of ultracold polar molecules in the absolute molecular ground state [113].

However, the Feshbach molecule association is interesting in its own right. This chapter details research aimed at increasing the understanding of Feshbach molecule creation in the ^{40}K-^{87}Rb mixture system. The work described in this chapter is the subject of a manuscript in preparation for publication [27]. In Sec. 3.1, basic scattering physics will be discussed to orient the reader. This will be followed by a more detailed description of Feshbach resonances in section 3.2 and magnetoassociation of Feshbach molecules in Sec. 3.3, where molecules are generated by sweeping the magnetic field across the Feshbach resonance to generate molecules. Next I will discuss the research performed to understand molecule formation in the perturbative (fast magnetic-field sweep) limit and lastly the saturated (slow magnetic-field sweep) limit. Our approach to understanding the magnetic-field sweep rate dependence differs with previous studies, which characterized the sweep rate dependence with a e^{-1} inverse sweep rate [75]. This previous approach, in effect, mixes information from the two limits. Instead we characterize the molecule creation in terms of the two limits, which have different dependences on the gas parameters. In Subsection 3.4, we show that the number of molecules made in the perturbative limit is governed only by the Feshbach resonance parameters and the spatial overlap of the atom clouds. In contrast, the number of molecules associated in the saturated limit depends upon the phase-space density, as will be discussed in Section

3.5. To understand this limit, we use a phenomenological model which has successfully described homonuclear[75] and heteronuclear systems [174, 142]. While this model has been previously applied to our system, ^{40}K – ^{87}Rb, for rf association [174], we fit the model to molecule data taken by magneto-association. We examine various experimental concerns, including relative offsets between the atom clouds in position and center-of-mass velocity. Finally, we theoretically explore the limitations that prevent the creation of a quantum degenerate gas of fermionic Feshbach molecules in the absence of a BEC.

3.1   Basic scattering theory

Two-body scattering is a standard problem addressed in many quantum mechanics text books [20, 137]. This problem is generally expressed in the center-of-mass frame of the two colliding particles, 1 and 2, with a two-body reduced mass $\mu_{2b} = m_1 m_2/(m_1 + m_2)$, relative separation vector $\vec{r}$, and a relative momentum $\hbar \vec{k}$. As the two particles approach each other from far away, they begin to interact through an inter-particle potential $V(\vec{r})$. In the case of the work discussed in this thesis, the inter-atomic potential is isotropic and thus only depends on the magnitude of $\vec{r}$. Because of this symmetry, the Hamiltonian commutes with the angular momentum operators $\vec{L}^2$ and $\vec{L}_z$ and thus the wavefunction is separable into radial and angular parts. The scattering problem has an additional azimuthal symmetry, which yields spherical harmonics, $Y_{l,m}(\theta, \phi)$, as the solution to the angular part. The rest of the wavefunction is an expansion in partial waves of order ℓ, which is a product of a radial wavefunction $R_\ell(k, r)$ and Legendre polynomial $P_\ell(\cos(\theta))$. The partial wave orders take on values $\ell = 0, 1, 2, \ldots$ which are termed s-, p-, d-wave,... contributions. The radial part of the wavefunction is found by solving the Schroedinger equation of the form

$$\left[-\frac{\hbar^2}{2\mu} \frac{d^2}{dr^2} + \frac{\hbar^2}{2\mu_{12}} \frac{\ell(\ell+1)}{r^2} + V(r) - \frac{\hbar^2 k^2}{2\mu_{12}} \right] u_\ell(k, r) = 0 \qquad (3.1.1)$$

after making the substitution $u_\ell(k, r) = r\, R_\ell(k, r)$[20].

The solution to Schroedinger equation has the following asymptotic form

$$R_\ell(k,r) \xrightarrow[r\to\infty]{} \frac{A_\ell}{k\,r} \sin\left(kr - \ell\pi/2 + \delta_\ell(k)\right)\, e^{\imath\delta_\ell(k)} \tag{3.1.2}$$

where all the details of the two-particle interaction are carried in scattering phase shift, $\delta_\ell(k)$. At ultracold temperatures, scattering events are generally cold enough to only involve s-wave scattering. The details of the scattering can then be described solely by the s-wave scattering phase shift. The s-wave scattering phase shift is related to the s-wave scattering length, a, and effective range, r_{eff}, by the following [13]:

$$k\,\cot(\delta_0(k)) = -1/a + \frac{1}{2}r_{\text{eff}}\,k^2. \tag{3.1.3}$$

However, at ultracold temperatures the effective range term can often be neglected [24] and then the sign and magnitude of the scattering length fully parameterizes the interaction between the two particles. The strength of the interaction between the particles increases with the magnitude of the scattering length and the interaction is attractive for $a < 0$ and repulsive for $a > 0$.

For neutral alkali atoms scattering in their electronic ground states, the leading term in the long-range part of the interatomic potential is a van der Waals term given by [89]

$$V(r) \underset{r\to\infty}{=} -\frac{C_6}{r^6} \tag{3.1.4}$$

where the quantity C_6 is known as the van der Waals coefficient and can be calculated from first principles [36]. This coefficient also defines a length scale for Eqn. (3.1.4) by equating an energy of the form $-\dfrac{\hbar^2}{2\mu_{2b}r^2}$ to Eqn. (3.1.4) and solving for r. The length scale is then given by [89]

$$r_{vdW} = \frac{1}{2}\left(\frac{2\,\mu_{2b}\,C_6}{\hbar^2}\right)^{(1/4)} \tag{3.1.5}$$

after dividing the result of the previous sentence by two for definitional purposes. This quantity, the van der Waals length, is not the only way to define a length scale for the van der Waals potential. An alternative length scale is the mean scattering length given by [63]

$$\bar{a} = 4\,\pi/\Gamma(1/4)^2\,r_{vdW} \approx 0.956\,r_{vdW} \tag{3.1.6}$$
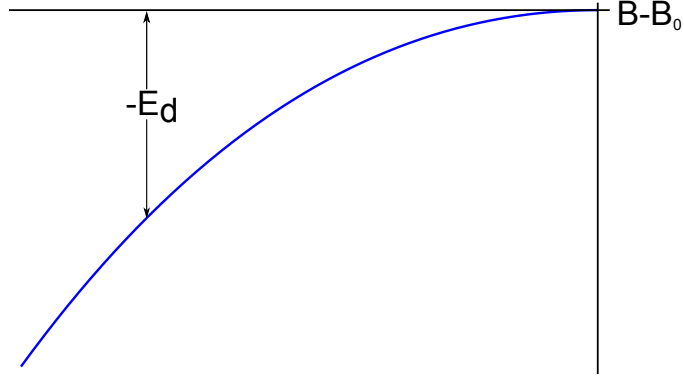
Figure 3.3: Binding energy, E_d, of a Feshbach molecule in the vicinity of the Feshbach resonance. The zero energy axis represents the energy of the colliding atoms in the entrance channel

where $\Gamma(x)$ is the Gamma function. For s-wave collisions at ultracold temperatures, interatomic separations on order of the van der Waals length mark the transition between the short-range and long-range aspects of the atom pair wavefunction [83].

3.2   Feshbach molecules

The Feshbach molecule state exists on the positive scattering-length side of the Feshbach resonance ($B - B_0 < 0$ in Fig. 3.2) and corresponds to a weakly bound molecule with a consequentially large spatial extent. Shown in Fig. 3.3 is a plot of the universal molecule binding energy in the vicinity of the Feshbach energy, where E_d is referenced to the open-channel threshold. These weakly bound molecules exhibit a universal binding energy given by

$$E_d = \hbar^2/(2\mu_{2b}\,a^2) \tag{3.2.1}$$

close to the Feshbach resonance, where by "close", we mean that the scattering-length that satisfies $E_d \ll \hbar^2/(2\mu_{2b}\,r_{vdW}^2)$ (or $a \gg r_{vdW}$).

As Köhler *et al.* explain in Ref. [89], the universality of the molecules close to the Feshbach resonance is a consequence of their large spatial extent. In the vicinity of a Feshbach resonance the molecule wave function has the form $\phi_d(r) = \dfrac{1}{\sqrt{2\pi\,a}}\dfrac{e^{-r/a}}{r}$, which has a mean inter-atomic separation of $\langle r \rangle = \frac{a}{2}$. Thus, for large scattering lengths ($a \gg r_{vdW}$) much of the wavefunction exists at large inter-atomic separations well outside of the inter-atomic potential, creating what is known as

a halo dimer [89]. For this asymptotic limit, inter-atomic interaction makes a negligible energetic contribution and the Schroedinger equation reduces to $E_d \, \phi_d \sim -\dfrac{\hbar^2}{2\mu_{2b}} \nabla^2 \phi_d$. The molecule wavefunction is then insensitive to the details of the inter-atomic interaction and the molecule exhibits universal behavior determined solely by the scattering length.

The range in magnetic field over which the molecule exhibits universal behavior depends upon the details of the Feshbach resonance. A convenient way to categorize resonances into two limiting cases is to use the resonance strength parameter given by [24]

$$s_{\mathrm{res}} = \frac{a_{bg}}{\bar{a}} \frac{\Delta \, \delta \mu}{\bar{E}} \qquad (3.2.2)$$

where $\bar{E} = \hbar^2 / (2\mu_{2b} \, \bar{a}^2)$ is the energy scale associated with $\bar{a}$ and $\delta \mu$ is the difference between the entrance- and closed-channel's magnetic moments [24]. Resonances for which $s_{res} \gg 1$ are called *open-channel dominated*. Open-channel dominated resonances are generally broad ($\Delta > 1\,G$) and the spin character of the wavefunction for threshold collisions, as well as the molecule wavefunction near the resonance, are largely that of the open channel. These resonances exhibit universal behavior over a large fraction of their resonance width, Δ. *Closed-channel dominated* resonances correspond to the limit $s_{res} \ll 1$. Generally closed-channel dominated resonances are narrow[2] ($\Delta < 1\,G$). Additionally, closed-channel resonances exhibit universal behavior over a small fraction of their resonance width, Δ.

The molecule binding energy only follows (3.2.1) for small detunings from the Feshbach resonance. Further away from the universal regime, the molecule binding energy must be corrected for the non-zero range of the inter-atomic potential. The lowest-order correction is given by [24]

$$E_d = \frac{\hbar^2}{2\mu_{2b} \, (a - \bar{a} + R^*)^2}, \qquad (3.2.3)$$

where $\bar{a}$ term is a correction for finite-range of the van der Waals interaction and $R^* = \bar{a}/s_{res}$ is an additional term introduced in [128].

Ref.	B_0 (G)	Δ (G)	a_{bg} (a_0)
Olsen et al.(2009) [117]	546.71(1)	-3.34(5)	-185(7)*
Klempt et al. (2008) [86]	546.618(5)(6)	-3.04(2)	-187*
Zirbel et al. (2008) [174]	546.76(5)	-3.6(1)	-185(7)*
Simoni et al.(2008) [140]	546.75*	-3.1*	-189*
Deuretzbacher et al. (2008) [38]	546.669(24)(2)	-2.92	-185(4)*
Klempt et al. (2007) [87]	546.71	-3.07*	-185(7)*^{a}
Zaccanti et al. (2006) [171]	546.65(2)	-3.3(2)	-185(4)*
Ospelkaus et al. (2006) [121]	546.8(1) G	-2.9*	-189*
Ferlaino et al.(2006) [55]	546.7	-2.9*	-185(7)*

^{a} Ref. does not quote a value, so one is assumed from its references.

Table 3.1: Comparison of the ^{40}K – ^{87}Rb Feshbach resonance parameters for the $|9/2, -9/2\rangle + |1,1\rangle$ resonance at $\approx$546.7 G as reported in various publications. In this table, B_0 is the measured resonance center, Δ is the zero-crossing width, and a_{bg} the background scattering length. All quantities with an asterisk (*) are theoretical predictions.

3.2.1 The 546.7 G Feshbach resonance

One of the more challenging aspects of working with a Feshbach resonance is having an accurate understanding of how the scattering length depends on magnetic field, which relies on having an accurate and precise measurement of the Feshbach resonance parameters. The s-wave Feshbach resonance employed for the work detailed in this chapter has been the subject of numerous theoretical [55, 87, 140, 79] and experimental investigations [55, 140, 117, 86, 38, 87, 171, 79]. The more recent results for the Feshbach resonance parameters are summarized in Table 3.1. This particular Feshbach resonance is between $|f, m_f\rangle = |1,1\rangle$ hyperfine state of ^{87}Rb and the $|9/2, -9/2\rangle$ state of ^{40}K, with the dominant closed-channel contribution being from the second bound state below the scattering threshold in the $|1,0\rangle$ and $|7/2, -7/2\rangle$ interatomic potential [174, 84]. Here f

---

^{2} One exception to this rule-of-thumb is the 737 G resonance in ^{7}Li: $s_{res} = 0.80$ even though it has a width of $\Delta = -192G$.
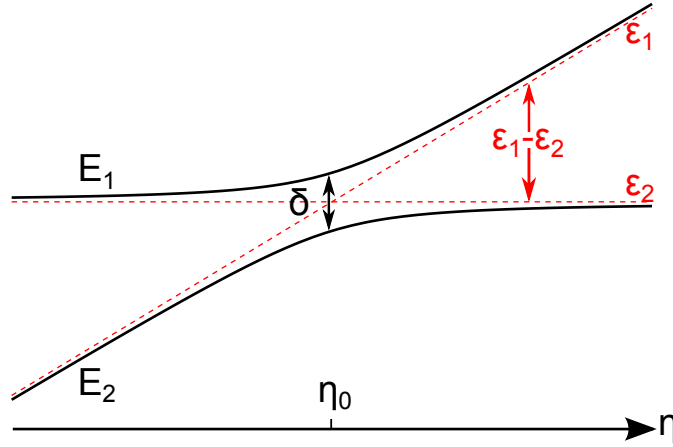
Figure 3.4: Energy diagram for a Landau-Zener avoided crossing. The two bare states ϕ_1 and ϕ_2 (bare-state energies ϵ_1 and ϵ_2 are red dashed lines) are coupled together at a system parameter value $\eta = \eta_0$. Because of the coupling, ϕ_1 and ϕ_2 are no longer the eigenstates; the eigenenergies of the coupled system are given by E_1 and E_2 (thick black curves).

is the total atomic angular momentum and m_f is the projection along the magnetic field.

Many of the early studies of this resonance relied on three-body recombination to locate the resonance [79, 55, 171, 87] and rethermalization between Rb and K to measure the zero-crossing width, Δ [171]. Most of the more recent characterizations of this resonance involve spectroscopic measurements of the molecule binding energy to characterize the Feshbach resonance. Many measurements of the Fano-Feshbach resonance have used rf-association spectroscopy to map out the molecule binding energy [174, 86, 38]. In Ref. [117] (of which this author is a co-author), Olsen et al. observed coherent atom-molecule quantum beats whose frequency was determined by the molecule binding energy. Using a Ramsey-type experiment, the authors were able to map out the molecule binding energy in the vicinity of the Feshbach resonance. Fitting the measured binding energies to the universal molecule binding energy formula returned values for the resonance position and width. The Feshbach parameters from this last measurement (Olsen *et al.* [117]) are used in calculations for this chapter.

3.3 Magneto-association of Feshbach molecules

There are several different ways to use a Feshbach resonance to bind atoms together. In Feshbach-assisted radio-frequency association, the atoms begin in a non-resonant state with the magnetic field on the $a > 0$ side of resonance. Applying a pulse of rf of the frequency corresponding to atom-atom transition plus the molecule binding energy causes some of the atoms to be bound into molecules [86, 174, 38, 9]. In a similar fashion, atoms can be bound by sinusoidally modulating the magnetic field at the frequency corresponding to the binding energy of the time-averaged magnetic field [62, 147, 123, 68, 94]. A third method, called magneto-association, involves ramping the magnetic field linearly in time from the negative scattering-length side of the Feshbach resonance to the positive scattering-length side. This widely used method has been used to create bosonic Feshbach molecules from fermionic atoms in ^{40}K[134], ^{6}Li [144], and more recently in ^{6}Li-^{40}K[150, 142]. Bosonic atoms have also been associated to create bosonic Feshbach molecules in ^{23}Na[169], ^{85}Rb[75], ^{87}Rb[47], ^{85}Rb-^{87}Rb[123], ^{133}Cs[74], and very recently in ^{87}Rb-^{133}Cs[32]. Fermionic Feshbach molecules have previously been generated by magneto-association in ^{40}K-^{87}Rb in Refs. [119, 174, 117] and recently in ^{23}Na-^{40}K [168] and ^{23}Na-^{6}Li [73].

The magneto-association process can be qualitatively understood in terms of a Landau-Zener model[3] , whose schematic energy level diagram is shown in Fig. 3.4. The Landau-Zener model begins with two bare states ϕ_1 and ϕ_2 of energies ϵ_1 and ϵ_2, which approach each other energetically as a function of a system parameter η, which in the case of this chapter is the magnitude of the magnetic field. Due to the coupling between the two states, they form an avoided crossing at some parameter value $\eta = \eta_0$ [172]. This coupling results in a mixing of the two bare states such that they are no longer eigenstates of the system. The eigenvalues of the coupled system are the black curves shown in Fig. 3.4 labeled E_1 and E_2, which asymptotically approach ϵ_1 and ϵ_2 far from $\eta = \eta_0$. If the system is initialized infinitely far away from η_0, in one of the two bare states, and then η is swept linearly in time through, and infinitely far past, η_0, then the system can adiabatically be

---

[3] Many-body treatments of magneto-association predict an approach to saturation that is slower than for a Landau-Zener model[45]
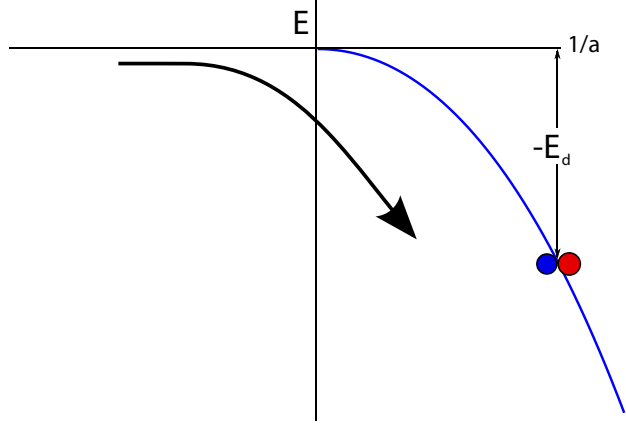
Figure 3.5: Magneto-association of atom with zero relative kinetic energy. The magnetic field begins with $a < 0$ where no weakly bound state exists. As the magnetic field is ramped through the Feshbach resonance at $B = B_0$, atom pairs can be bound into a Feshbach molecule.

transferred from one bare state to another. The probability of the system adiabatically following the eigenstate is given by the following:

$$P_{LZ} = 1 - e^{-2\pi\delta_{LZ}}. \tag{3.3.1}$$

The Landau-Zener parameter is given by $\delta_{LZ} = \delta^2 / (4\hbar|\frac{d}{dt}(\epsilon_1 - \epsilon_2)|)$ for a relative energy separation of the two eigenenergies of δ at $\eta = \eta_0$ [172]. Thus, the probability of starting in ϕ_1 and adiabatically transferring into ϕ_2 is higher for slower ramps (i.e. smaller $|\frac{d}{dt}(\epsilon_1 - \epsilon_2)|$).

For the case of magneto-association, the energy diagram resembles Fig. 3.5. The system energy is controlled by the magnetic field; the two bare states correspond to a scattering state in the entrance channel and a bound state in the closed channel, and the energy separation of the two states is controlled by the magnetic field. To associate atoms, the magnetic field begins on the negative scattering-length (unbound) side of resonance (the left side of Fig.3.5) and sweeps linearly in time to the positive-scattering-length (bound) side of the Feshbach resonance.

Shown in Fig. 3.6 is an example of magneto-association with ultracold ^{40}K-^{87}Rb, where the molecule creation efficiency ($f = N_{mol}/N_<$, where $N_<$ is the number of atoms of the species with the lower atom number) as a function of the inverse magnetic-field sweep rate ($|\dot{B}|^{-1}$). We prepared the system with 3.4×10^5 ^{87}Rb atoms in the $|1, 1\rangle$ state and 2.6×10^5 ^{40}K in the $|9/2, -9/2\rangle$ state at

a quantum degeneracy of $T/T_c = 1.5$ in an optical trap with a radial trap frequency of 630 Hz (450 Hz) and axial trap frequency of 8.2 Hz (5.9 Hz) for K (Rb). The magnetic field began 5 G above the heteronuclear Feshbach resonance between Rb $|1,1\rangle$ and K $|9/2,-9/2\rangle$ at approximately 546.7 G. Next, we ramped the magnetic field linearly down through resonance to 5 G below resonance on the bound side where the molecules have a binding energy of roughly $h \cdot 12$ MHz (cf. Fig. 5 of [174]). To reduce the density of the atom clouds before molecule association, we released the atoms from the optical trap by abruptly shutting off the trap. While the atom clouds expanded, we swept the magnetic field through the Feshbach resonance such that the magnetic field crossed the Feshbach resonance 0.4 ms after trap release. We imaged the molecules as in Refs. [117, 174] where unbound K atoms were transferred to the $|9/2,-7/2\rangle$ state using an rf adiabatic rapid passage (ARP) with a 1.6 MHz frequency span. Once the unbound K atoms were transferred to $|9/2,-7/2\rangle$, the magnetic field was then ramped to 0.7 G below resonance and the molecules were imaged using the K probe light[4] ; the first probe photon breaks the molecule and subsequent photons excite the once-bound K atom on the $|9/2,-9/2\rangle \rightarrow |11/2',-11/2\rangle$ cycling transition. The ARP used to clear out the unbound K is only $\approx 99\%$ efficient, which leaves adds a background of ≈ 2000 to our molecule signal, which has been subtracted from Fig. 3.6. This background is measured after the same magnetic-field sweep used for magneto-association, but without Rb present in the trap.

In order to extract information about the molecule formation, the data in Fig. 3.6 were fit to an exponential (similar to Ref. [75]) given by

$$f = f_0 \left[1 - \exp \left(-\frac{\Gamma}{f_0} |\dot{B}|^{-1} \right) \right] \tag{3.3.2}$$

where the quantity Γ is the initial slope of Fig. 3.6 and f_0 is the saturated molecule fraction in the limit of slow magnetic-field sweeps. This parameterization of the fit allows for information to be extracted from two regimes. In contrast, in Ref. [75] the magnetic-field sweep dependence was characterized in terms of a 1/e inverse sweep rate whose fitted value did not agree with theory, even after thermally averaging the Landau-Zener coefficient over open-channel continuum states

---

[4] K in the $|9/2,-7/2\rangle$ at this field is roughly 13 natural linewidths detuned from the probe transition and it does not significantly perturb the molecule imaging.
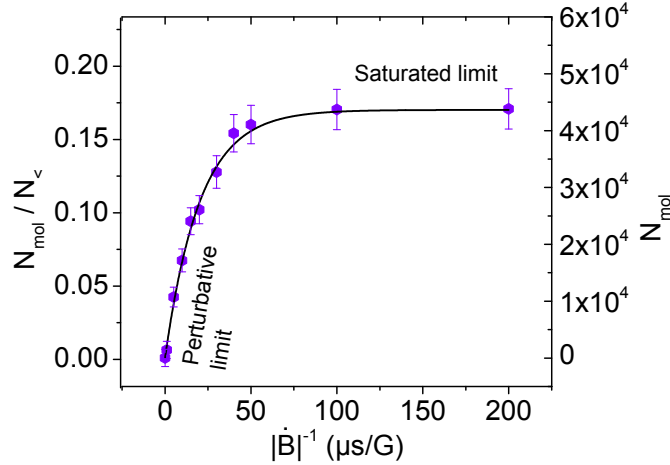
Figure 3.6: Molecule creation measured after sweeping the magnetic field through the Fano-Feshbach resonance. The molecules were produced from 3.4×10^5 Rb atoms and 2.6×10^5 K atoms at $T/T_c = 1.5$ and $T/T_F = 0.6$. To reduce the density, the atom clouds were released from the trap 0.4 ms before the magnetic field crossed the Fano-Feshbach resonance. The data were fit to Eqn. (3.3.2) returning $\Gamma = 8.5(3) \times 10^{-3} G/\mu s$ and $f_0 = 0.171(4)$, as defined in the text.

[90]. With this new parameterization, the saturated molecule creation efficiency, f_0, only contains information about the *saturated limit*. The molecule creation efficiency in the saturated limit, the limit of slow magnetic-field sweeps, is governed by the quantum degeneracy of the atom clouds [75, 164]. This will be the subject of Subsec. 3.5.1. As will be discussed in Sec. 3.4, Γ contains information on the *perturbative limit*. In this limit, which is the limit of fast magnetic-field sweeps, we will show that the molecule creation efficiency is determined by the Feshbach resonance parameters and the spatial density overlap of the two clouds.

3.4 Molecule creation in the perturbative limit

For the perturbative limit, or fast magnetic-field sweep rate limit, theoretical treatment of magneto-association is discussed in Refs. [25, 89], where the approach begins in the context of a Landau-Zener model [172]. For the case of two isolated atoms in a box of volume $\mathcal{V}$, the probability of a molecule being created after the magnetic-field sweep through the Feshbach resonance is $P_{2-body} = 1 - \exp(-2\pi\delta_{LZ})$. The two-body Landau-Zener coefficient for atoms interacting via a

Feshbach resonance is given by [89]

$$\delta_{LZ} = \frac{1}{\mathcal{V}} \frac{4\pi\hbar}{2\mu_{2b}} \left| \frac{a_{bg}\,\Delta}{\dot{B}} \right| \tag{3.4.1}$$

in the quantization volume $\mathcal{V}$ for reduced mass $\mu_{2b} = (1/m_1 + 1/m_2)^{-1}$, background scattering length a_{bg}, and at an inverse magnetic-field sweep rate $\dot{B}^{-1}$ [89]. In the limit of high ramp speed, the two-body association probability reduces to $\mathrm{P}_{\text{2-body}} \approx 2\pi\delta_{LZ}$.

A simple classical probability theory can be used to extend this two-body probability to an expected number of molecules formed in a many-particle system [25]. In this fast-sweep limit the probability of creating a molecule from a single atom-pair is small and one can think of the atom populations as large reservoirs of atoms from which a perturbative number of molecules are formed. These reservoirs of atoms enhance the probability of a given atom associating in that each N_1 atoms of one species has N_2 possible partners, where N_2 is the number of atoms of the other species. Since the Bose-Fermi mixture system is an incoherent mixture of bosons and fermions, the fraction of molecules generated in the perturbative limit is then the incoherent sum of all possible two-particle combinations of dissimilar atoms ($N_1\,N_2$) multiplied by P_{2-body} and divided by $\mathrm{N}_<$:

$$f = \frac{N_1 N_2}{N_<} P_{2-body} \approx \frac{N_1 N_2}{N_< \mathcal{V}} \frac{8\pi^2\hbar}{2\mu_{2b}} \left| \frac{a_{bg}\,\Delta}{\dot{B}} \right| \text{ for } f \ll f_0 \tag{3.4.2}$$

Using a local density approximation, we can extend this to the more realistic situation of an inhomogeneous density distribution. In this approximation, the clouds are divided into boxes of differential volume $d\mathcal{V}$. The number of atoms of species-i in a given volume is $n_i(\vec{r}_j)\,d\mathcal{V}$, where $n_i(\vec{r}_j)$ is the number density of particles of species i at the location $\vec{r}_j$. The expression for the molecule fraction in a fast magnetic-field sweep becomes

$$\begin{aligned} f &= \frac{8\pi^2\hbar}{2\mu_{2b}} \left| \frac{a_{bg}\,\Delta}{\dot{B}} \right| \frac{1}{N_<} \sum_j n_1(\vec{r}_j)\,d\mathcal{V}\, n_2(\vec{r}_j)\,d\mathcal{V} \frac{1}{d\mathcal{V}} \qquad \text{for } f \ll f_0 \\ &= \frac{8\pi^2\hbar}{2\mu_{2b}} \left| \frac{a_{bg}\,\Delta}{\dot{B}} \right| \frac{1}{N_<} \sum_j n_1(\vec{r}_j)\, n_2(\vec{r}_j)d\mathcal{V} \end{aligned} \tag{3.4.3}$$

,which becomes the following after taking the continuum limit of (3.4.3):

$$f = \frac{8\pi^2\hbar}{2\mu_{2b}} \left| \frac{a_{bg}\,\Delta}{\dot{B}} \right| \langle n_> \rangle \qquad\qquad \text{for } f \ll f_0 \qquad\qquad (3.4.4)$$

$$= \frac{\Gamma}{|\dot{B}|} \qquad\qquad\qquad (3.4.5)$$

where $\Gamma = \frac{8\pi^2\hbar}{2\mu_{2b}} |a_{bg}\,\Delta|\,\langle n_> \rangle$ and the average majority-species density is $\langle n_> \rangle = \int n_1\,n_2/N_<\,d^3r$.

Eqn. (3.4.4) can be further simplified by evaluating the integral assuming gaussian atom clouds. In general, the two atom clouds can have disparate sizes as well as a relative position offset. The density product integral is a product of three gaussian integrals

$$\int n_1\,n_2\,d^3x = n_{1,0}\,n_{2,0} \prod_{j=1}^{3} \left(\int e^{-(x_j - \delta_j)^2/(2\sigma_{1,j}^2)}\,e^{-x_j^2/(2\sigma_{2,j}^2)}\,dx_j \right) \qquad (3.4.6)$$

$$= N_1\,\langle n_2 \rangle_{\delta=0} \prod_{j=1}^{3} \left(\sqrt{\frac{2}{\sigma_{1,j}^2/\sigma_{2,j}^2 + 1}}\;e^{-\delta_j^2/[2(\sigma_{1,j}^2 + \sigma_{2,j}^2)]} \right), \qquad (3.4.7)$$

where $\sigma_{i,j}$ is the rms width of the species-i cloud in the j-th direction and δ_i is the relative cloud separation and $\langle n_2 \rangle_{\delta=0}$ denotes the density overlap integral in the case of perfect cloud overlap. The expression for Γ from Eqn. (3.4.5) then becomes

$$\Gamma = \frac{8\pi^2\hbar|\,a_{bg}\,\Delta|}{2\mu_{2b}}\,\langle n_> \rangle_{\delta=0} \prod_{j=1}^{3} \left(\sqrt{\frac{2}{\sigma_{1,j}^2/\sigma_{2,j}^2 + 1}}\;e^{-\delta_j^2/[2(\sigma_{1,j}^2 + \sigma_{2,j}^2)]} \right) \qquad (3.4.8)$$

where it is important to note that this expression is symmetric upon exchange of species-1 with species-2.

Figure 3.7 shows a comparison of our measurements with the theoretically predicted Γ as a function of $\langle n_> \rangle$. Ultracold clouds of K and Rb were prepared with a range of conditions ($1.3 \leq T/T_c \leq 1.7$, $0.6 \leq T/T_F \leq 0.7$) in the optical trap with $N_K \approx 2 \times 10^5$ and $N_{Rb} \approx 3 - 5 \times 10^5$. To vary the atomic density, the clouds were abruptly released from the optical trap and allowed to expand for 0.1 ms to 0.5 ms before the magnetic field crossed the Fano-Feshbach resonance. Assuming ballistic expansion, the density overlap integral is reduced from in-trap conditions by up to a factor of four. The experimental values for Γ were extracted from least-squares fits of molecule association data as in Fig. 3.6 using Eqn. (3.3.2). In Fig. 3.7 the vertical error bars show the
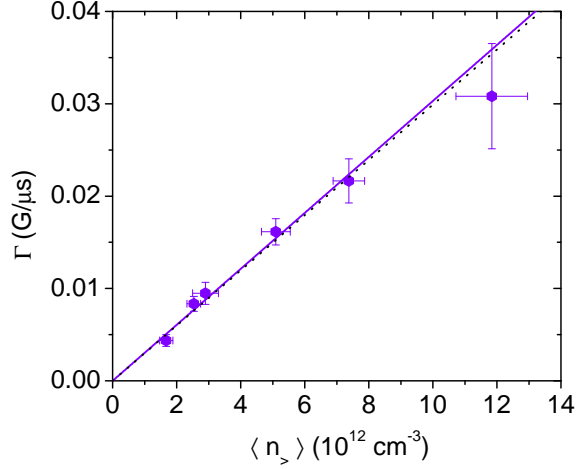
Figure 3.7: Initial molecule creation rate compared with theory from Eqn. (3.4.8). The initial molecule creation rate in the limit of fast magnetic-field sweeps is plotted against the average majority-species density, $\langle n_> \rangle$. For the Fano-Feshbach resonance parameters given in the text, the theoretically predicted slope of Γ vs. $\langle n_> \rangle$ is $2.99(12) \times 10^{-15}$ G/μs/cm^{-3} (dashed line). The solid line is a weighted least-squares fit to the data, which gives a slope of $3.06(13) \times 10^{-15}$ G/μs/cm^{-3}. The fit has a reduced chi-squared parameter of 0.7.

statistical error (one standard deviation) in Γ from the fit (e.g. from Fig. 3.6) and the horizontal error bars show the statistical uncertainty in the density.

Using the Fano-Feshbach resonance parameters from Ref. [117] ($a_{bg} = -185(7)\,a_0$ [54] and Δ = -3.34(5) G), the theoretical prediction for the slope of Fig. 3.7 is $2.99(12) \times 10^{-15}$ G/μs/cm^{-3}. The dashed line in Fig. 3.7 shows the theoretical prediction of the slope. A linear fit to the data in Fig. 3.7 (with an intercept of 0) returned 3060(200) for the slope, where the error includes statistical error and systematic error due to uncertainties in trap frequencies and the imaging system's magnification. The data agree well with the theory, which provides evidence that, in the perturbative limit, the number of Feshbach molecules created depends only on the Feshbach resonance parameters and the density overlap of the two atom clouds. Furthermore, this demonstrates that by using the parameterization of Eqn. (3.3.2), we can indeed separately examine the perturbative limit.

3.5 Molecule creation in the saturated limit

To understand the molecule formation process in the saturated limit, we employ a phenomenological model that successfully described the Feshbach molecule formation efficiency for magneto-association of ^{40}K-^{40}K [75], ^{85}Rb-^{85}Rb[75], ^{85}Rb-^{87}Rb[123], and ^{6}Li-^{40}K [142], as well as the rf-association efficiency of ^{40}K-^{87}Rb[174] molecules. This model will be the subject of the next subsection. Although this model does not include any time-dependent quantities, adiabatic formation of the molecules is assumed. Adiabatic formation requires slowly sweeping the magnetic field through the Feshbach resonance, which entails spending substantial time at large scattering lengths where the inelastic losses of atoms and molecules are large. These inelastic losses are not included in the model.

3.5.1 Semi-classical simulation of molecule formation

In order to simulate the fraction of Feshbach molecules formed in the saturated, or adiabatic, limit, the so-called "Semi-classical Phase-Space Sampling" (SPSS) model was used [75, 164]. This model was originally based on the argument that efficiency of molecule formation should be closely connected to the atoms' relative proximity in phase space[5] . In this model, only pairs of atoms that are sufficiently close together in phase space can transform into a molecule. The authors of Ref. [75] used the defining relation for the model

$$\mu_{2b} \, |\vec{v}_{rel}| \, |\vec{r}_{rel}| \, < \, \gamma \, \frac{h}{2}, \tag{3.5.1}$$

where μ_{2b} is the reduced mass of the atom pair, $\vec{v}_{rel}$ their relative velocity, $\vec{r}_{rel}$ their relative spatial separation, and h is Planck's constant. As part of the model, a "monogamy" clause is enforced: a single atom of type 1 is only allowed to bind to a single atom of type 2 and, once the atoms are bound, both are removed from the pool of available atoms. The parameter γ was determined by fitting the model to molecule association data for ^{40}K-^{40}K and ^{85}Rb-^{85}Rb returning $\gamma_K = 0.38(4)$

---

[5] Theoretical underpinning has since been provided for the homonuclear case in Ref. [164] and the heteronuclear case in Ref. [158], but the assumption of thermodynamic equilibrium is made in the theory, which is not the case for our molecules.

and $\gamma_{Rb} = 0.44(3)$, respectively. For this model, the governing parameter is the degeneracy of the system, i.e. T/T_F and T/T_c for Fermi and Bose systems, respectively. The agreement between the values for γ, as well as the good agreement with the model for homonuclear systems, suggests that this model could be applied to heteronuclear systems. This model was applied to heteronuclear molecule formation for the ^{85}Rb-^{87}Rb system [123], ^{40}K-^{87}Rb [174, 116], and more recently in ^{6}Li-^{40}K[142].

For this thesis, the model was implemented in a Matlab code and, after calibrating γ, was used to address the importance of relative atom cloud offsets and provide guidance for improving the molecules quantum degeneracy. This code was optimized to decrease the computation time through vectorizing loops, using vectorized conditional logic, preallocating memory for arrays, and using static sized arrays. This speed increase allowed for simulations using realistic atom numbers, instead of scaling up calculations for smaller atom numbers. Details of this simulation and its implementation are discussed in Appendix A.

3.5.2 Molecule creation efficiency

To look at the saturated molecule fraction, we generated molecules with a range of initial T/T_F values. Parametric heating was employed to vary the cloud temperature with the atom numbers fixed. The atoms were prepared with the magnetic field 5 G above the Feshbach resonance on the positive scattering-length side. The magnetic field is then swept linearly down through the resonance at an inverse ramp rate of 200 μs/G and as the field crosses the resonance, the atoms and molecules are abruptly released from the optical trap and allowed to expand from an optical trap with a 627 Hz (448 Hz) radial trap frequency and 8.2 Hz (5.9 Hz) axial trap frequency for K (Rb). The magnetic field continues sweeping down until it is 5 G below the resonance, at which point the unbound K atoms can be transferred to the $|9/2, -7/2\rangle$ state using a 1.6 MHz wide Adiabatic Rapid Passage (ARP, c.f. Subsection 2.3.2) [6] . After the ARP, the magnetic field is ramped up to 0.7 G below the Feshbach resonance where the molecules are imaged 1.7 ms in expansion using the

---

[6] The molecules are $\approx$12 MHz bound at this magnetic field and are not addressed by the ARP.
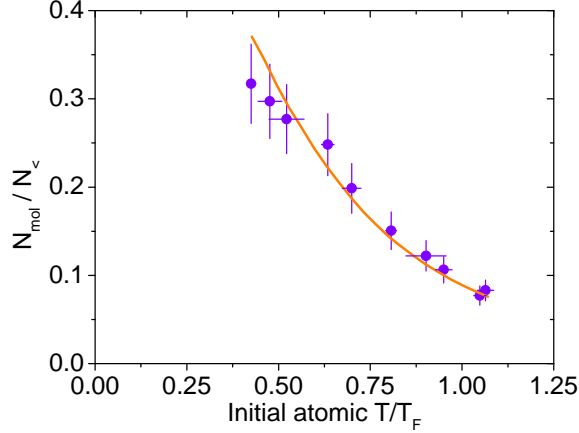
Figure 3.8: Molecule creation efficiency measured in trap as a function of the initial atomic T/T_F. The molecules were formed from 1.2×10^5 Rb atoms and 1.6×10^5 K atoms. The initial temperature was varied by parametrically heating the gas before sweeping the magnetic field to create molecules. The solid line is the results of a least-squares fit of the SPSS model to the five points with the largest initial atomic T/T_F returning $\gamma = 0.352(6)$.

K probe light on the $|9/2, -9/2\rangle \rightarrow |11/2', -11/2\rangle$ transition.

We fit the molecule creation efficiency data to the SPSS model using a full-scale simulation that uses the same atom numbers and trap frequencies as in the experiment. This eschews the finite-system size corrections [7] employed previously by the authors of Ref. [75]. The SPSS model is semi-classical in nature and neglects the fermionic statistics of the molecules [8] . Figure 3.8 shows the result of the fit (solid line) overlaid with our data, where the fit returned $\gamma = 0.352(6)$. This result is in agreement with the fermionic atom result of Ref. [75], $\gamma_F = 0.38(4)$, but not the bosonic atom result $\gamma_B = 0.44(3)$. We fit only the data with the atomic $T/T_F > 0.75$ where the effect of inelastic collisions between atoms and molecules are smaller because of the lower density of the atom gas. Overall, the model shows good agreement, with the exception of the systematic offset at low T/T_F. At low T/T_F the systematic offset is likely due to the effects of inelastic collisions with unpaired atoms.

---

[7] We find that this correction amounts to a $\sim$10% correction in γ, which was correctly accounted for by the authors of Ref. [75].

[8] Given the temperatures (initial K atom $T/T_F > 0.4$) and molecule numbers, this effect is unlikely to be important for our data.
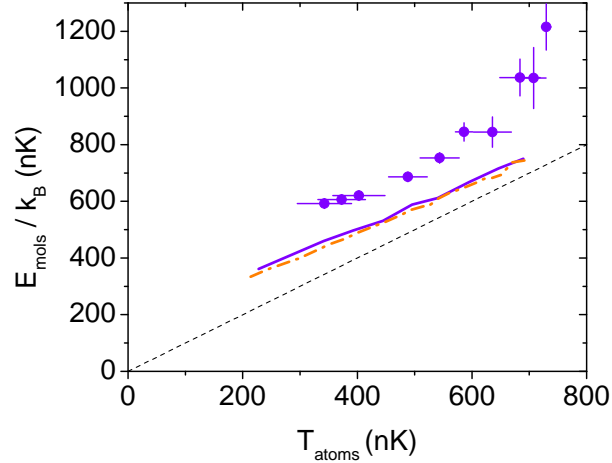
Figure 3.9: Measurement of the molecule temperature defined by their expansion energy as a function of the initial atomic temperature. The solid curve is the simulation results of the SPSS model and the dashed line is a line with a slope of one.

Another interesting question to ask of this model is how does temperature, or expansion energy, relate to the initial atomic temperature? This question is particularly important to experiments that use Feshbach molecules to generate absolute ground-state molecules because the ground-state molecules are often generated from Feshbach molecules [113]. We find that if we allow the SPSS model code to pair atoms purely randomly by not enforcing Eqn. (3.5.1), then the molecular temperature is equal to the initial atomic temperature. However, when Eqn. (3.5.1) is enforced, then the molecular temperature is higher than the atomic temperature, as shown in Fig. 3.9.

The data shown in Fig. 3.9 is from the same data set as Fig. 3.8. While the molecular distribution is not thermalized, we use $E_{mols} = k_B T_{mols}$ to express the expansion energy in temperature units. The theory curves qualitatively describes the expansion energy of the molecules, but the theory curve (solid curve) predicts a systematically lower expansion energy. In addition, we plot the simulation results where the trap frequencies of the Rb and K atoms are forced to be equal (dash-dotted curve). In this case only, the two-atom system can be separated into relative and center-of-mass coordinates. As can be seen, the the lack of separability is not a significant factor

in determining the molecule expansion energy. This prediction of lower expansion energy by the model may be due to interaction energy between the molecules and atoms, collisional heating of the molecules, or merely a failure of the SPSS model defined by Eqn. (3.5.1) to accurately describe the molecule momentum distribution. Further investigation is needed to sort out these possibilities.

3.5.3   Experimental concerns

This model of molecule formation serves another use for the experimentalist: determining the importance of various experimental problems and techniques. Given the dependence on relative occupation in phase-space, it is reasonable to assume that the molecule creation efficiency will be decreased by relative offsets in position or momentum of the atom clouds. Adding relative momentum and positions offsets into the simulation allows one to estimate the importance of these offsets. Additionally, the effect of ballistic expansion before molecule formation can be modeled.

3.5.3.1   Relative position and momentum offsets

The optical trap utilized for this experiment has a large aspect ratio with weak confinement in the axial direction (typical axial trap frequencies are 5-10 Hz). In the optical trap, Rb and K experience different trapping frequencies[9] . The atoms also have different magnetic moments[10] , which allows for magnetic-field gradients to cause relative position offsets between the atom clouds, or momentum offsets (i.e. slosh) if the magnetic-field gradient is changed too rapidly. To model the significance of the effect of axial slosh on the molecule creation efficiency, a momentum offset was added to the simulated Rb cloud, and none to the simulated K cloud, before the molecule formation was simulated. The slosh kinetic energy was parameterized as a fraction f of the cloud temperature such that $m_{Rb} v_{slosh}^2 = f k_B T$, where k_B is Boltzmann's constant and m_{Rb} is the Rb atom mass. Similarly, the significance of position offsets was modeled by offsetting the Rb cloud before the molecule formation.

---

[9] This is due to dissimilar masses, but similar ground-state electric dipole polarizabilities[36, 76]

[10] Rb in the $|1, 1\rangle$ hyperfine state has a magnetic moment of $\mu = -1/2\mu_B$ and K in the $|9/2, -9/2\rangle$ has $\mu = -\mu_B$, where μ_B is the Bohr magneton.

(a) Momentum offset
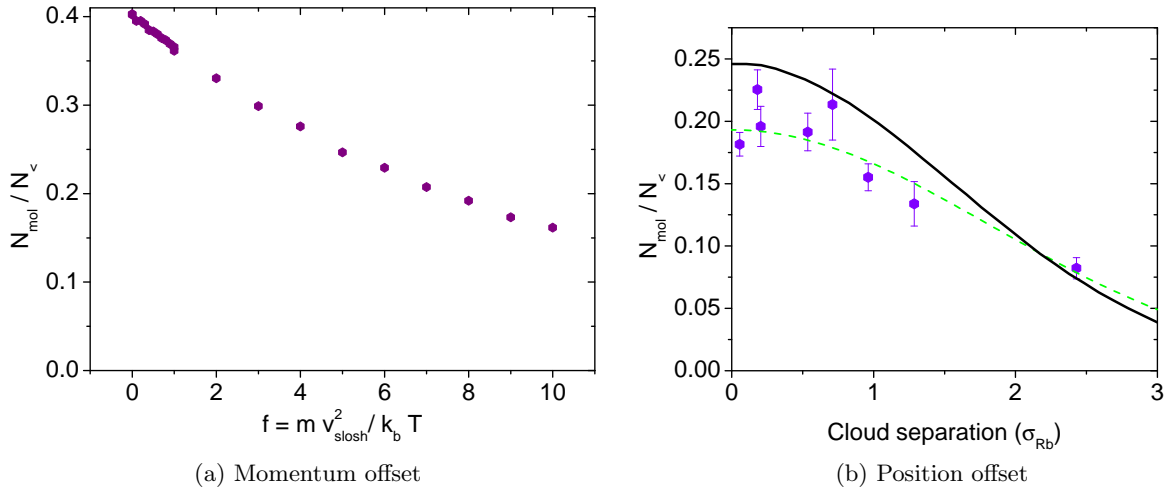
(b) Position offset

Figure 3.10: (a) Simulated molecule creation efficiency with an axial momentum offset between the Rb and K clouds, and no added position offset other than gravitational sag. The simulation was run for $N_K = N_{Rb} = 10^5$ and $T/T_c = 1.3$ with the assumption that the K and Rb clouds were in thermodynamic equilibrium. For conditions in the experiment, $f < 0.2$ and thus we conclude that slosh is a negligible concern. (b) Measured molecule creation efficiency as a function of the axial offset between the Rb and K clouds before molecule production. The atom clouds were separated by applying an axial magnetic-field gradient that was abruptly turned off before the magnetic-field was swept across the Feshbach resonance. The solid line is the simulation results using the atom conditions and the dashed line is a fit of the data to a gaussian.

Results for simulating the effect of axial slosh on the molecule creation efficiency are shown in Fig. 3.10a. The simulation was performed for 10^5 atoms of each species at $T/T_c = 1.3$. As can be seen, the reduction in molecule creation efficiency does not become significant until the slosh kinetic energy is on the order of the temperature. Thankfully the amount of slosh that typically occurs in the experiment corresponds to $\frac{m_{Rb}\, v_{slosh}^2}{k_B\, T} \lesssim 0.2$, which has negligible impact on the molecule creation efficiency.

Heteronuclear systems can also be subject to relative position offsets between the atom clouds due external forces acting differently on the two atom species. To simulate the importance of this effect, distributions with 2.00×10^5 atoms of K and 2.85×10^5 were generated with $T/T_c = 1.46$ for a K (Rb) radial trap frequency of 627 Hz (448 Hz) with an aspect ratio of $\lambda = 0.0131$. Before the molecule formation code is run, a relative position offset is added to the Rb cloud that is

a fraction of the calculated Rb gaussian cloud size. The solid curve in Fig. 3.10b is the result of this simulation. To realize this in the experiment, $2.85(12) \times 10^5$ Rb atoms in the $|1, 1\rangle$ state and $2.00(7) \times 10^5$ K atoms in the $|9/2, -9/2\rangle$ state were prepared at $T/T_c = 1.46(5)$ in an optical trap with the same frequencies as the simulation. Because the $|1, 1\rangle$ and $|9/2, -9/2\rangle$ states have different magnetic moments, an axial offset between the two clouds could be produced by applying an axial magnetic-field gradient across the cloud. The magnetic-field gradient was abruptly shut off shortly before the magnetic-field sweep to associate the Feshbach molecules. The measured molecule fraction was then fit to a gaussian (dashed line) returning a rms width of 1.8(1) σ_{Rb}. Given that the measured cloud offset in this trap is 30 μm = 0.17 σ_{Rb}, the reduction in molecule creation efficiency is likely a small effect in our measurements. In other heteronuclear alkali systems with large mass ratios (e.g. Li-Cs), this might not be the case.

3.5.3.2   Generating molecules in expansion

The SPSS model does not include the three-body effects. Three-body recombination, as the magnetic field transits through the Feshbach resonance, results in either a weakly or deeply bound molecule being formed, with its binding energy being converted into the kinetic energy of the third atom and the newly bound dimer. Strong losses and heating can occur from crossing through the Feshbach resonance. Since three-body recombination rates in a two-species gas scale as $n_1^2 \, n_2$, reducing the atom density will ameliorate the heating and losses. This reduction in density can be had by a combination of confining the atoms more weakly , reducing the atom number, working at higher temperatures, etc. These methods have the drawback of creating a lower signal-to-noise ratio for measuring molecules. Alternatively, the clouds can be diabatically released from the trap and allowed to expand. Assuming ballistic expansion, the peak atom densities would decrease by roughly a factor of ten compared to the in-trap density after a millisecond of expansion for the trap frequencies considered in Fig. 3.11.

Shown in Fig. 3.11 are the results of simulating the dependence of the molecule formation efficiency on ballistic expansion. Ballistic expansion was simulated by propagating the individual
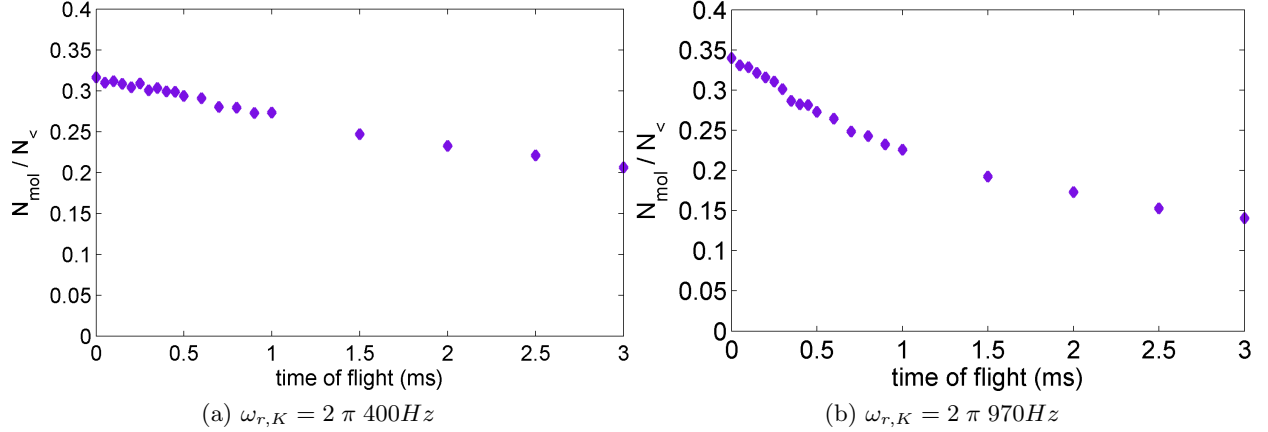
Figure 3.11: Simulated molecule creation after varying periods of ballistic expansion after releasing from a harmonic trap with aspect ratio $\lambda = \omega_z/\omega_r = 0.0131$. The atom clouds were generated for $N_K = N_{Rb} = 3 \times 10^4$ with $T/T_c = 1.5$ and the assumption of thermodynamic equilibrium between Rb and K clouds. Note that the discrepancy in molecule creation efficiency between a) and b) is due to greater significance of gravitational sag in the weaker trap of a).

atom positions according to their velocity for an amount of time ('time-of-flight' in Fig. 3.11). As can be seen in Fig. 3.11, the molecule creation efficiency decreases slowly, even though the peak densities vary by a factor of roughly 60 (30) for K (Rb) in the case of Fig. 3.11a. One thought as to why there is such a weak dependence is that as the clouds expand the atoms begin to segregate in terms of velocity. This creates a "local cooling" effect where atoms in a given location in the cloud have very similar momenta, which prolongs the efficiency of molecule creation. Since Rb and K atoms have different masses, Rb and K atoms with similar momenta will gradually move further apart as the cloud expands thus making association less likely to occur. This simulation indicates that molecule creation efficiency should remain high well into expansion, although the actual experiment is a bit more complicated due to the finite duration of the magnetic-field sweeps (which is not taken into account by the SPSS model) and interactions during expansion.

3.5.4 Theoretical optimization of Feshbach molecule degeneracy

The SPSS model can also provide guidance for the experimentalist who desires to create the most degenerate sample of Feshbach molecule given the constraints of their apparatus. This
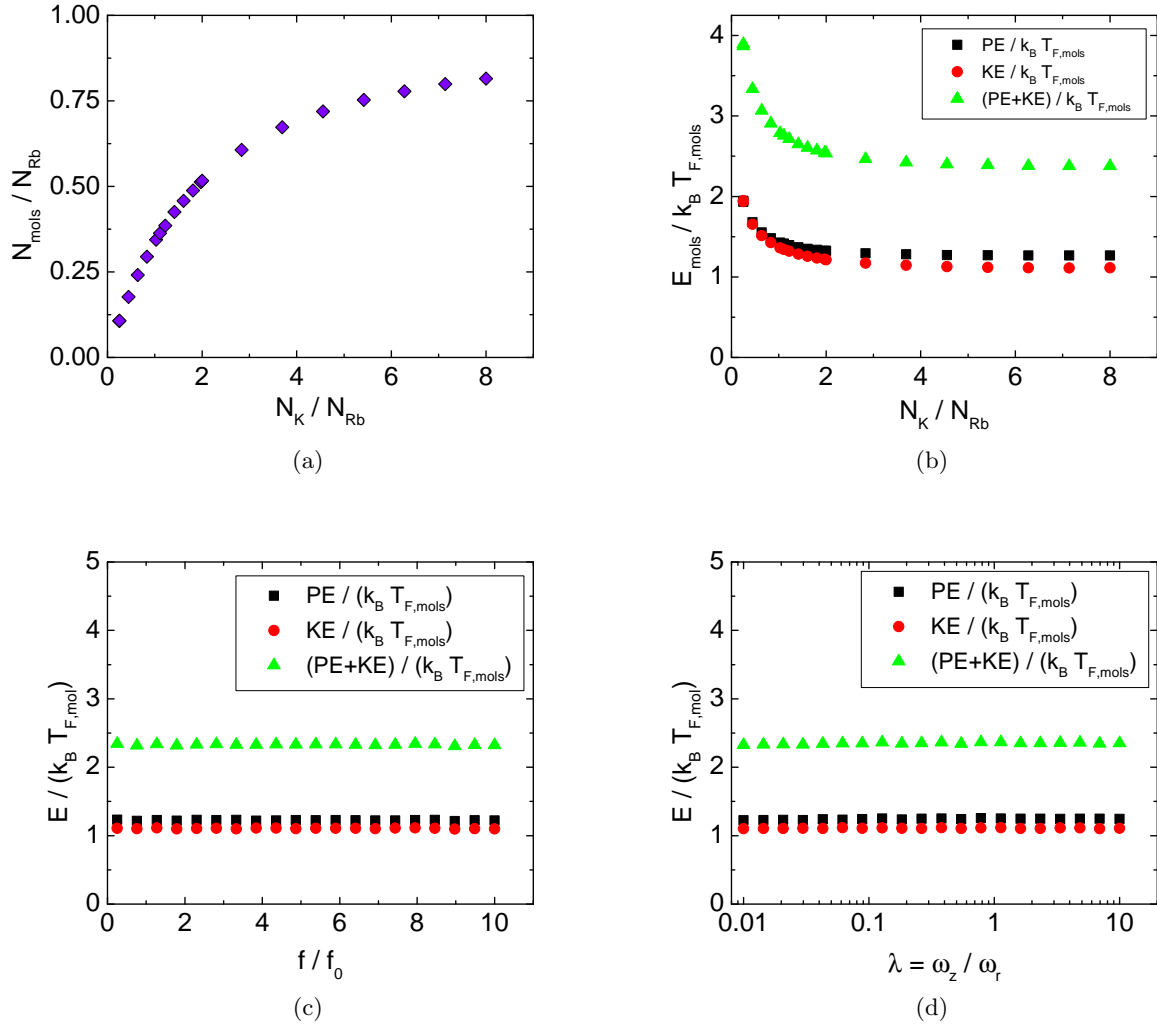
Figure 3.12: a) Molecule fraction as a function of the K atom number to Rb atom number ratio for fixed $N_{Rb} = 10^5$ and T/T_c=1.05. b) Average molecular potential energy per particles (PE), kinetic energy (KE), and total energy (PE+KE) compared to the molecular Fermi energy as a function of N_K/N_{Rb}. c) Molecular E/E_F versus trap frequency for fixed atomic T/T_c and T/T_F. d) Molecular E/E_F versus trap frequency aspect ratio.

goal is complicated in mixture systems by the inelastic collisions with unbound atoms. As will be shown in the next chapter, near the Feshbach resonance Rb is the dominant collision partner with the Feshbach molecules; the collision event rate between Rb and Feshbach molecules is roughly an order of magnitude higher than K and Feshbach molecules. The general strategy is then to look for conditions where the K atom number greatly outnumbers the Rb atom number.
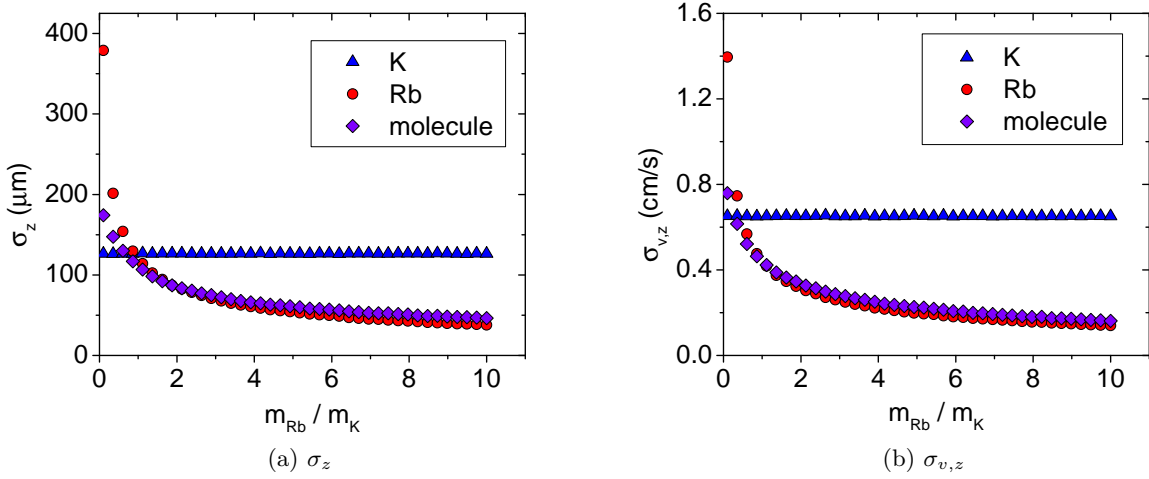
Figure 3.13: a) Axial rms cloud size versus the Rb to K mass ratio. b) Axial rms velocity spread versus the Rb to K mass ratio.

First we consider the case of fixed Rb number, trap frequencies, and T/Tc = 1.05, while allowing the K atom number to vary. In this simulation, the K and Rb atom distributions are in thermal equilibrium. The radial and axial trap frequencies for K are 627 Hz and 8 Hz, respectively; Rb has radial and axial trap frequencies of 448 Hz and 6 Hz, respectively. The results of this simulation are shown in Fig. 3.12 for a range of fixed Rb numbers. As can be seen in Fig. 3.12a, the Rb conversion fraction favors high K atom numbers, which leaves little Rb left over after association. This simulation also predicts that the molecule E/E_F saturates at its lowest value for high K to Rb number ratios, as shown in Fig. 3.12b.

In Figs. 3.12c and 3.12d are the simulation results where the geometry of the trap was varied for fixed atom numbers ($N_K = 10 \times N_{Rb} = 10^5$), $T/T_c = 1.05$, and $T/T_F = 0.18$, in the absence of the relative vertical offset between the Rb and K clouds due to gravitational sag. In Fig. 3.12c the trap frequency aspect ratio, $\lambda = \omega_z/\omega_r$, was fixed, but the trap frequencies for both Rb and K were scaled, whereas for Fig. 3.12d the radial trap frequencies were fixed, but λ was varied. As can be seen, the molecular E/E_F is independent of the frequencies and aspect ratio of the trap.

The result in Fig. 3.12b leaves the question of what is setting the energy of the molecules.

To address this question we look at the velocity spread, as well as the cloud sizes, for the atom and molecule clouds by fitting the momentum and spatial density distributions to gaussian distributions to extract rms widths. For the case of thermal clouds the velocity and spatial rms widths are $\sigma_z = \sqrt{\frac{k_B T}{m \omega^2}}$ and $\sigma_v = \sqrt{\frac{k_B T}{m}}$, respectively, for particles of mass m and trap frequency ω. If we vary the Rb atomic mass, while keeping the K atomic mass, trap frequencies, temperature, and $\mathrm{T/T_c}$ fixed with $N_K = 10 \times N_{Rb} = 10^5$, the simulation returns the results shown in Fig. 3.13 for the axial cloud width, σ_z, and axial velocity spread, $\sigma_{v,z}$. As can be seen in both Fig. 3.13a, the molecule widths (violet diamonds) closely follow whichever width is smallest. This result is understandable given that the molecule association criterion (Eqn. (3.5.1)) is expressed entirely in terms of relative coordinates of velocity and distance. This restriction on the relative separation in position and velocity means that the distribution with the smaller width will dictate the subsequent width for the molecules.

One possible way to gain better cloud overlap, and hopefully a more degenerate Feshbach cloud, might be to adiabatically compress the fermionic atom cloud such that the overlap with the bosonic cloud is better. The results simulating this experiment are shown in Fig. 3.14 using the trap frequencies listed above for $N_K = 10 \times N_{Rb}$ with $\mathrm{T/T_c} = 1.05$ and $\mathrm{T/T_F} = 0.18$ at $f_0 = 627$ Hz for K. In this simulation the adiabatic compression is assumed to progress faster than the rethermalization time scale with the Rb cloud such that only the K cloud heats as a consequence of the compression. The reduction of the K cloud size can be seen in Fig. 3.14a, but as the cloud is compressed further, the cloud is heated and the velocity spread increases. As the K cloud is compressed further and heats more, the number of K atoms able to pair with the Rb atoms decreases and the molecule fraction is lower as a consequence, which can be seen in Fig. 3.14c.

The resulting average energies of the molecules is shown in Fig. 3.14d, where the ensemble average potential energy (PE) is shown as black squares, average kinetic energy (KE) as red circles, the average total energy (PE+KE) as green upwardly pointing triangles, and the computed molecule $\mathrm{T_F}$ as blue downwardly pointing triangles [11] . As the K cloud is compressed further, the

---

[11] For $f_{r,K}/f_0 < 0.5$ relative gravitational sag between the Rb and K clouds becomes important.
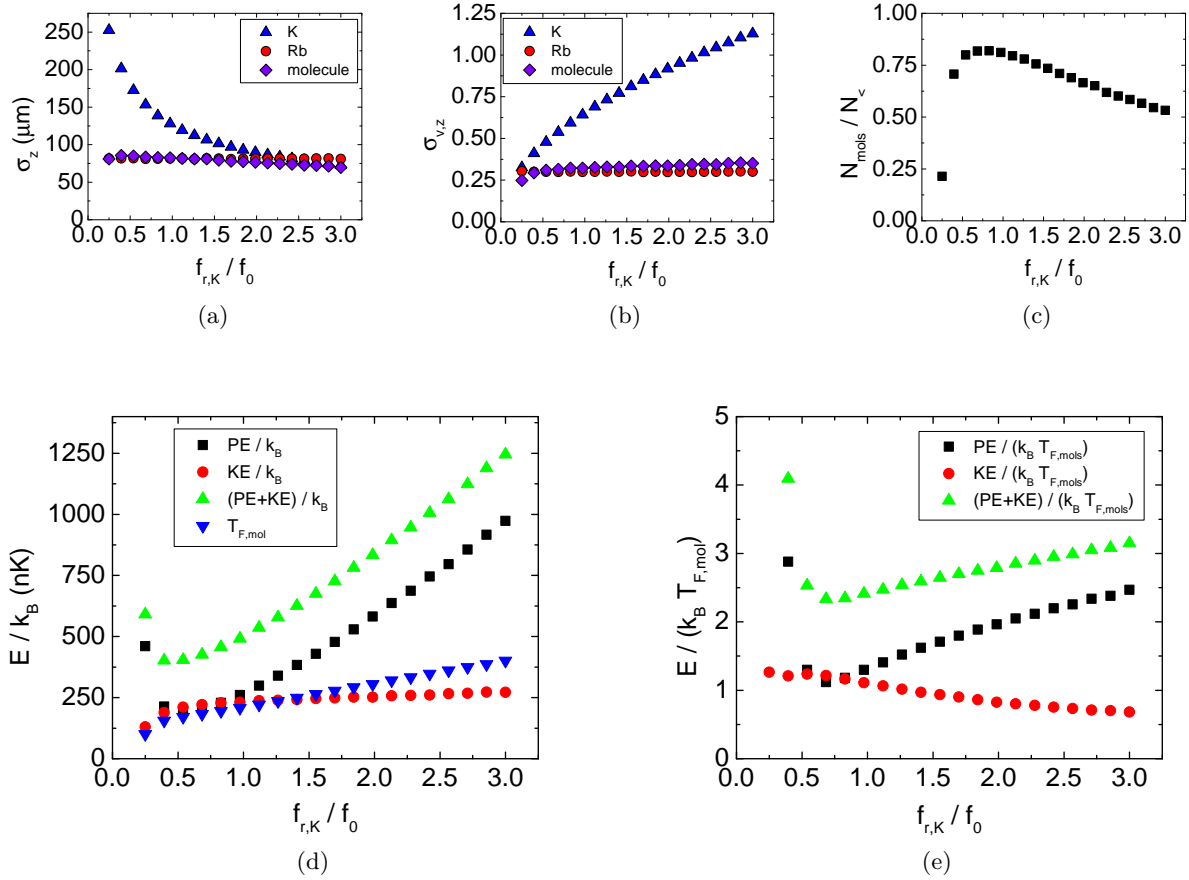
Figure 3.14: a) Axial rms cloud size for K atoms (blue triangles)), Rb atoms (red circles), and molecules (violet diamonds) versus the frequency of the compressed K trap. b) Axial velocity spread for K atoms, Rb atoms and molecules. c) Molecule conversion fraction. d) Molecular potential energy (PE), kinetic energy (KE), total energy (PE+KE), and Fermi temperature (T_F). e) Ratios of PE, KE, and (PE+KE) to the Fermi temperature.

Fermi temperature of the molecules increases since the reduction in molecule creation efficiency is weak. While the average molecular kinetic energy is only weakly affected by the compression, the potential energy, and the total energy, increases dramatically with the compression. Hence the ratio $(PE+KE)/k_B T_{F,mols}$ increases with the trap frequency and never approaches the value for a degenerate Fermi gas: $PE+KE = \frac{3}{4}k_B T_{F,mols}$ [132]. Therefore, even if the molecules were able to thermalize with a bath and survive the collisions, compression would not lead to a more degenerate molecular gas.

Chapter 4

The search for Efimov Physics in ^{40}K-^{87}Rb

In addition to the two-body bound state induced by the Feshbach resonance, in many atomic systems there also exist three-body (and 4-body [153, 56, 170, 129] and perhaps even higher n-body [67, 152, 151]) states in the vicinity of the Feshbach resonance. These other bound states are a consequence of the Efimov effect, which was originally discussed in terms of bound states amongst three nucleons (i.e. the ^{3}H nucleus) and three α particles (i.e. the ^{12}C nucleus) [48]. The Efimov states arise from strong two-body interactions near the Feshbach resonance. Curiously, the Efimov bound states exist on both sides of the resonance, for positive and negative two-body scattering lengths. Another remarkable feature is that the Efimov states exist not as a single bound state, but as a theoretically semi-infinite ladder of states with a discrete scaling symmetry between the different rungs.

Signatures of Efimov trimers were not observed until 35 years after Efimov's prediction; the observation was made in an ultracold gas of cesium by the Innsbruck group [92] through resonantly enhanced three-atom inelastic collisions. Following the Innsbruck group, Efimov resonances were observed in ^{39}K by the LENS group [170], in ^{7}Li by the Rice [129] and Bar-Ilan [64] groups, in a three spin-state mixture of ^{6}Li by the Penn State [165] and Heidelberg [163] groups, and recently in a ^{41}K $-$ ^{87}Rb mixture by the LENS group [7]. In ^{39}K, and later in ^{7}Li, the log-periodic scaling of the Efimov spectrum in ^{39}K was measured from the locations of the first two Efimov features. The authors of Ref. [170] measured a scaling of 25(4) in agreement with theory (22.7). Additionally, the energy of the lowest Efimov state has been mapped out for positive scattering lengths through

rf-association in a three spin-state mixture of ^{6}Li[101, 111] as well as in ^{7}Li[105].

One of the remarkable discoveries of this line of research is with regards to the location of the first Efimov bound state. Originally it was thought that the three-body parameter that sets the first state's location was a mixture of two- and three-body physics and therefore a priori calculation of the location was not possible. In ^{7}Li, Efimov resonances where found near two Feshbach resonances that involved different atomic hyperfine states and the locations of the associated Efimov resonances were found at the same location [65]. Additionally, the Innsbruck group measured the locations of the first Efimov resonance at four Feshbach resonances and found their locations to clustered about an average far more tightly than the scaling factor of 22.7 in scattering length between different rungs of the Efimov state ladder [12]. These two observation suggested that the location of the first Efimov resonance was in fact determined by two-body physics (i.e. the length scale of the two-body potential, the van der Waals length r_{vdW}) and the authors of reported the locations to be $a_-^{(1)} = -9.1(4)r_{vdW}$. This view of the three-body parameter being universally determined by two-body physics was corroborated in other homonuclear gas systems [23] and provided theoretical support for the case of broad Feshbach resonances [23, 155]. One remaining question is whether the three-body parameter in heteronuclear systems is also universally determined by r_{vdW}. Since ^{40}K – ^{87}Rb and ^{41}K – ^{87}Rb have very similar values of r_{vdW}, our system is well positioned to address the question of a universal three-body parameter.

In this chapter we will discuss our observations of Efimov resonances in a mixture of ^{40}K and ^{87}Rb atoms. The contents of this chapter are the subject of a manuscript in preparation [28] for publication. Section 4.1 will review fundamental physics of Efimov resonances and Section 4.2 will give a brief overview of how Efimov resonances are observed through inelastic collisions rates. In Sections 4.3 and 4.4 discusses our analysis methods to extract the inelastic collision rates from three-body recombination and atom+molecule relaxation, respectively. Next the observations will be compared against theoretical relations between different features in Section 4.5 and lastly we will compare the Efimov resonances in ^{41}K-^{87}Rb and ^{40}K-^{87}Rb in Section 4.6 to address the question of a universal three-body parameter in heteronuclear systems.

4.1 The Efimov effect and discrete scaling

In 1970 Efimov derived the effective attractive three-body interaction in the limit of strong two-body interactions and the associated ladder of three-body bound states that bears his name. Efimov derived the effective potentials for the three identical bosons, where the lowest-energy potential is an attractive $1/R^2$ and the infinite number of higher potentials are repulsive $1/R^2$ potentials [18]. The ladder of states is a consequence of the attractive $1/R^2$ three-body potential that arises for certain collision partners (e.g. three identical bosons, more discussion below) in the limit of strong repulsive or attractive interactions. For the general case of three particles with unequal masses, with at least two particles interacting strongly, the effective three-body potential is [18]

$$V_{eff}(R) = -\frac{(s_0^2 + \frac{1}{4})\,\hbar^2(m_1 + m_2 + m_3)}{2(m_1\,m_2 + m_2\,m_3 + m_3\,m_1)\,R^2}, \quad r_{vdW} \ll R \ll |a|. \tag{4.1.1}$$

where R is the hyperradius[1] and the parameter s_0 characterizes not only the potential strength, but also the periodicity of the Efimov ladder. The values that s_0 assumes depend strongly on the masses and spin statistics of the particles[2]. An interesting aspect of the Efimov effect is that the three-body system in the limit of strong two-body interactions exhibits a discrete scaling symmetry. One part of this symmetry is that in the limit a$\to \pm\infty$, the trimer binding energies corresponding to different bound states are related by $E_T^{(n)}/E_T^{(n+1)} = \exp{(-2\pi/s_0)}$. This would seem to indicate that the trimer binding energies are unbounded, but as part of the derivation for the Efimov effect the assumption that $|a| \gg r_{vdW}$ is made. This enforces a minimum length scale given by r_{vdW}, or alternatively, an energetic cutoff $\hbar^2/(2\mu_{2b}r_{vdW}^2)$ of the Efimov trimer binding energy ladder; any trimer states past the energetic cutoff would no longer follow the discrete scaling symmetry.

This energetic cutoff terminates the ladder of trimer states from below. The energy of the lowest Efimov state is defined by the three-body parameter, κ_*, which has units of wavenumber.

---

[1] The hyperradius is rms size of the three-body system. For the general three-body system $R^2 = \frac{m_1\,m_2\,r_{12}^2 + m_2\,m_3\,r_{23}^2 + m_3\,m_1\,r_{31}^2}{m_1\,m_2 + m_2\,m_3 + m_3\,m_1}$ [18].

[2] For example for three strongly interacting equal mass particles, $s_0 \approx 1.00624$. However, for two identical bosons colliding with a third equal mass non-identical particle with only two of the three scattering lengths being large, then $s_0 = 0.4137$.

Collision type	a_{ij} large	a_{ij}, a_{jk} large	a_{ij}, a_{jk}, a_{ki} large
BBB	N/A	N/A	Yes
BBX	No	Yes	Yes
XYZ	No	Yes	Yes
FFX	No	Yes[a]	N/A

[a] This is true iff $m_F/m_X > 13.61$ [71, 41, 127].

Table 4.1: Classes of collisions and whether or not Efimov states exist when one, two, or all three inter-particle scattering lengths (a_{ij}, a_{jk}, a_{ki}) are large compared to r_{vdW}, the length scale of the two-body potential.

The three-body parameter is defined such that

$$E_T^{(n)} \to \exp\left(-2n\pi/s_0\right) \frac{\hbar^2 \kappa_*^2}{2\mu_{2b}} \text{ as } a \to \pm\infty. \tag{4.1.2}$$

where μ_{2b} is the two-body reduced mass.

In Ref. [18], the authors derive the trimer binding energy for the three identical bosons case. The general three-body system consists of three atoms with masses m_1, m_2, and m_3 with any mixture of bosons, fermions, and distinguishable particles. We can classify three-body systems into those with two identical bosons and a distinguishable particle (BBX), two identical fermions and a distinguishable particle (FFX), three identical bosons (BBB), three identical fermions (FFF), and three distinguishable particles (XYZ). The general three-body system then has three inter-particle scattering lengths (a_{12}, a_{23}, and a_{31}). The Efimov effect occurs only when two or more of the inter-particle scattering lengths are large compared to the two-body potential range [2, 49], as summarized in Table 4.1. In our system we have both FFX and BBX collisions, but, given that $m_K/m_{Rb} = 0.46 < 13.61$, only the BBX collision channel supports Efimov states.

The trimer binding energy E_T for three identical bosons of mass m is given by [18]

$$E_T^{(n)} + \frac{\hbar^2}{m\,a^2} = (e^{-2\pi/s_0})^n \, \exp\left[\Delta(\xi)/s_0\right] \frac{\hbar^2 \kappa_*^2}{m}, \, n = 0, \, 1, \, 2, \, \ldots \tag{4.1.3}$$

where the angular argument, ξ, to Efimov's universal function, $\Delta(\xi)$, is defined by

$$\tan(\xi) = -(m\,E_T/\hbar^2)^{1/2}\,a. \tag{4.1.4}$$

The angular argument ξ spans the range from $\xi = -\pi$, corresponding to three-atom threshold at $E_T = 0$, to $\xi = -\frac{\pi}{4}$, where the trimer energy reaches the atom+dimer threshold for which $E_T = \frac{\hbar^2}{m\,a^2}$. The function $\Delta(\xi)$ is not known to have an analytical form and has been calculated numerically for identical bosons in Ref. [19] where $\Delta(\xi)$ is found to vary monotonically from $\Delta(-\pi) = -0.89$ to $\Delta(-\pi/4) = 6.04$. There does not exist a similar published calculation for the BBX system, but to get a qualitative picture of what the Efimov trimer energies look like in our system we will adapt Eqn. (4.1.3) by replacing the mass m with twice the two-body reduced mass, $2\mu_{2b}$. Eqn. (4.1.3) then becomes

$$E_T + \frac{\hbar^2}{2\mu_{2b}\,a^2} = (e^{-2\pi/s_0})^n\,\exp\left[\Delta(\xi)/s_0\right]\frac{\hbar^2\,\kappa_*^2}{2\mu_{2b}}, \; n = 0,\,1,\,2,\,\ldots \tag{4.1.5}$$

The value for s_0 can be calculated for the BBX system from a transcendental equation:[18]

$$\cosh(s_0\pi/2) - \frac{2\sinh[s_0(\pi/2 - \gamma_{12})]}{s_0\,\sin(2\gamma_{12})} = 0 \tag{4.1.6}$$

where the angle γ_{12} satisfies $\tan\gamma_{12} = \left(\frac{m_3(m_1+m_2+m_3)}{m_1\,m_2}\right)^{1/2}$. For this system $m_1 = m_2 = m_{Rb}$, $m_3 = m_K$, $a_{23} = a_{31} = a_{KRb} = a$, and $a_{12} = a_{RbRb}$; Eqn. (4.1.6) gives $s_0 \approx 0.65317$ for ^{87}Rb $-$ ^{87}Rb $-$ ^{40}K.

The trimer binding energy for the lowest two Efimov states is shown in Fig. 4.1 for ^{87}Rb $-$ ^{87}Rb $-$ ^{40}K using the published calculation of $\Delta(\xi)$[19, 18] for identical bosons[3] . In the figure the lowest two trimer energies (solid orange curves) are plotted as a function of $1/a$. For this figure, $E = 0$ represents the three-atom threshold, above which the system consists of three colliding atoms. The universal dimer binding energy (black dashed curve) demarcates the atom-dimer threshold, where between the atom-dimer threshold and $E = 0$ the system consists of a mixture of dimers and atoms. At a scattering length $a_-^{(n)} < 0$, the n-th trimer state terminates at $E_T = 0$. $E_T^{(n)}$ reaches the atom-dimer threshold at a scattering length $a_*^{(n)} > 0$. Additionally at scattering lengths $a_+^{(n)} > 0$ quantum mechanical interference occurs, which will be discussed below in Section 4.2.

---

[3] Although this does not give the correct scalings between features on opposite sides of the Feshbach resonance, it does give the qualitative features of the Efimov states.
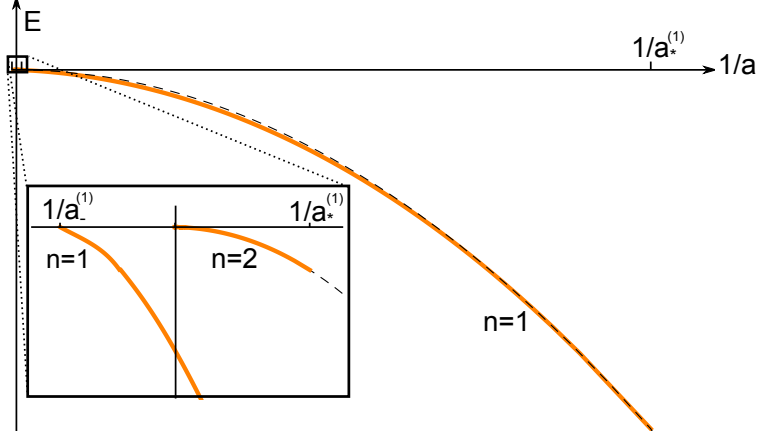
Figure 4.1: Schematic of the binding energy of the lowest two Efimov states (solid orange curves) plotted along with the dimer binding energy (dashed black curve) for $s_0 = 0.65317$. The inset is a magnified view of the origin showing where the lowest Efimov state (n = 0) reaches the atom threshold (a = $a_-^{(0)}$) as well as the entirety of the next-to-lowest Efimov state(n = 1).

Figure 4.1 shows the discrete scaling symmetry characteristic of Efimov states. This scaling symmetry involves a particular value of κ_* where the system is unchanged by transformations of the form

$$\kappa_* \to \kappa_*,\ a \to \zeta a,\ E_T \to \zeta^{-2} E_T \tag{4.1.7}$$

where the scaling factor $\zeta = \exp(\pi/s_0) \approx 122.7$ for $^{87}\text{Rb} - ^{87}\text{Rb} - ^{40}\text{K}$. This symmetry creates a relation between the n-th and (n+1)-th trimer state of the form

$$E_T^{(n+1)}(a) = \zeta^{-2}\, E_T^{(n)}(\zeta a) \tag{4.1.8}$$

as well as for $a_*^{(n)}$ and $a_-^{(n)}$

$$a_*^{(n+1)} = \zeta a_*^{(n)} \approx 122.7 a_*^{(n)} \tag{4.1.9}$$

$$a_-^{(n+1)} = \zeta a_-^{(n)} \approx 122.7 a_-^{(n)}. \tag{4.1.10}$$

The relation between $a_*^{(n+1)}$ and $a_-^{(n)}$, as well as $a_+^{(n)}$ and $a_-^{(n)}$, was calculated in Ref. [72] to be

$$a_*^{(n+1)}/|a_-^{(n)}| = 0.51 \tag{4.1.11}$$

$$|a_-^{(n)}|/a_+^{(n)} = e^{\pi/2s_0} \tag{4.1.12}$$

using a zero-range (i.e. $r_{vdW} = 0$) effective field theory.

As one might expect, there are limitations to the number of Efimov states we can observe due to a finite range of accessible scattering lengths. The lower limit is imposed by the aforementioned limit of strong interactions, namely $a \gg r_{vdW}$. The upper limit is essentially set by the point where the scattering length becomes of order of the interparticle spacing. This limit corresponds to the point $k_{\text{thermal}} a \sim 1$, where $k_{\text{thermal}} = \sqrt{2 m_{3\text{body}} k_B T / \hbar^2}$ [43] where the three-body reduced mass is defined as $m_{3\text{body}} = \sqrt{\frac{m_1 m_2 m_3}{m_1 + m_2 + m_3}}$ [41]. For the data shown below, the temperature is typically 250 nK, which means that the scattering lengths we can span are limited to $r_{vdW} = 72\, a_0 < |a| < 3000\, a_0$. Given this limitation and the scaling factor of 122.7, we will at best be able to measure one feature each from the a_-, a_*, and a_+ series.

4.2   Observation of Efimov resonances

In order to address the question of whether the three-body parameter for heteronuclear system is universal, we set out to look for Efimov resonances. Observation of Efimov resonances can be made through their influence on inelastic collision rates [10, 17, 53, 114, 18] since the presence of the trimer state increases the likelihood of several particles being close together. One such inelastic process is three-body recombination where three atoms collide resulting in the creation of a molecule. In atomic systems, there exist both shallowly bound molecule states (i.e. a Feshbach molecule, for $a > 0$ only) as well as deeply bound molecule states, and so three-body recombination of particles A, B, and C in general has two possible paths:

$$A + B + C \rightarrow (AB)^* + C \tag{4.2.1}$$

$$\rightarrow (AB) + C \tag{4.2.2}$$
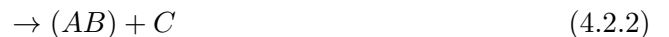
where (AB) denotes a deeply bound molecule and $(AB)^*$ a shallowly bound molecule. This collision releases an amount of energy equal to the binding energy of the molecule, which is carried away in the kinetic energy of the atom and molecule. Additionally, atom-molecule relaxation can occur where the shallowly bound dimer can collide with an atom and vibrationally relax into a more

deeply bound state. This results in

$$(AB)^* + C \rightarrow (AB) + C, \tag{4.2.3}$$

where again the binding energy difference between the deeply and shallowly bound molecule is carried away by the kinetic energy of the molecule and atom.

For the BBX system, the three-body recombination event rate per unit volume is of the form $\alpha n_B^2 \, n_X$, where the n_B is the density of identical bosons and n_X is the density of the distinguishable species. The event rate coefficient, α, is strongly dependent upon the scattering length and is defined by density loss rate equations[4] .

$$\frac{d}{dt} n_B = 2 \frac{d}{dt} n_X = -2\alpha \, n_B^2 \, n_X. \tag{4.2.4}$$

Similarly, the atom-dimer relaxation rate is defined in terms of an event rate constant, β,

$$\frac{d}{dt} n_A = \frac{d}{dt} n_D = -\beta n_A \, n_D \tag{4.2.5}$$

where n_A denotes the density of atoms and n_D the density of weakly bound molecules.

The authors of Ref. [72] derive expressions for the recombination rate for positive and negative scattering length in the BBX system with the assumption that the molecule binding energy has the universal form $E_D = \hbar^2/(2\mu_{2b}a^2)$, where μ_{2b} is the two-body reduced mass. The recombination coefficient is different for positive and negative scattering lengths in part because recombination into shallow dimers is possible only for positive scattering lengths. The three-body recombination coefficient, α, has the piece-wise form

$$\alpha = \begin{cases} \alpha_s + \alpha_d^{(+)} & a > 0 \tag{4.2.6} \\ \\ \alpha_d^{(-)} & a < 0 \tag{4.2.7} \end{cases}$$

with contributions from shallow (α_s) and deep dimers ($\alpha_d^{(\pm)}$). The coefficient for recombination into shallow dimers is [72]

$$\alpha_s = C(\delta) \frac{D \left\{ \sin^2[s_0 \, \ln(a/a_+)] + \sinh^2 \eta_* \right\}}{\sinh^2(\pi \, s_0 + \eta_*) + \cos^2[s_0 \, \ln(a/a_+)]} \frac{\hbar \, a^4}{m_X} \tag{4.2.8}$$

---

[4] This expression assumes that two bosonic atoms are lost per distinguishable atom. The ratio of loss can vary in cases where secondary collisions result in further loss. For example, if three-body recombination results in the weakly bound molecule remaining trapped, but the third atom not, then the molecule can collide with another atom and vibrationally relax with the loss of another atom. The loss ratio in this case can be between 1:1 to 3:1.

with $D = 128\pi^2(4\pi - 3\sqrt{3})$ and C(δ) is a coefficient that depends upon the mass ratio $\delta = m_X/m_B$.

For ^{87}Rb – ^{87}Rb – ^{40}K collisions, $\delta \approx 0.46$ and C(δ)≈ 0.037 [72]. Eqn. (4.2.8) exhibits minima[5] at

scattering lengths a = $a_+^{(n)}$ with the log-periodic spacing of $a_+^{(n)} = \exp(\pi/s_0)\, a_+^{(n-1)}$. The expression

for recombination into deeply bound dimers [72] is

$$\alpha_d^{(+)} = C(\delta)\, \frac{D \coth(\pi\, s_0) \cosh(\eta_*) \sinh(\eta_*)}{\sinh^2(\pi\, s_0 + \eta_*) + \cos^2[s_0 \ln(a/a_+)]} \frac{\hbar\, a^4}{m_X}, \tag{4.2.9}$$

which exhibits weak local extrema since $\sinh^2(\pi\, s_0) \gg 1 \geq \cos^2[s_0 \ln(a/a_+)]$. The coefficient for

recombination into deep dimers for negative scattering lengths is [72]

$$\alpha_d^{(-)} = \frac{C(\delta)}{2} \frac{D \coth(\pi\, s_0) \sinh(2\eta_*)}{\sin^2[s_0 \ln(a/a_-)] + \sinh^2(\eta_*)} \frac{\hbar\, a^4}{m_X}. \tag{4.2.10}$$

A plot of α is shown in Fig. 4.2 for a variety of values for η_* assuming $a_- = -1000a_0$ and the

relation between a_- and a_+ from Eqn. (4.1.12). The measured values of η_* span the range from

0.016 (in ^{6}Li [165]) to 0.251 (in ^{7}Li [65]).). From this plot, one can see the log-period scaling factor

of 122.7 as well as the higher sensitivity of $\alpha_d^{(-)}$ to η_* compared to $\alpha_d^{(+)}$ and α_s.

The other inelastic collision process that exhibits strong Efimov features is atom-dimer re-

laxation. The atom-molecule relaxation coefficient for a BBX system is

$$\beta = 2\pi C_2(\delta) \frac{\delta(\delta + 2)}{\delta + 1} \frac{\sinh(2\eta_*)}{\sin^2[s_0 \ln(a/a_*) + \sinh^2 \eta_*]} \frac{\hbar\, a}{m_X}, \tag{4.2.11}$$

where $C_2(\delta) = 2.08$ for ^{87}Rb – ^{87}Rb – ^{40}K [72]. The coefficient β exhibits strong peaks at a =

$a_*^{(n)}$, where the trimer binding energy intersects the atom-dimer threshold. Even though α is

expected to lack sharp features at a = $a_*^{(n)}$, various experiments have observed peaks in three-

body recombination on the a > 0 side, which were attributed to secondary relaxation events where

recombined shallow molecules relaxed into deeply bound molecules through collisions with a third

atom [129, 170, 7, 104, 105]. Although recent theoretical work questions this interpretation [95],

in ^{7}Li the location of this secondary collision peak agrees with a_* measured by mapping out the

trimer binding energy via rf-association [105].

---

[5] The source of these minima are an interference effect. Essentially, the incoming hyperradial wave function is a superposition between a state that feels the lowest repulsive $1/R^2$ potential and an atom-molecule state, which is in the attractive $1/R^2$ potential. The part of the wavefunction in the repulsive $1/R^2$ potential scatters at short distances and makes a nonadiabatic transition at long distances (R $\sim$ a) into the atom-molecule state where it destructively interferes with the part of the wavefunction in that was originally in that state[18].
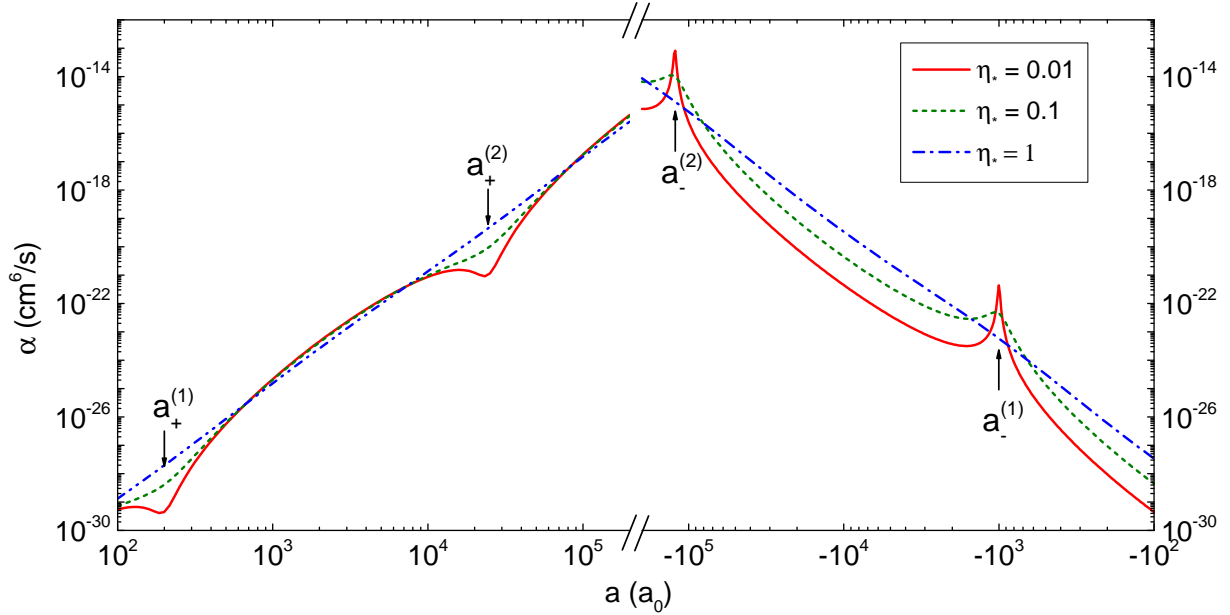
Figure 4.2: Three-body recombination event rate coefficient as a function of scattering length. The solid line corresponds to a value for the inelasticity parameter $\eta_* = 0.01$. The dashed and dash-dotted correspond to $\eta_* = 0.1$ and $\eta_* = 1$, respectively. Measured values of η_* span the range from 0.016[165] to 0.251[65].

4.3   Analysis of loss data to extract α

The process to measure α at a given magnetic field is fairly simple. We begin with a mixture of ^{87}Rb atoms in the $|1, 1\rangle$ hyperfine state and ^{40}K atoms in the $|9/2, -9/2\rangle$ hyperfine state with the magnetic field far from the Feshbach resonance where the inelastic loss time scales are long compared to our optical trap lifetime. The magnetic field is then ramped closer to resonance and held for a duration t_{hold}, as shown in Fig. 4.3a. At this field, the atoms undergo enhanced inelastic collisional loss. After the hold, the atoms are released from the optical trap (indicated by the vertical dashed line) and the magnetic field is ramped away from the Feshbach resonance. The remaining atoms are then imaged using standard absorption imaging, from which we extract the atom numbers and cloud sizes.

Fig. 4.3b shows a measurement of α at 548.695 G (a = -460 a_0), for initial in-trap density-weighted densities of $1.2 \times 10^{13}\,\mathrm{cm}^{-3}$ and $3.3 \times 10^{12}\,\mathrm{cm}^{-3}$ for Rb and K, respectively. The curves

(a) Magnetic-field sequence

(b) Number loss measurement
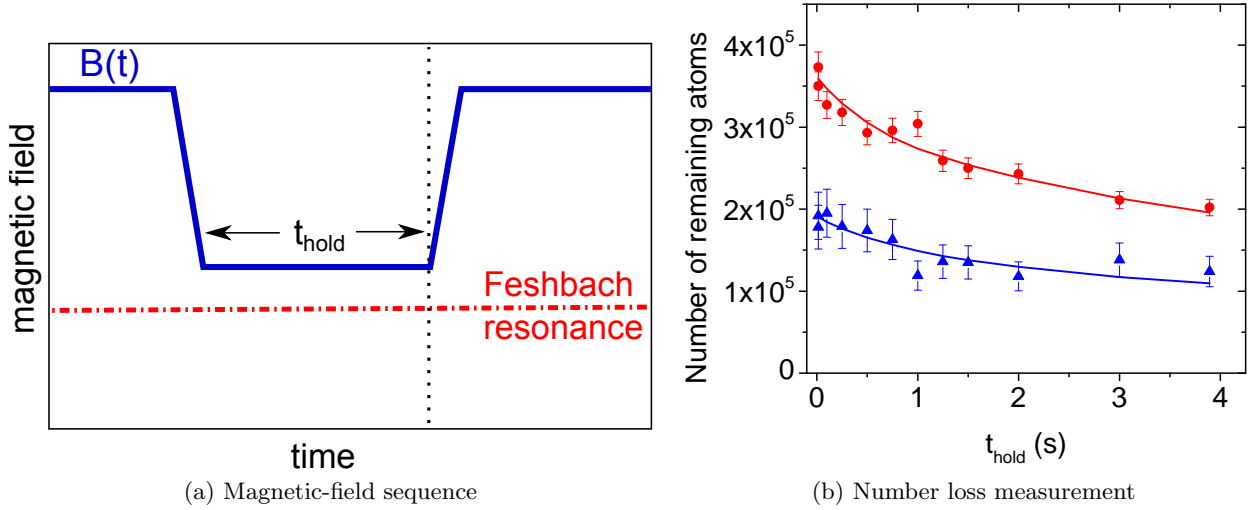
Figure 4.3: (a) Diagram of the magnetic-field sequence for measuring α. The magnetic field starts far from the Feshbach resonance and is ramped towards resonance where it is held for a duration t_{hold}. After the hold, the remaining atoms are released from the optical trap (vertical dotted line) and the magnetic field is ramped away from resonance. (b) Measurement of α at 548.695 G (a = -460 a_0) with initial in-trap density-weighted densities of 1.2×10^{13} cm^{-3} and 3.3×10^{12} cm^{-3} for Rb and K, respectively. The solid lines are from a dual-species fit described below. The fit returned $\alpha = 15.3(6) \times 10^{-27}$ cm^6.

correspond to a fit to the model developed below. We extract α from the atom number and cloud sizes using methods similar to those outlined in Refs. [21, 120]. To develop the three-body recombination model let's consider the K loss rate first. To begin we make the local density approximation for Eqn. (4.2.4) and divide through by $N_K(t')$ yielding

$$\frac{1}{N_K(t')}\frac{dn_K(r,t')}{dt'} = -\alpha \frac{n_{Rb}^2(r,t')n_K(r,t')}{N_K(t')}. \tag{4.3.1}$$

Next we integrate both sides over all space

$$\frac{1}{N_K(t')}\frac{dN_K(t')}{dt'} = \frac{d\ln(N_K(t'))}{dt'} = -\alpha \int d^3r \, \frac{n_{Rb}^2(r,t')n_K(r,t')}{N_K(t')} \tag{4.3.2}$$

and then integrate with respect to time, which results in

$$\int_0^t dt \, \frac{d\ln(N_K(t'))}{dt'} = \ln\left(\frac{N_K(t)}{N_K(0)}\right) = -\alpha \int_0^t dt' \int d^3r \frac{n_{Rb}^2(r,t') \, n_K(r,t')}{N_K(t')}. \tag{4.3.3}$$

Similarly for the Rb loss rate we find

$$\ln\left(\frac{N_{Rb}(t)}{N_{Rb}(0)}\right) = -2\alpha \int_0^t dt' \int d^3r \frac{n_{Rb}^2(r,t')\,n_K(r,t')}{N_{Rb}(t')}. \tag{4.3.4}$$

The spatial integrals on the right-hand side of Eqns. (4.3.3) and (4.3.4) are evaluated assuming a gaussian distribution. The expression for the spatial integral on the right-hand side of Eqns. (4.3.3) and (4.3.4) is then

$$\int d^3r\, n_{Rb}^2(r,t')\,n_K(r,t') = \frac{N_K(t')N_{Rb}^2(t')}{(2\pi)^3\,\sigma_{r,Rb}^4\,\sigma_{z,Rb}^2\,\left(2\sigma_{r,K}^2/\sigma_{r,Rb}^2 + 1\right)\,\sqrt{2\sigma_{z,K}^2/\sigma_{z,Rb}^2 + 1}}, \tag{4.3.5}$$

where $\sigma_{r,i}$ and $\sigma_{z,i}$ are the radial and axial rms cloud widths at time t', respectively, for species i. The time integrals are then discretely evaluated by a linear interpolation of the spatial integral at each measurement. For a function $f(t)$, the discrete evaluation of its integral with respect to t from t_1 to t_m is

$$\int_{t_1}^{t_m} dt'\, f(t') \approx \sum_{i=1}^{m-1} \frac{f(t_{i+1}) + f(t_i)}{2}(t_{i+1} - t_i). \tag{4.3.6}$$

A value of α is then extracted by performing a simultaneous least-squares fit of Eqns. (4.3.3) and (4.3.4) to a line, using Eqn. (4.3.6) to evaluate the time integrals with the measured atom number and sizes as inputs.

The results of these measurements are shown in Fig. 4.4 as a function of the magnetic field. For this Fano-Feshbach resonance, magnetic fields above 546.6 G or below 543.5 G correspond to negative scattering lengths. The data were taken with an initial temperature of T $\approx$ 250 nK as measured before the atoms were brought to the hold field. Other than the Fano-Feshbach resonance at 546.6 G, the only dramatic feature is the peak at 547.35(10) G [6] .

4.3.1   Identifying the feature at 547.4 G

The feature at 547.35(10) G could be due to a narrow Fano-Feshbach resonance or an Efimov resonance. Ref. [84] predicts a narrow d-wave Feshbach resonance (which couples to the s-wave scattering length) near the s-wave resonance, although the predicted location is roughly 1 G higher

---

[6] The 0.1 G width of this feature is probably due to the gas temperature and the experimental magnetic-field resolution.
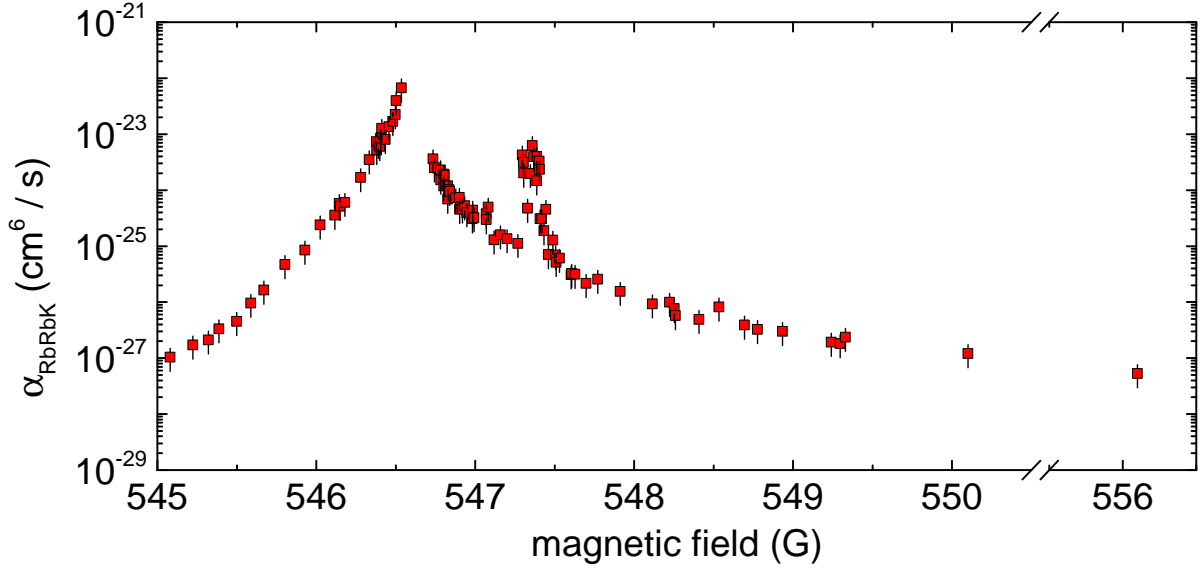
Figure 4.4: Measured three-body event rate coefficient, α, as a function of magnetic field.

than where we observe the peak in α. Zaccanti *et al.*, in studies of interactions between ^{40}K and ^{87}Rb, also observed a peak in number loss at 547.4(1) G [171] and they state that their model of the KRb potentials predicts a narrow Feshbach resonance at this field.

To see if the feature could be consistent with an Efimov resonance, we can also compare the shape of the observed feature in three-body recombination to the prediction of Eqn. (4.2.10), as shown in Fig. 4.5. In Fig. 4.5, the points correspond to the B > 546.6 G data replotted in terms of scattering length, a(B), is given by

$$a(B) = a_{bg}\left(1 - \frac{\Delta}{B - B_0}\right) \tag{4.3.7}$$

and is calculated by averaging the scattering lengths from the Feshbach resonance calibrations of Refs. [86] ($a_{bg} = -187\,a_0$, $B_0 = 546.618$ G, and $\Delta = -3.04$ G) and [117] ($a_{bg} = -185\,a_0$, $B_0 = 546.71$ G, and $\Delta = -3.34$ G). The hollow points are for scattering lengths where a > $1/\mathrm{k_{thermal}}$ and are excluded from the fit (solid curve). The least-squares fit of the data for $|a| < 890\,a_0$ to Eqn. (4.2.10) returns $\eta_* = 0.0167(7)$. For this fit, the log-periodic series of resonances in Eqn. (4.2.10) was truncated such that for scattering lengths $|a| \le e^{-\pi/(2s_0)}|a_-^{(1)}|$, $\alpha = Ca^4$. The constant C was
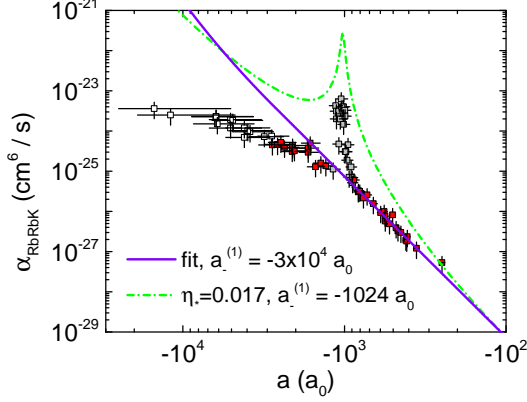
Figure 4.5: Comparison of negative scattering length data from Fig. 4.4 to a fit of Eqn. (4.2.10) (solid curve) and a plot of Eqn. (4.2.10) assuming $\eta_* = 0.017$ (dash-dotted curve). The fit was restricted to $|a| < 890 a_0$ with $a_-^{(1)} = -3 \times 10^4 a_0$ and returned $\eta_* = 0.0167(7)$.
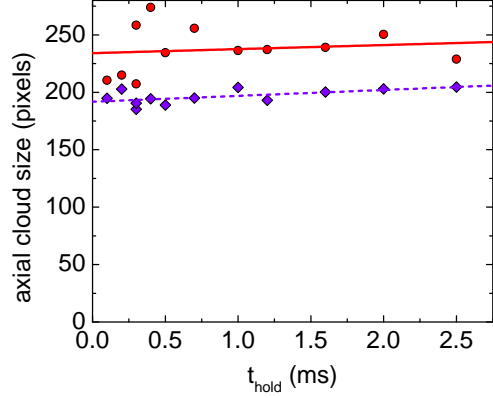
Figure 4.6: Axial cloud sizes for the Rb (red circles) and molecule (violet diamonds) clouds as a function of the hold duration in Fig. 4.7a.

determined by matching to Eqn. (4.2.10) at $a = e^{-\pi/(2s_0)} a_-^{(1)}$. For comparison Eqn. (4.2.10) is plotted (dash-dotted line) with the same value of η_*, but with $a_- = -1024 a_0$, which is centered on the points at 547.36 G. As can be seen, the peak in the data is substantially narrower than the peak of Eqn. (4.2.10) and attempts to use lower values of η_* in order to make the peak narrower only result in worse agreement at low scattering lengths (i.e. $|a| < 890 \, a_0$). Thus, we see that the three-body recombination feature at 547.36(10) G is not consistent with the expected shape of an Efimov feature. Therefore, we conclude that this peak is likely to be due to a narrow Feshbach resonance.

4.4   Extracting β from atom-molecule inelastic collisional loss

We extract values for β in a similar fashion to what was done for α. The analysis has to be changed slightly since when we image the molecules, we dissociate the molecules first by ramping the magnetic field to the unbound side. The molecule number is measured from the previously bound K atoms, but the Rb atom signal includes both bound and unbound atoms. Eqn. (4.2.5)

needs to be slightly modified: n_{Rb}, the unbound Rb density, is replaced by $n_{Rb} = \tilde{n}_{Rb} - n_{mol}$. The quantity $\tilde{n}_{Rb}$ is the density of bound and unbound Rb atoms, which what our Rb absorption images measure. The density rate equations for a homogeneous gas then become

$$\frac{d}{dt}\tilde{n}_{Rb} = 2\frac{d}{dt}n_{mol} = -2\beta\,n_{mol}\,(\tilde{n}_{Rb} - n_{mol}). \tag{4.4.1}$$

After making a local density approximation integrating over space, Eqn. (4.4.1) results in

$$\frac{dN_{mol}}{dt} = -\beta \int d^3r\,n_{mol}\,(\tilde{n}_{Rb} - n_{mol}). \tag{4.4.2}$$

We now make the approximation that the atom and molecule density distributions are gaussians at all times. The integrals on the right-hand side of Eqn. (4.4.2) becomes

$$\int d^3r\,n_{mol}\,(\tilde{n}_{Rb} - n_{mol}) = \frac{N_{mol}^2(t)}{8\pi^{3/2}\,\sigma_{r,mol}^2(t)\sigma_{z,mol}(t)}\left(\frac{\sqrt{8}\,N_{Rb}(t)/N_{mol}(t)}{\left(\frac{\sigma_{r,Rb}^2(t)}{\sigma_{r,mol}^2(t)}+1\right)\sqrt{\frac{\sigma_{z,Rb}^2(t)}{\sigma_{z,mol}^2(t)}+1}} - 1\right). \tag{4.4.3}$$

where the N_{Rb} is the total Rb number (i.e. both bound and unbound Rb) and the radial and axial rms sizes for species i are $\sigma_{r,i}$ and $\sigma_{z,i}$, respectively. The radial and and axial rms cloud sizes are measured and change in time due to effects such as anti-evaporation [7] . We observe that the cloud sizes initially vary linearly with time (c.f. Fig. 4.6); we fit the initial slope of σ vs. t and incorporate this into the numerical solution of Eqn. (4.4.2). With the cloud sizes and atom and molecule numbers as inputs, we fit the data to Eqn. (4.4.2), using Eqn. 4.4.3, to extract a value of β.

A sample measurement and the associated magnetic field trajectory are shown in Figs. 4.7b and 4.7a, respectively. We create molecules by sweeping the magnetic field across the Feshbach resonance. The magnetic field continues to 2G below the Feshbach resonance where the molecules are so deeply bound that they can be distinguished from atoms. The molecules at this field have a binding energy of approximately 2 MHz [174]. This allows for unwanted atoms to be cleared

---

[7] Given the strong dependence on density, three-body recombination preferentially removes atoms at the high density region near the trap center. Three-body recombination depletes the cloud of atoms with low potential energy, compared to the ensemble average, and therefore the new ensemble average potential energy is higher than before [160]. This process is termed "anti-evaporation".

(a) Magnetic-field sequence

(b) Rb+molecule collisions
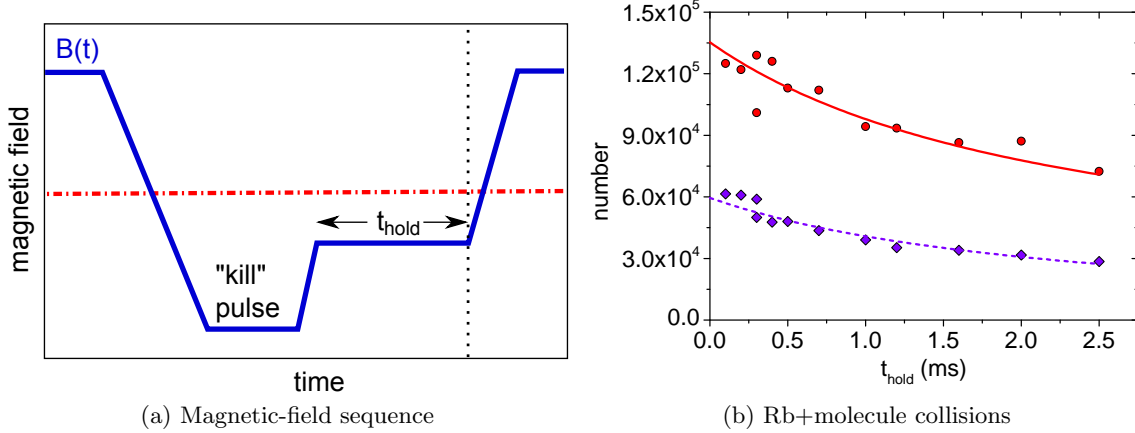
Figure 4.7: (a) Magnetic-field sequence for measuring atom-molecule collisional loss. First molecules are generated by sweeping slowly through the Fano-Feshbach resonance (dash-dotted line). Next, unwanted remaining atoms are heated out of the trap with resonant light. For removing K, we merely apply light resonant with $|9/2, -9/2\rangle - |11/2', -11/2\rangle$, but for Rb we ARP to the $|2, 2\rangle$ hyperfine state and apply light resonant with $|2, 2\rangle - |3', 3\rangle$. The magnetic field is then ramped to another field and held for a duration t_{hold} after which optical trap is extinguished. While the atoms and molecule are expanding, the molecules are dissociated by ramping back across the resonance. (b) Measured Rb (red circles) and molecule number (violet diamonds) after holding at 545.14 G (a = 200 a_0) with an initial temperature of 450 nK and a Rb density-weighted density of 2×10^{12} cm^{-3}. The molecule number is determined from imaging K atoms after dissociation. The measured Rb number after the dissociation of the molecules is the sum of the molecule number and Rb atoms that were never bound, which is the reason for the 2:1 Rb number to molecule number loss.

out of the trap with a combination of resonant light and rf. We can then selectively examine collisions between molecules and Rb atoms in the $|1, 1\rangle$ hyperfine state, K in the $|9/2, -9/2\rangle$ state, or distinguishable atoms, where ^{40}K atoms in the $|9/2, -7/2\rangle$ state served as our distinguishable atoms.

Shown in Fig. 4.8 are the results of measuring the atom-molecule loss rates for a wide range of magnetic fields. The data represented as circles are Rb (in the $|1, 1\rangle$ state) colliding with the molecules, the triangles are K (in the $|9/2, -9/2\rangle$) colliding with the molecules [8] , and the squares are distinguishable atoms (K in the $|9/2, -7/2\rangle$ state, whose scattering length is not resonant with either Rb atoms in $|1, 1\rangle$ or K atoms in $|9/2, -9/2\rangle$) colliding with molecules [9] . For the hollow

---

[8] Unbound Rb are removed by a "kill" pulse.

[9] To create this collision partner, unbound K atoms are transferred to $|9/2, -7/2\rangle$ with an ARP while unbound Rb is removed with a "kill" light pulse. After the dissociated molecules are imaged these K atoms are transferred back to the $|9/2, -9/2\rangle$ and imaged.
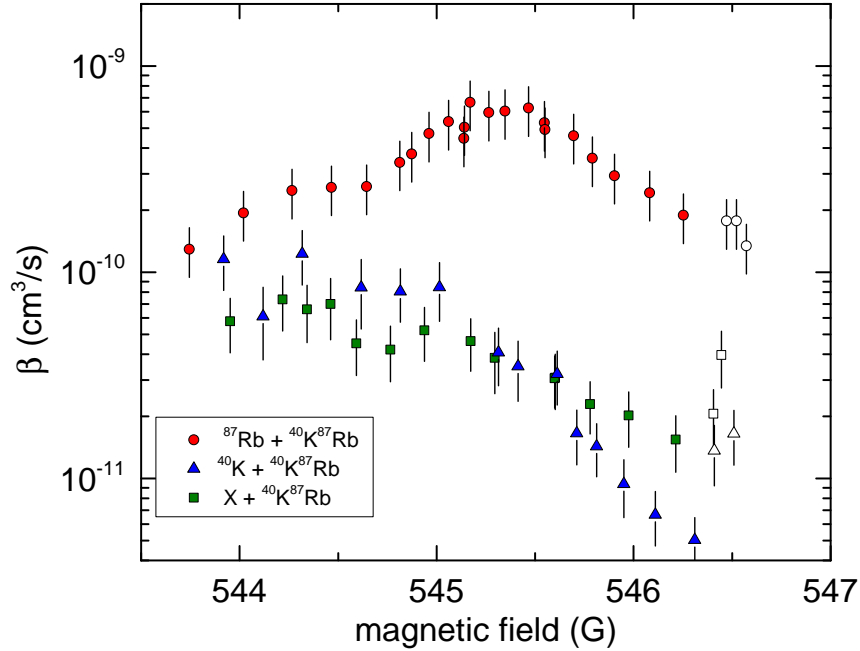
Figure 4.8: Measured atom-molecule collision event-rate coefficient, β, for various collision partners with KRb molecules. The data shown as circles correspond to collisions between molecules and Rb atoms in the $|1,1\rangle$ hyperfine state. The Rb-molecule collision can be influenced by Efimov physics, unlike the resonant K-molecule collisions, shown in triangles. The resonant feature also is not seen in collisions between distinguishable atoms (K atoms in $|9/2, -7/2\rangle$) and molecules, shown as squares. The open circles, squares, and triangles occur at scattering lengths where molecules can additionally dissociate due to their finite temperature.

data points, the temperature of the atoms and molecules are are equal to, or greater than, the molecule binding energy such that spontaneous dissociation is possible. In this figure, there is clearly a resonant feature at 545.3 G in the Rb+molecule relaxation coefficient, which is absent in collisions with distinguishable atoms as well as K atoms. Recall from Section 4.1 that FFX collisions in our system do not exhibit Efimov states. Additionally, collisions with non-resonant distinguishable atoms would not exhibit an Efimov feature, but any effects that are independent of spin-statistics of the atom would become apparent. The fact that this resonance only occurs in resonant Rb+molecule collisions is consistent with this feature being an Efimov resonance.

4.5 Comparison with universal predictions

One remaining question is whether or not the resonant feature we observe in Rb+molecule collisions is an Efimov resonance, albeit one subject to finite-range corrections since the scattering length at which the feature is centered (a = 250 a_0) is only about three times the van der Waals length ($r_{vdW} = 71.9a_0$). Shown in Fig. 4.9 is the same data as in Figs. 4.8 and 4.4, but replotted in terms of the scattering length. The scattering length is determined by the average of those given by the Feshbach resonance parameters of Refs. [86] and [117]; the scattering length error bars in the plot are half the difference between the two scattering lengths. The answer to the question of whether this feature is an Efimov resonance has three possibilities, which we can partially address using the universal formulae for α as well as the relations between a_*, a_-, and a_+.

The first possibility is that the resonant feature in Fig. 4.9a is the second lowest atom-molecule relaxation feature, $a_*^{(2)}$. The Rb-molecule feature is centered at 250 a_0 and if, for the moment, we assume the universal relations are applicable, then from Eqn. (4.1.11) we would expect a peak in three-body recombination at a= $a_-^{(1)} = -490\,a_0$. The three-body recombination spectra using Eqns. (4.2.10), (4.2.9), and (4.2.8) for this result, and the accompanying value $a_+^{(1)} = 44\,a_0$ from Eqn. (4.1.12), are shown as the solid curves in Fig. 4.9b. The feature at a= $a_-^{(1)} = -490\,a_0$ disagrees strongly with what we measure. However, given that $a_+ = 250\,a0 \approx 3.5\,r_{vdW}$, it is unlikely that the universal relations between $|a_-^{(n)}|$ and $a_*^{(n+1)}$ will hold in our case. The other possibilities are that the Rb-molecule resonance is either the $a_*^{(1)}$ resonance (shown as the dashed curves in Fig. 4.9b) or is not an Efimov resonance at all. Given the lack of features in α, these two possibilities cannot be distinguished because, if the Rb-molecule resonance is $a_*^{(1)} = 250\,a_0$, then $a_-^{(1)} \approx -60,000\,a_0$ and $a_+^{(1)} = 5430\,a_0$ [10] , which are both outside of the range of realizable scattering

---

[10] For these two theory curves, the theory prediction for α was modified to truncate the Efimov series at the lowest resonances. We assumed simple a^4 scaling of α for scattering lengths $a \leq |a_-^{(1)} \exp\left(-\frac{\pi}{2s_0}\right)|$ on the negative side and for $a \leq a_+^{(1)} \exp\left(-\frac{\pi}{2s_0}\right)$ on the positive; the prefactor for the a^4 was matched to the universal theory at $a = a_-^{(1)} \exp\left(-\frac{\pi}{2s_0}\right)$ on the negative side and $a = a_+^{(1)} \exp\left(-\frac{\pi}{2s_0}\right)$ on the positive. The matching points at $a = a_-^{(1)} \exp\left(-\frac{\pi}{2s_0}\right)$ and $a = a_+^{(1)} \exp\left(-\frac{\pi}{2s_0}\right)$ were chosen because they are half of a log-period away from their associated extrema where the universal theory is at the opposite extrema and is purely a^4 in nature.

lengths. Thus the nature of this Rb-molecule feature is uncertain due to the lack of corroborating features in the three-body recombination data. However, the three-body recombination data is most consistent with the $a_-^{(1)}$ and $a_+^{(1)}$ resonances occurring at scattering lengths well past what we can realize experimentally. This is the scenario that a recent theory paper predicts[157].

4.6   Three-body parameter and comparison with ^{41}K $-^{87}$Rb

Now we return to the question of universality for the three-body parameter in heteronuclear systems. Recall that the observation that sparked this question involved measurements of Efimov resonance positions from four Feshbach resonances in Cesium. The authors measured that the Efimov resonances on the $a < 0$ (a_-) corresponded to very similar scattering lengths. The average value for the $a < 0$ Efimov resonance positions was found to be $a_- = -9.1(4)\, r_{vdW}$ [57]. Similar observations have been made in ^{6}Li, ^{7}Li and ^{85}Rb [23].

Recent theoretical work supports the notion that for open-channel dominated Feshbach resonances, the locations of $a_-^{(1)}$ resonances are universally determined by r_{vdW}. In Ref. [23] it is argued that a strong quantum reflection of the three-body wavefunction at the point where the van der Waals potential begins to dominate the $1/R^2$ three-body potential (c.f. Eqn. (4.1.1)), sets a boundary condition at a hyperradius $R \approx r_{vdW}$ which in turn sets the location of $a_-^{(1)}$. Similar results are voiced in Ref. [155] where they find that, for model single-channel two-body potentials, the effective three-body potentials (akin to Eqn. (4.1.1)) converge to a single curve as the number of two-body bound states is increased. These effective potentials have the sharp drop-off as in Ref. [23] as well as a strong repulsive barrier at $R \approx 2r_{vdW}$ [11] . As a consequence of this barrier, they find that the location of the first Efimov resonance converges to a value consistent with experimental observations as the number of two-body bound states in their model potentials is increased to roughly 10, which is a reasonable number for atomic potentials [140]. The authors of Ref. [138] extend the approach to a two-channel model in order to address the question of universality in systems where

---

[11] This repulsive barrier restricts the three-body wavefunction from having substantial weight at length scales comparable to the length scale of the non-additive three-body potential [141].

(a)

(b)
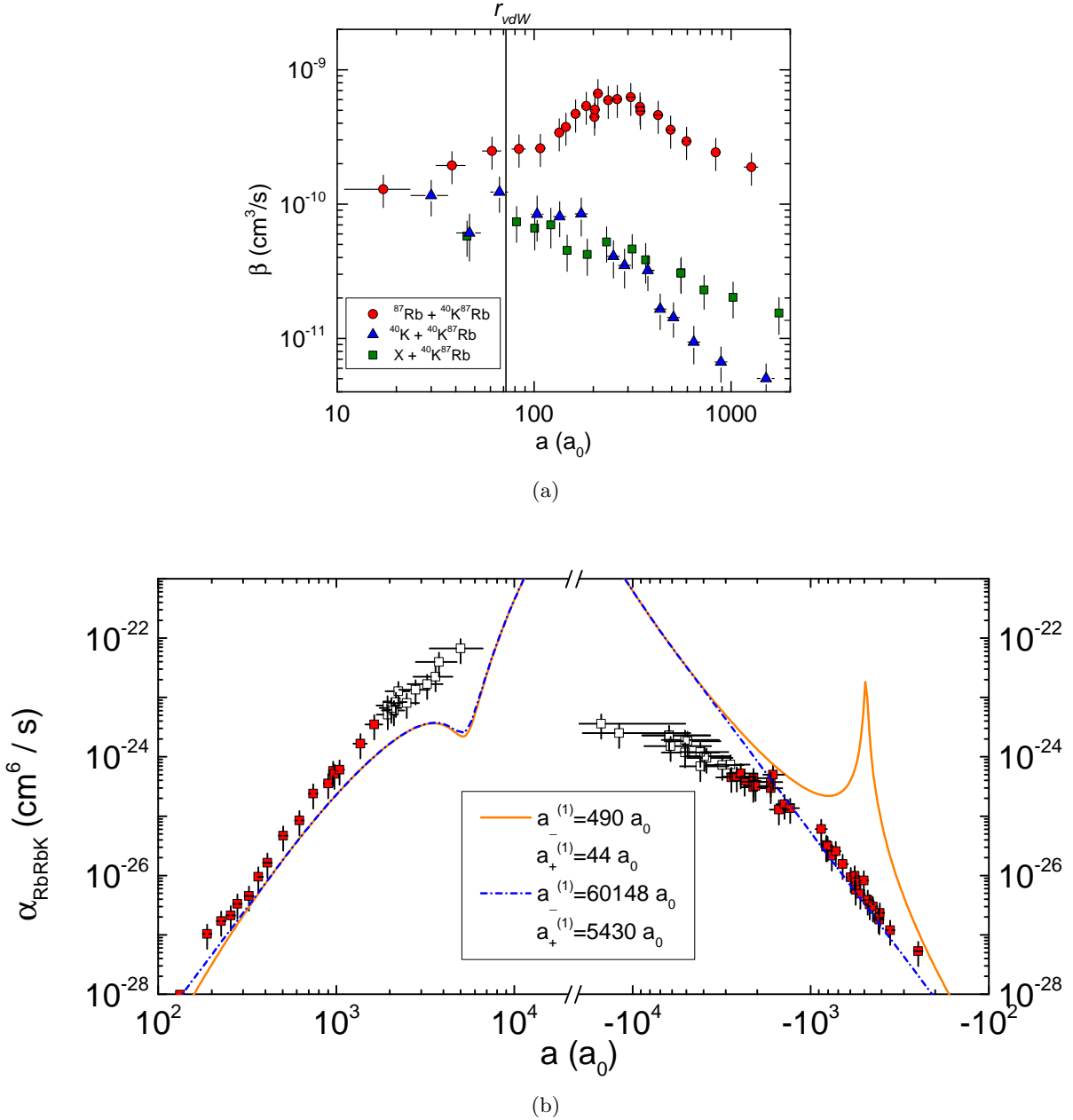
Figure 4.9: Replotting of the data from Figs. 4.4 and 4.8 in terms of scattering length. The scattering length was calculated by averaging the scattering lengths produced by the Feshbach parameters of Refs. [86] and [117].a) Atom-molecule event rate coefficient from Fig. 4.8. The Rb+molecule collisions indicate a resonance centered at 250 a_0. b) Overlaid over the three-body recombination data are predictions of α using the universal relations (Eqns. (4.1.11) and (4.1.12)) to relate a_- and a_+ to a_*. The solid curves assume that the atom-molecule feature in a) is $a_*^{(2)}$ and the dashed curves assume the feature is $a_*^{(1)}$. The data near the d-wave Feshbach resonance have been omitted from the plot.

	$^{40}K\,^{87}Rb\,^{87}Rb$	$^{41}K\,^{87}Rb\,^{87}Rb$	$^{41}K\,^{41}K\,^{87}Rb$
s_0	0.6532 [72]	0.6444 [72]	0.2462[72]
e^{π/s_0}	122.7 [72]	131.0 [72]	348 000 [72]
a_-/a_0	None (for $|a| < 3000a_0$)	-246(14) [7]	$-22\binom{+4}{-6} \times 10^3$[7]
a_*/a_0	250	667(1)[7]	
η_*		0.12(1)[7]	0.017(10) [7]
r_{vdW}/a_0	71.9	72.2	72.2

Table 4.2: Comparison of Efimov resonance parameters between ^{41}K – ^{87}Rb and ^{40}K – ^{87}Rb.

the Feshbach resonance is not necessarily open-channel dominated [12] . They find that the location of $a_-^{(1)}$ asymptotes to a constant value for $s_{res} \gg 1$ whereas in the $s_{res} \ll 1$ limit $a_-^{(1)}$ approaches infinity [13] . All of these treatments consider only collisions between three-identical bosons, however it is likely that the universality in the three-body parameter extends to heteronuclear systems.

The LENS group in Florence published observations of Efimov resonances in ^{41}K – ^{87}Rb, where they used measurements of the atom number after holding at a fixed field for a fixed time [7, 8]. They located a_- features in the ^{41}K – ^{41}K – ^{87}Rb and the ^{87}Rb – ^{87}Rb – ^{41}K loss channels, as well as an Rb+molecule resonance observed via atom loss at fixed hold. The summary of their observations is shown in Table 4.2, as well as the predicted log-periodicity of their Efimov features and the van der Walls length, r_{vdW}, for both ^{41}K – ^{87}Rb and ^{40}K – ^{87}Rb. Note that the FFX collision channel in ^{40}K – ^{87}Rb does not support Efimov states and therefore only the locations of features in ^{87}Rb – ^{87}Rb – ^{40}K and ^{87}Rb – ^{87}Rb – ^{41}K can be compared.

As can be seen in Table 4.2, the van der Waals lengths for the ^{41}K – ^{87}Rb and the ^{40}K – ^{87}Rb are very similar and under the assumption of universality in the three-body parameter, we would

---

[12] Recall from Eqn. (3.2.2) that $s_{res} \gg 1$ denotes open-channel dominated Feshbach resonances and $s_{res} \ll 1$ denotes closed-channel dominated resonances.

[13] For ^{39}K ($s_{res} = 2.1$ [23]), the authors of Ref. [138] predict $a_-^{(1)} \approx -13\,r_{vdW}$, compared to $a_-^{(1)} = -8.27\,r_{vdW}$ for open-channel dominated resonances.
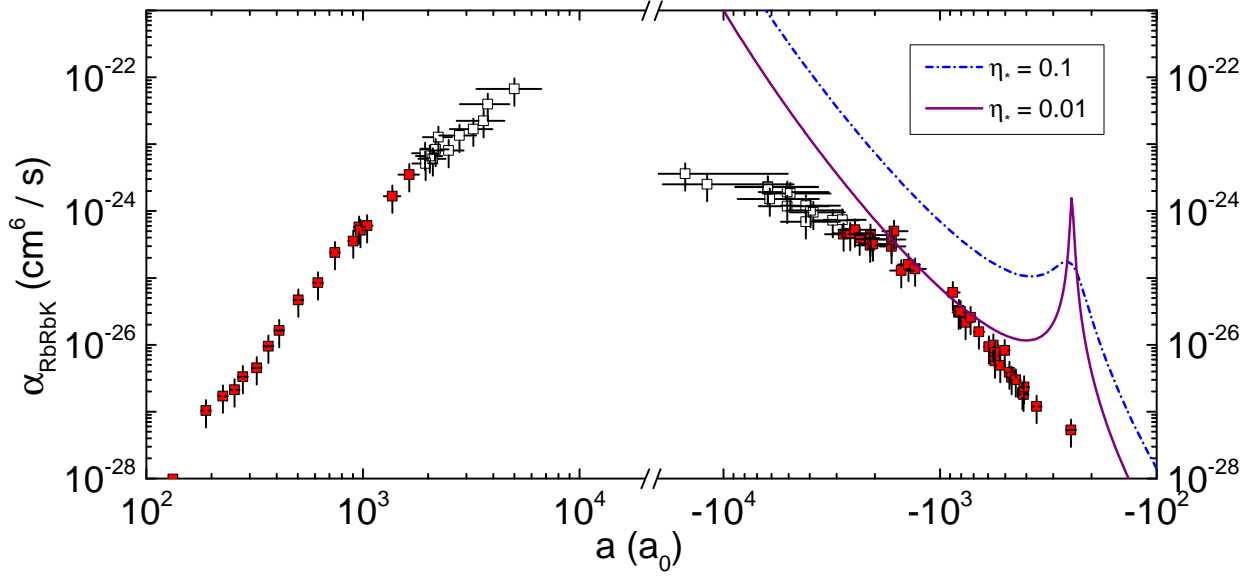
Figure 4.10: Plot of the data from Fig. 4.9b with the universal theory for $\alpha_d^{(-)}$ (Eqn. (4.2.10)) assuming $a_- = -246\,a_0$ as in the ^{87}Rb – ^{87}Rb – ^{41}K reported in Ref. [7].

have expected to see features at nearly the same scattering lengths as in ^{41}K – ^{87}Rb. Perhaps our most surprising result is the lack of an observed a_- feature in our system compared to the feature observed at $a = $ -246 a_0 in ^{41}K – ^{87}Rb; this is in stark contrast to the three-body parameter universality seen in homonuclear systems[14] . The magnitude of this discrepancy is shown in Fig. 4.10, where the theoretical curves from Eqn. (4.2.10) are for $a_- = -246\,a_0$. This begs the question: what is different between our system and LENS' that would explain this discrepancy in observed features? One large difference is in the properties of the two Feshbach resonances. As can be seen in Table 4.3, the Feshbach resonance used by the LENS group is substantially broader than ours in terms of magnetic field, as well as being more clearly open-channel dominated.

The Feshbach resonance we employ is only starting to be open-channel dominated with $s_{res} \approx 2$. In systems with narrow Feshbach resonances (i.e. $s_{res} \ll 1$), the three-body physics is

---

[14] The disagreement between our observed a_* features, while large, is not too alarming. The locations of the atom+molecule resonances are not expected to be universal because of non-universal behavior in the molecule state [138]. Furthermore, in homonuclear systems, the atom+molecule resonances have not agreed with the universal predictions [88, 129, 170].

(a) Scattering length and effective range

(b) Fraction difference in scattering phase due to effective range
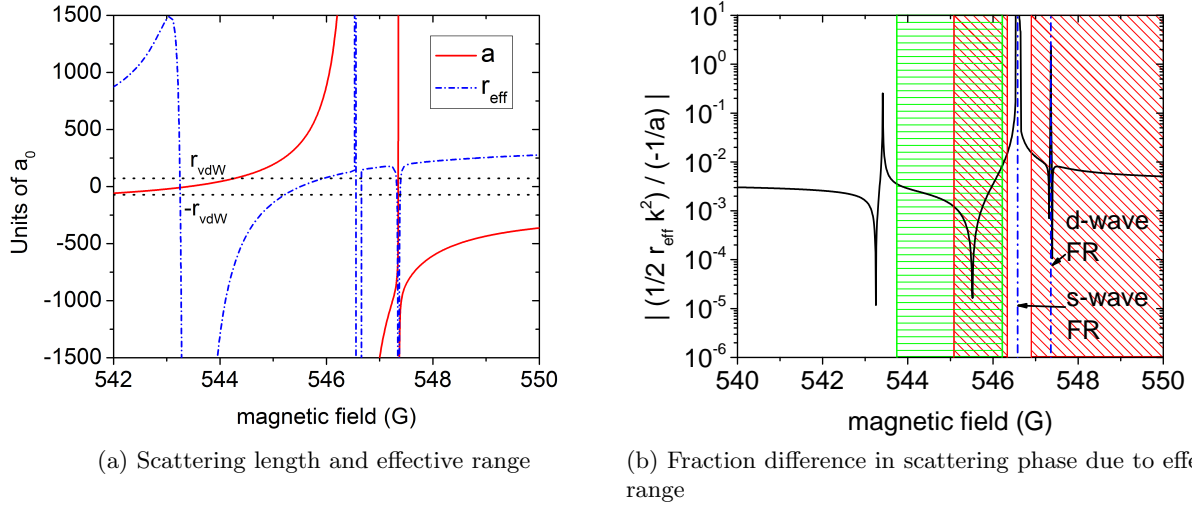
Figure 4.11: a) Quantum Defect calculation of the scattering length and effective range, r_{eff}, for ^{40}K in the $|9/2, -9/2\rangle$ hyperfine state and ^{87}Rb in the $|1, 1\rangle$ hyperfine state courtesy of Brandon Ruzic and John Bohn [136]. The scattering length plot shows both the broad s-wave Feshbach resonance as well as a narrow d-wave Feshbach resonance at 547.35 G. The effective range exhibits divergences at the two zero crossings of the scattering length. The divergence in r_{eff} at the s-wave resonance location is perhaps a numerical artifact. For a length-scale comparison, $\pm r_{vdW} = \pm 71.9 a_0$ is shown as the horizontal dotted lines. b) Ratio of the effective range term $(1/2 \, r_{\text{eff}} \, k^2)$ in the effective range expansion of $k \cot \delta_0$ defined below to the scattering length term $(-1/a)$ at 250 nK.

modified significantly resulting in different scattering-length scaling laws for α [128, 156] because the scattering length is the dominant length scale for only a small region of the resonance. However, a counter example to this concern of the width of our Feshbach resonances are the observed Efimov spectrum in ^{7}Li [64] ($s_{\text{res}} = 0.80$, $r_{vdW} = 32.5 a_0$ [24]). Even though the Feshbach resonance used in Ref. [64] is a borderline closed-channel dominated resonance, they find the first Efimov resonance to occur at $|a_-^{(1)}|/\bar{a} = 8.5$, which is close to what is seen in Cs[12].

Questions of the width of the Feshbach resonance boil down to considerations of the effective range. Recall that the effective range expansion of the two-body s-wave scattering phase, δ_0, is given by $k \, \cot(\delta_0(k)) = -1/a + \frac{1}{2} r_{\text{eff}} k^2$ (Eqn. (3.1.3)), where r_{eff} is the effective range. The effective range is a function of scattering length [24] and diverges at a = 0 [24, 64]. In order to settle questions about the width of our Feshbach resonance, we need to examine the effective range.

	$^{40}K\,^{87}Rb$	$^{41}K\,^{87}Rb$
$B_0(G)$	546.71(1) [117]	38.40(3) [159]
$\Delta(G)$	-3.34(5) [117]	37 [140]
$\delta\mu(\mu_B)$	2.38 [174]	1.65 [24]
$a_{bg}(a_0)$	-185(7)[54]	284 [140]
s_{res}	2.15	25.8 [24]

Table 4.3: Comparing the Feshbach resonances between ^{40}K – ^{87}Rb and ^{41}K – ^{87}Rb

Brandon Ruzic and John Bohn were kind enough to calculate the locations and widths of Feshbach resonances in our system using a Quantum Defect theory and provided a calculation of the effective range as well. The results of Brandon's calculations are shown in Fig. 4.11a. The α data in this chapter corresponding to scattering lengths below thermal saturation, spans the magnetic-field ranges 545.08 G < B < 546.33 G and 546.90 G < B < 556.10 G. Generally we want to work in the regime where the scattering length is the dominant length scale and the effective range is not substantially larger than r_{vdW} [15] (e.g. $r_{eff} < 10\,r_{vdW}$).

To determine how significant the effective range is at a given magnetic field is to consider how the effective range changes the s-wave phase shift, δ_0. By examining the significance of the effective range term to the s-wave phase, we are asking if the scattered wavefunction of the two atoms is affected by the effective range term. Recall from scattering theory that the scattered wavefunction amplitude for central forces can be expressed by a partial wave expansion

$$f(k,\theta) = \sum_{l=0}^{\infty} f_l(k)P_l(\cos\theta)$$

where $P_l(\cos\theta)$ are Legendre polynomials. The partial wave amplitudes relate to the scattering

---

[15] For bosons near a narrow Feshbach resonance, a large effective range is predicted to modify the equations for the Efimov log-periodic scaling factor [156].

phases by [20]

$$f_l(k) = \frac{2l+1}{2\imath k}\left[\exp 2\imath\delta_l(k) - 1\right] = \frac{2l+1}{k\cot\delta_l - \imath k}$$

where δ_l is the phase shift for the l-th partial wave. For the temperatures that we operate at(100 nK-1 μK) we only need to concern ourselves with s-wave scattering[16] . Recall from Eqn. (3.1.3) that the first two terms in the effective range expansion of the s-wave scattering phase shift is

$$k\,\cot(\delta_0(k)) \;=\; -1/a + \frac{1}{2}\mathrm{r}_{\mathrm{eff}}\,k^2.$$

We can estimate the wave number, k, from the average speed of two colliding thermal atoms(see Ref. [60]); the wave number is then $k = \sqrt{\frac{8\mu k_B T}{\pi\hbar^2}}$, where μ is the two-body reduced mass. We can now indicate regions where the effective range is an issue by calculating the ratio $\left|\frac{1/2\mathrm{r}_{\mathrm{eff}}k^2}{-1/a}\right|$. The results of this ratio, using the results in Fig. 4.11a and assuming T = 250 nK, are shown in Fig. 4.11b. The region in magnetic field covered with the α data (below thermal saturation) is indicated as the diagonally hashed regions and the horizontally hashed region indicates the magnetic field span covered in the β data. As can be seen the effective range amounts to a < 1.5% correction to the value of $k\cot\delta_0$ over the hashed regions, excluding the region near the d-wave Feshbach resonance. The scattering length over the range excluding the d-wave Feshbach resonance is the dominant length scale. Therefore, the fact that our resonance is not as clearly open-channel dominated as the resonance in ^{41}K $-$ ^{87}Rb, is unlikely to be an issue significant enough to explain the fact that we do not observe Efimov features at the locations seen by LENS.

---

[16] The p-wave threshold for ^{40}K-^{87}Rb is roughly 110 μK [60] below which the p-wave scattering cross section falls off as T^2 as per the Wigner threshold law.

Chapter 5

The "Fabrergé egg" Ioffe-Pritchard trap

Near the end of August 2010, the south Fast B coil developed a break in its insulation inside of the existing Ioffe-Pritchard (IP) trap. The Fast B is a capacitor driven system (C = 6.8 mF) that is initially charged to ≈150 V. Due to the break in the coil's insulation, a violent arc within the IP trap would result discharging ≈1 Coulomb into the IP trap's copper cooling forms. We were able to fix the issue after partially disassembling the IP trap and coating the areas of obliterated insulation with an electrically insulating enamel. This incident, combined with the previous failures of two out the four rf antennas (we need two antennas minimum), which are epoxied inside of the IP trap, prompted the design of a replacement magnetic trap.

In designing the new magnetic trap, we desired to make a few improvements over the existing IP trap. The existing IP trap coils are made from solid core wire, which is wrapped around copper heatsinks. Cooling water flows through these heat sinks to carry away the heat generated by the trap. Although slots were cut through the copper heat sinks to suppress eddy currents, the contribution of eddy currents to magnetic field at the atoms is not insignificant. While we can correct the total magnetic field for these eddy currents (c.f. the eddy current correction section of Michele Olsen's thesis [116]), it is desirable to eschew the copper cooling forms and instead build the coils out of hollow-core copper tubing. The cooling water then flows directly through the coils and eliminates the need for extra copper near the atoms. Another design goal was to improve the optical access for improved imaging as well as future lattice experiments. Lastly, we also want to use the trap's bias coils to provide the large field necessary for reaching our Feshbach resonances
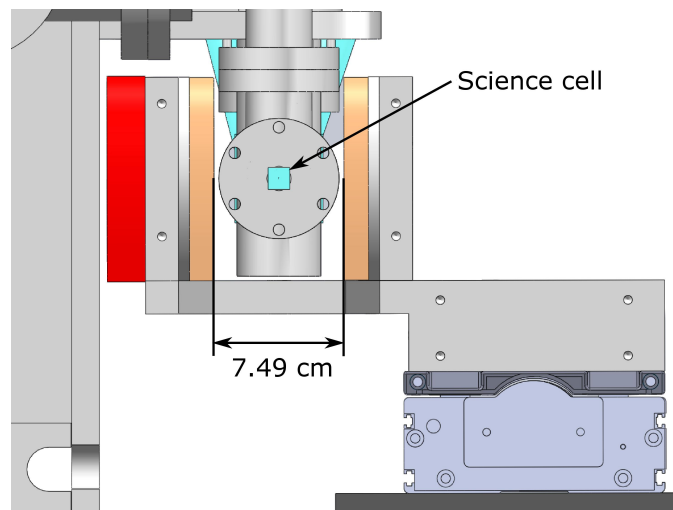
Figure 5.1: View of the 'Science cell' end of the vacuum chamber with the IP trap removed. The Science cell (small cyan square) is flanked by the Quadrupole trap coils (orange rectangles) which restricts the size of the new IP trap.

(and beyond to 800 G) and therefore we require this coil pair to have a small amount of field curvature.

Unfortunately, there are fairly strict space constraints on the size of the IP trap due to the orientation of Quadrupole trap coils on the moving cart system as shown in Fig. 5.1. Due to these constraints we cannot simply borrow the hollow tubing based designs from the other labs in JILA as they require more space in the horizontal direction than the Quadrupole coils will allow. The need to miniaturize the design will influence the coil geometry, as will be discussed in Sec. 5.1. The space constraints will also necessitate building the trap coils out of narrower tubing than previous designs. This raises the concern that the cooling water flow through the coils will be insufficient to remove the heat generated by the trap. Addressing this concern is the subject of Sec. 5.2. This chapter concludes with a summary of the magnetic trap specifications. However, as of the writing of this chapter, the trap has not yet been installed on the apparatus.
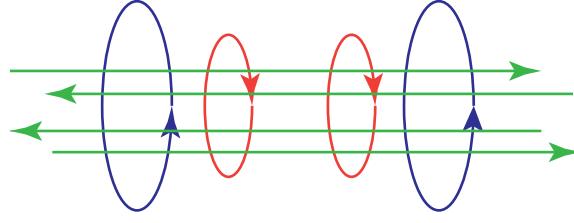
Figure 5.2: Simplified diagram of a Ioffe-Pritchard trap where the arrows indicate the direction of current flow through each coil. Axial curvature is provided largely by the pinch coils (red coils) and the bias coils (blue coils) serve to largely cancel the offset field produced by the pinch coils. Radial confinement is provided by the radial quadrupolar field produced by the Ioffe bars (horiz. arrows).

5.1   Magnetic trap potential and design considerations

Rb and K, as with the other alkalis, possess magnetically sensitive hyperfine states in their ground electronic states. This magnetic sensitivity occurs as a consequence of the coupling between the magnetic moment μ of the atom, which is caused by the angular momentum of the alkali atom's unpaired electron and nuclear spin, to a magnetic field via the Zeeman effect. The Zeeman effect couples eigenstates of the atom to an applied magnetic field B with an interaction energy of the form $U = -\vec{\mu} \cdot \vec{B} = m_F\, g_F\, \mu_B |\vec{B}(\vec{r})|$ [20], where m_F is the projection of the total atomic angular momentum along the magnetic field, g_F is the Landé g-factor, and μ_B is the Bohr magneton, which determine the strength of the magnetic moment, μ. As shown in Refs. [166, 85] the magnitude of the magnetic field in free space cannot have a maximum due to Gauss' law, but local minima are possible. Therefore we can trap states for which $g_F\, m_F > 0$ (so-called 'low-field seeking' states) in a local minimum [149, 69, 93, 108]. For ^{40}K the Landé g-factors in the ground electronic states are $g_{7/2} = -2/9$ and $g_{9/2} = 2/9$, and the states $|F, m_F\rangle = |7/2, -7/2\rangle$, $|7/2, -5/2\rangle$, $|7/2, -3/2\rangle$, $|7/2, -1/2\rangle$, $|9/2, 9/2\rangle$, $|9/2, 7/2\rangle$, $|9/2, 5/2\rangle$, $|9/2, 3/2\rangle$, and $|9/2, 1/2\rangle$ can all potentially be trapped. For ^{87}Rb the g-factors are $g_2 = 1/2$ and $g_1 = -1/2$ and the list low-field seeking states is significantly shorter: $|2, 2\rangle$, $|2, 1\rangle$, and $|1, -1\rangle$ can be trapped.

The magnetic trap style that we chose to implement is the Ioffe-Pritchard trap [80, 130]

because of its ease of construction and modelling. The trap is formed by fields from three sets of coils, as shown in Fig. 5.2. The *pinch coils* (small red coils) provide an axial curvature as well as an offset field. This offset field is largely canceled by the *bias coils* (large blue coils) whose current flows the opposite orientation as the pinch coils. Lastly, radial confinement is provided by the radial quadrupolar field produced by the *Ioffe bars* (green wires). The magnetic field produced by this configuration at the center of the trap is approximately [130]

$$\vec{B}(x, y, z) = \left(\beta\, x - \frac{1}{2}\gamma\, z\, x \right)\, \hat{x} - \left(\beta\, y + \frac{1}{2}\gamma\, z\, y \right)\, \hat{y} + \left(B_0 + \frac{1}{2}\gamma \left(z^2 - \frac{x^2 + y^2}{2} \right) \right)\, \hat{z} \qquad (5.1.1)$$

where β the radial field gradient of the Ioffe bars, γ is the total axial field curvature from the pinch and bias coils, and B_0 is the sum the pinch and bias offset fields. If we now approximate the potential at the center of the trap as harmonic, the trap frequency in the i-th direction can be calculated from

$$m\omega_i^2 = \mu \frac{\partial |\vec{B}|}{\partial x_i}\bigg|_{x=y=z=0} \qquad (5.1.2)$$

where m is the atomic mass and μ the atomic magnetic moment. The trap frequencies from Eqn. (5.1.1) are given by

$$\omega_x = \sqrt{\frac{\mu}{m} \left(\frac{\beta^2}{B_0} - \frac{1}{2}\gamma \right)} \qquad (5.1.3)$$

$$\omega_y = \sqrt{\frac{\mu}{m} \left(\frac{\beta^2}{B_0} - \frac{1}{2}\gamma \right)} \qquad (5.1.4)$$

$$\omega_z = \sqrt{\frac{\mu}{m}\gamma}. \qquad (5.1.5)$$

Since evaporation of atoms is aided by having large trap frequencies[1] , some design principles arise from Eqn. (5.1.3). In addition to desiring large field gradients and curvatures, we also wish to have the lowest offset field possible. However, the offset field cannot be set to zero because the magnetic moment of the atom will not be able to adiabatically follow the magnetic field direction as it travels

---

[1] The elastic collision rate between K and Rb is proportional to $\bar{\omega}^3 N/T$ [60] where $\bar{\omega} = \sqrt{\omega_x\, \omega_y\, \omega_z}$. This collision rate sets the time scale by which the system rethermalizes and thereby repopulates the high-momentum tail of the distribution which had just been truncated by the rf-evaporation knife. By having a larger trap frequency, the evaporation is able to proceed faster and reduce the loss due to background collisions.

through the center of the trap. In that case, the atom will undergo Majorana spin flips resulting in loss of atoms from the trap [126]. Additionally, the campus AM radio station broadcasts at 1.19 MHz which potentially could drive spin flips in $|9/2, 9/2\rangle$ K at 3.8 G and so we designed the trap with an offset field of 4 G in mind.

5.1.1 Modeling the magnetic field from the coils

To design the trap we need to model the magnetic field from the coils, which are in reality multiple layer helices made from hollow tubing (square outer cross-section and round inner cross-section) with a non-zero thickness. For the bias and pinch coils, we model each turn as a closed loop of current with a separation between loops equal to the tube thickness. For a coil of radius R centered on the axial location $z = z_0$, the magnetic field components from the coil are [11]

$$B_z(r, z, z_0) = \frac{0.2}{\sqrt{(R+r)^2 + (z-z_0)^2}} \left(K(k^2) + \frac{R^2 - r^2 - (z-z_0)^2}{(R-r)^2 + (z-z_0)^2} E(k^2) \right) \tag{5.1.6}$$

$$B_r(r, z, z_0) = \frac{0.2}{r} \frac{z - z_0}{\sqrt{(R+r)^2 + (z-z_0)^2}} \left(-K(k^2) + \frac{R^2 + r^2 + (z-z_0)^2}{(R-r)^2 + (z-z_0)^2} E(k^2) \right) \tag{5.1.7}$$

where B_z and B_r are the axial and radial magnetic-field components, respectively, in G/A, with all spatial dimensions in cm. The functions $K(k^2)$ and $E(k^2)$ are complete elliptic integrals of the first and second kind, respectively, where the argument is defined as $k^2 = \frac{4Rr}{(R+r)^2 + (z-A)^2}$. The bias and pinch coils are then modeled by summing up the fields of individual loops of the appropriate radius and axial location. To simulate the real coils, which are multiple layered helices, the loops are tilted by an angle $\theta = (-1)^{n+1} \arcsin\left(\frac{t}{2R}\right)$ for a turn in the n-th layer of radius R for tubing of thickness t (see Fig. 5.3b). The winding tilt creates a non-axial field component which is canceled at the trap center by winding each bias and pinch coil in the coil pair as a mirror image of the other where the mirror plane is parallel to the plane of the ideal (i.e. winding tilt free) coil ^{2} .

---

^{2} The non-axial field component for a coil pair separated by a distance d, is roughly $B_z(r, z, d/2) \sin(\theta) + B_z(r, z, -d/2) \sin(-\theta) = \sin(\theta)(B_z(r, z, d/2) - B_z(r, z, -d/2)) = \frac{t}{2R}(B_z(r, z, d/2) - B_z(r, z, -d/2))$. Similarly the axial component is reduced to $B_z(r, z, d/2) \cos(\theta) + B_z(r, z, -d/2) \cos(-\theta) = \cos(\theta)(B_z(r, z, d/2) + B_z(r, z, -d/2)) = \sqrt{1 - \left(\frac{t}{2R}\right)^2}(B_z(r, z, d/2) - B_z(r, z, -d/2))$. The ratio $\frac{t}{2R} = 0.04$ for the innermost layer of the bias coils and
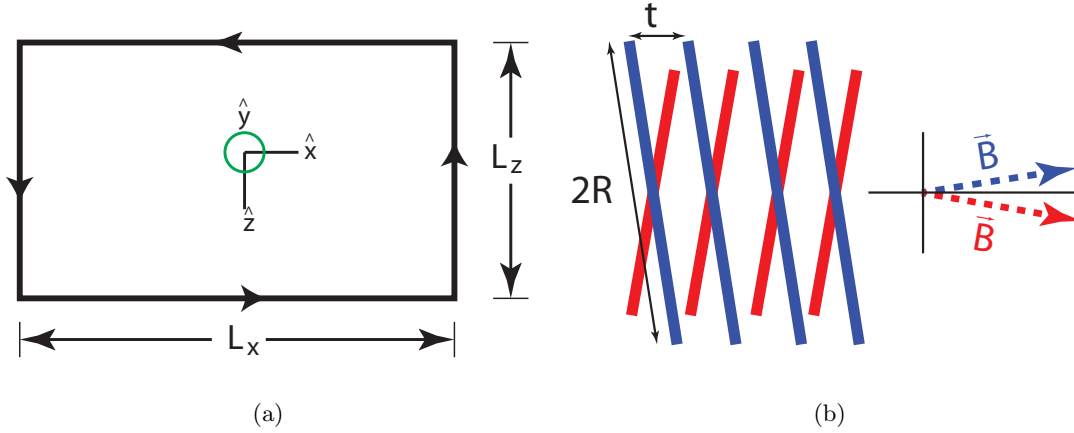
Figure 5.3: a) Diagram for the rectangular coil used to model the Ioffe bars where the unit vector $\hat{y}$ points out of the page and the current flows in the direction indicated by the arrows. b) Diagram of the winding tilt model showing the individual loops edge-on (solid lines) for two layers of windings. As a consequence of the tilt, the magnetic field from each layer acquires a vertical component which does not completely cancel when the coil is considered as a whole.

The Ioffe bars are modeled as sets individual rectangular loops of current to incorporate the effect of the ends of the Ioffe bars. The magnetic field from each rectangular loop is the sum of the magnetic fields from four finite-length wires, whose magnetic field can be calculated from the Biot-Savart law. The geometry of this coil is shown in Fig. 5.3a where the $\hat{y}$ direction points out of the page. To simplify the equations, let's introduce the function $f(A, B, C) = \dfrac{A}{\sqrt{A^2 + 4(y - y_c)^2 + B^2}}$. For a rectangular coil centered at $y = y_c$ of dimensions L_x and L_z, the magnetic field components

---

$\frac{t}{2R} = 0.08$ for the innermost layer of the pinch coils; for the bias coils $\sqrt{1 - \left(\frac{t}{2R}\right)^2} \approx 0.999$ and for the pinch coils $\sqrt{1 - \left(\frac{t}{2R}\right)^2} \approx 0.997$, which indicates that the winding tilt effect is not a large concern for our coils.

	quasi-Helmholtz (d≪2R)	Helmholtz (d=R)
$\frac{2\pi}{\mu_0 I} B(z=0)$	$\frac{2}{R} - \frac{3d^2}{4R^3} + O\left(R^{-5}\right)$	$\frac{16}{5\sqrt{5}\,R}$
$\frac{2\pi}{\mu_0 I} \left.\frac{\partial^2 B}{\partial z^2}\right|_{z=0}$	$-\frac{6}{R^3} + \frac{45d^2}{4R^5} + O\left(R^{-7}\right)$	0
$\frac{2\pi}{\mu_0 I} \left.\frac{\partial^4 B}{\partial z^4}\right|_{z=0}$	$\frac{90}{R^5} - \frac{1575d^2}{4R^7} + O\left(R^{-9}\right)$	$-\frac{55296}{625\sqrt{5}\,R^5}$

Table 5.1: Derivatives of the magnetic field on axis at the center in between a coil pair separated by a distance d.

(in SI units) are

$$B_x = \frac{\mu_0 I}{4\pi}(y - y_c)\left[-\frac{f(L_z - 2z, L_x - 2x) + f(L_z + 2z, L_x - 2x)}{(-L_x/2 + x)^2 + (y - y_c)^2}\right. \tag{5.1.8}$$
$$\left. + \frac{f(L_z - 2z, L_x + 2x) + f(L_z + 2z, L_x + 2x)}{(L_x/2 + x)^2 + (y - y_c)^2}\right]$$

$$B_y = \frac{\mu_0 I}{4\pi}\sum_{n=1}^{2}\left\{(-1)^{n-1}\left[\frac{((-1)^n\frac{L_z}{2} + z)(f(L_x - 2x, (-1)^n L_z - 2z) + f(L_x + 2x, (-1)^n L_z - 2z))}{(y - y_c)^2 + ((-1)^n L_z/2 + z)^2}\right.\right. \tag{5.1.9}$$

$$\left.\left. + \frac{((-1)^n\frac{L_x}{2} + x)(f(L_z - 2z, (-1)^n L_x + 2x) + f(L_z + 2z, (-1)^n L_x + 2x))}{((-1)^n L_x/2 + x)^2 + (y - y_c)^2}\right]\right\}$$

$$B_z = \frac{\mu_0 I}{4\pi}(y - y_c)\left[-\frac{f(L_x - 2x, L_x - 2z) + f(L_x + 2x, L_z - 2z)}{(y - y_c)^2 + (-L_z/2 + z)^2}\right. \tag{5.1.10}$$
$$\left. + \frac{f(L_x - 2x, L_z + 2z) + f(L_x + 2x, L_z + 2z)}{(y - y_c)^2 + (L_z/2 + z)^2}\right]$$

where I is the current flowing in the orientation show in Fig. 5.3a. With Eqns. (5.1.6) and(5.1.8-5.1.10) the full trap can now be designed.

5.1.2   Design principles

Design principles can be found by first modeling the coils with simpler components [3] . First let's consider the bias and pinch coils, which we treat each as a simple loop of current. The magnetic

---

[3] Ref. [110] is great read for when you are designing a magnetic coil, but be wary of the formulae for cooling fluid flow as they only apply for straight tubes. The fluid flow through helical tubes is substantially reduced compared to straight tubes.

field on axis with a simple loop of current is, in SI units,

$$\vec{B} = \frac{\mu_0 I}{2\pi} \frac{R^2}{(z^2 + R^2)^{3/2}} \hat{z} \qquad (5.1.11)$$

where μ_0 is the vacuum permeability, z the axial distance from the coil, and R the radius of the loop. The bias and pinch coils are constructed from coil pairs whose current flows in the same orientation. Shown in Table 5.1 are the even-order derivatives for a coil pair separated by a distance d with the z axis centered at z=0 in between the pair. An alternative way to examine this problem is to define a new variable, $\eta = d/R$, which will serve to characterize the geometry of the coil pair. The magnitude of the magnetic field for the coil pair, and its even partial derivatives, at z=0 becomes

$$B(z = 0) = \frac{\mu_0 I}{2\pi} \frac{16}{(4 + \eta^2)^{3/2} R} \qquad (5.1.12)$$

$$\left. \frac{\partial^2 B}{\partial z^2} \right|_{z=0} = \frac{\mu_0 I}{2\pi} \frac{768(\eta^2 - 1)}{(4 + \eta^2)^{7/2} R^3} \qquad (5.1.13)$$

$$\left. \frac{\partial^4 B}{\partial z^4} \right|_{z=0} = \frac{\mu_0 I}{2\pi} \frac{92160(\eta^4 - 6\eta^2 + 2)}{(4 + \eta^2)^{11/2} R^5} \qquad (5.1.14)$$

which allows for separate analysis of the scaling of the magnetic field on the system size, characterized by R, and the system geometry, characterized by η. For a fixed value of η and current, the magnetic field scales as $1/R$ and the axial field curvature (Eqn. 5.1.13) scales as $1/R^3$. A special case is the Helmholtz configuration ($\eta = 1$) for which the field curvature vanishes. The higher-order even derivatives of the magnetic field do not vanish at $\eta = 1$, and so there is a finite range over which the field is flat to within some fraction of the central field value (this range scales as R). Ideally the bias coils would have the Helmholtz configuration, but since the coils are made from several layers of turns, this is not possible. Therefore, to reduce the field curvature contribution from the turns which are not in the Helmholtz configuration, the bias coils should have a large radius and the separation should be adjusted to minimize the field curvature. From the pinch coils we desire a large field curvature, and so they should have a radius smaller than the bias coils and $\eta > 1$ so that the field curvature is positive.

Scaling laws can also be derived for the Ioffe bars from the magnetic field from an infinite

	Bias	Pinch	Ioffe bars	Fast B
turns / layer	4	4	2	2
number of layers	4	4	1	2
inside diameter (cm)	7.26	3.66	1.4, 4.66	3.68
outside diameter (cm)	10.02	6.42	2.76, 6.02	4.28
B_0 (G/A)	3.32	3.48		1.65
β (G/cm/A)			1.00	
γ (G/cm^2/A)		1.03		0.11

Table 5.2: Calculated magnet coil properties

wire. The magnetic field at a radius R from the wire with a current I is

$$\vec{B} = \frac{\mu_0 I}{2\pi r}\hat{\phi} \tag{5.1.15}$$

where field points in the azimuthal direction, $\hat{\phi}$. As shown in Fig. 5.2, the wires for the Ioffe bars are arranged on a the vertices of a square with the current flowing in the same direction for wires on opposite corners of the square. If we assume that adjacent wires are separated by a distance, d, then the magnetic-field gradient at the center of the wires scales as $1/d^2$. Although this scaling is not as strong as the scaling of the pinch coil curvature, given that the radial trap frequencies depend roughly linearly on the Ioffe bar gradient and axial trap frequency depends on the square root of the curvature, it is advantageous to have the Ioffe bars fit within the pinch coils.

The best configuration we came up with for the coils given our space constraints is the one shown in Fig. 5.4d with the bias and pinch oriented colinear with the Quadrupole trap coils in Fig. 5.1 and the Ioffe bars fitting within the radial coils[4] . Cross-sections of the calculated magnetic field are shown in Fig. 5.4 for the coordinate system shown in Fig. 5.4d using Eqn. 5.1.6 to model magnetic-field from the bias and pinch coils and Eqns. (5.1.8-5.1.10) to model the field from the

---

[4] Other configurations with the pinch coils within the Ioffe bars, or with the orientation of the bias and pinch perpendicular to the Quadrupole trap, were also considered, but when configured to produce the appropriate field strengths, gradients, and curvatures, the traps simply did not fit within our space constraints.
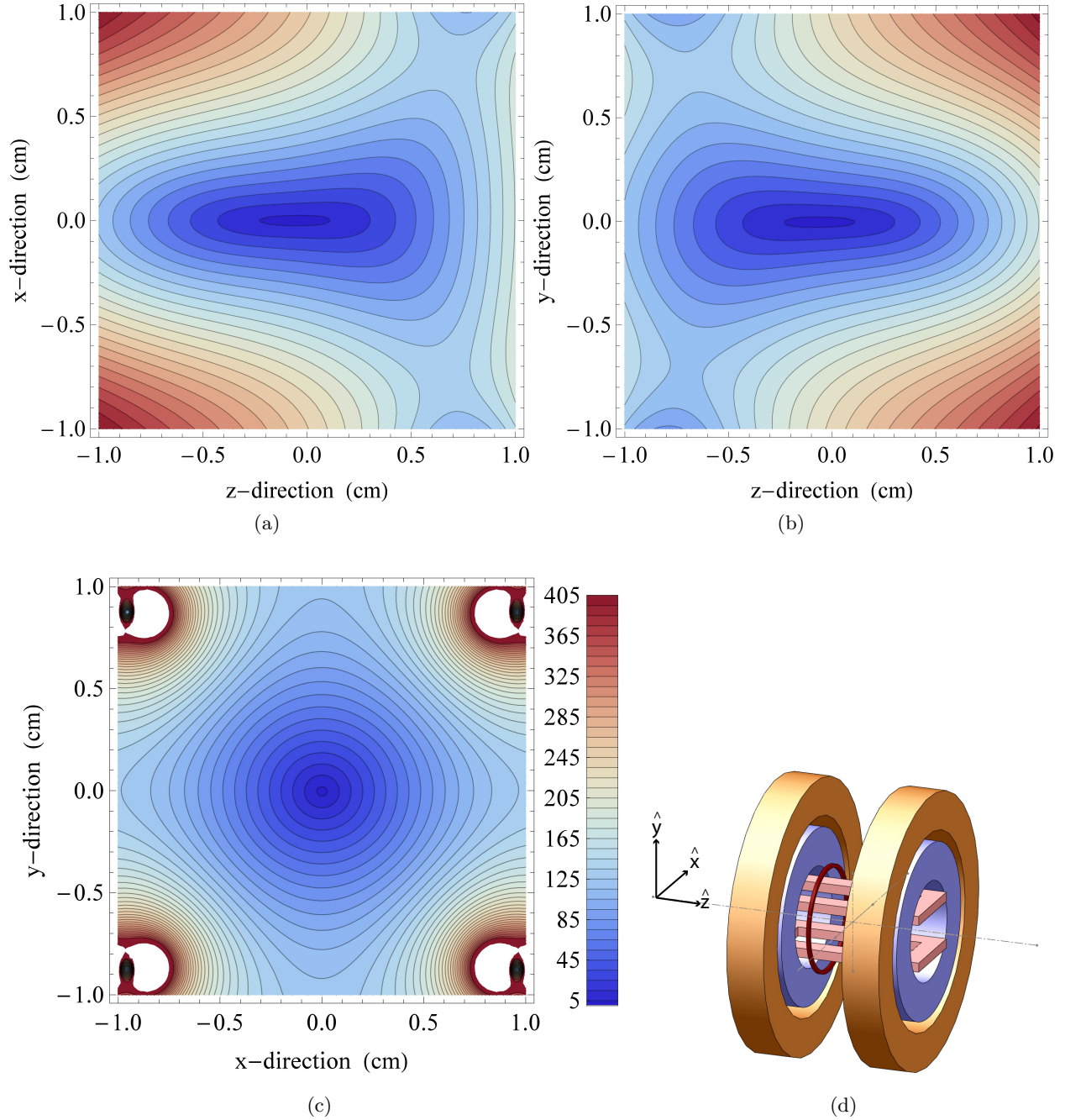
Figure 5.4: a) - c) Cross-sections of the calculated magnetic field magnitude for the operating currens $I_{bias} = 193.75A$, $I_{pinch} = 186A$, and $I_{Ioffe} = 186A$. The field from the bias and pinch coils we calculated from Eqn. 5.1.6 and the field from the Ioffe bars are calculated from Eqns. (5.1.8-5.1.10), which includes the contribution from the ends of the Ioffe bars. The scale for the magnetic field in G is shown in c). d) A simplified diagram of the coils showing the coordinate system. In this diagram the bias coils are shown as the gold rings, the pinch coils are the lavender rings, the Fast B coils are red rings, and the Ioffe bars are the salmon square rings.

Ioffe bars (including the contribution from the ends of the Ioffe bars). As can be seen from Figs. 5.4a and 5.4b, the minimum of the magnetic field is shifted by 0.6 mm in the z-direction, which is small compared to the 1 cm x 1 cm interior dimensions of the science cell. This shift is due to the field gradients produced by the ends of the Ioffe bars as well as the coil leads and can be corrected by either shifting the Quadrupole trap potential over before loading into the IP trap, or by applying a modest gradient of 10 G/cm in the z-direction.

The details of the coils are listed in Table 5.2. In order to allow for the coil leads to exit the trap as a pair, and thus reduce the gradient produced by the leads, the bias and pinch were designed with an even number of layers, and likewise Ioffe bars were designed for an even number of turns. In designing the trap, it became apparent that we would need to use smaller tubing than has been used previously in our labs, so we would need to think carefully about what size tubing to use.

5.2   Water cooling concerns

In order to miniaturize the design of the coils, the channels through which cooling water flows must also be reduced compared to previous designs [173]. This raises the immediate concern that restricting the water to flow through narrower pipes will result in the coils overheating. To assuage these concerns before purchasing the tubing, we first predicted the water flow rate through a helical coil for a given pressure drop.

While a more complete description of fluid flow requires numerically solving the Navier-Stokes equation, in this case it is sufficient to rely on simpler phenomenological equations. As fluid flows through a tube, it suffers frictional loss of energy due to roughness of the tube walls, sharp obstructions to flow, tight bends, etc. The Darcy-Weisbach equation describes the pressure loss as a fluid flows through a pipe. The pressure loss is [81] [5]

$$\Delta P = f \frac{L}{d} \frac{1}{2} \rho_w \, v^2 \tag{5.2.1}$$

---

[5] In the notation of Ref. [81], $\Delta P = \rho_w g h$.
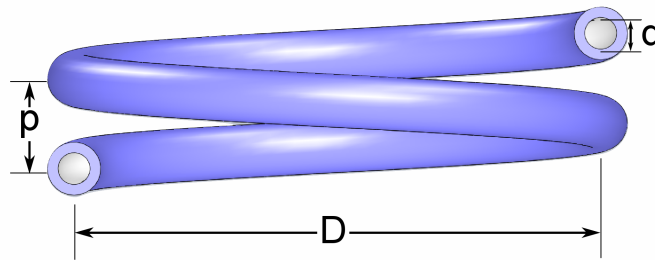
Figure 5.5: Definition of the dimensions of a helix with pitch p, coil diameter D, and inner wetted diameter d.

for a fluid of density ρ_w, mean speed v, in a tube of length L, and inner diameter d. The Darcy friction factor f is a dimensionless factor that depends on the characteristics of the fluid flow (e.g. whether the flow is turbulent or laminar) as well as the pipe roughness.

The degree of turbulence in a given fluid flow is encapsulated in a single parameter, the Reynolds number, Re. The Reynolds number is related to the fluid's kinematic viscosity ν (in units of m^2/s), mean speed, and tube diameter d, by

$$Re = \frac{v\,d}{\nu} \tag{5.2.2}$$

and is proportional to the ratio of the drag force to the viscous force of the fluid. In a sense, the Reynolds number sets the minimum size of eddies possible in the fluid. Large values of Re correspond to turbulent flows which support small eddies in the flow. Conversely, low values of Re indicate smooth laminar flow.

The pressure loss when flowing through a helical tube can be significantly different from the flow through straight pipes. Although helical pipes have been used as heat exchangers for some time, the problem of understanding the flow and pressure drop is still an active area of research [39, 1]. The author of Ref. [1] measured the pressure drop and flow rates through a large set of helical tubes with different pitches p, coil diameters D, and inner diameters d (cf. Fig. 5.5). From the pressure drop data, the author models the pressure drop with an equation akin to the

Darcy-Weisbach equation:

$$\Delta P_{Ali} = 2\,\alpha Re^{-\beta}\,G_{rhc}^{-1}\,\rho_w\,v^2 \tag{5.2.3}$$

where the quantity G_{rhc} is the geometrical group that characterizes fluid flow through a regular helix such that all the pressure drop data from the disparate group of helices falls on the same curve. The volumetric flow rate, Q, in cm^3/s is then

$$Q = \frac{\pi d^2}{4}v = \frac{\pi d^2}{4}\sqrt{\frac{\Delta P_{Ali}\,G_{rhc}}{2\,\alpha Re^{-\beta}\,\rho_w}}. \tag{5.2.4}$$

The author found the best fit for G_{rhc} is

$$G_{rhc} = d^{0.85} D_{eq}^{0.15}/L_c \tag{5.2.5}$$

where the equivalent diameter $D_{eq} = \sqrt{p^2 + \pi D^2}/\pi$ and L_c is the linear length of the coiled section. Upon fitting separate sections of the curve that appear to have constant values of α and β, the author of Ref. [1] finds the following piecewise definition:

$$\alpha Re^{-\beta} = \begin{cases} 21.88\,Re^{-0.9}, & Re < 500, \text{ low laminar} & (5.2.6) \\[2mm] 5.25\,Re^{-2/3}, & 500< Re <6300, \text{ laminar} & (5.2.7) \\[2mm] 0.56\,Re^{-2/5}, & 6300 < Re < 10000, \text{ mixed flow} & (5.2.8) \\[2mm] 0.09\,Re^{-1/5}, & Re > 10000, \text{ turbulent} & (5.2.9) \end{cases}$$

where the lowest regime (Re<500) is termed the low laminar region, the next (500< Re <6300) the laminar flow region, the mixed flow region, and the last the turbulent region. To prevent vibrations within the coils due to turbulent flow, the IP trap coils are connected hydraulically such that the fluid flow stays within the laminar flow region.

In order to verify the results of Ref. [1], we constructed a simple test setup as illustrated diagrammatically in Fig. 5.6. The coil consisted of 6 turns of copper refrigerator tubing (3/16" OD tubing from Mueller Industries) with a coil diameter of 9.4 cm and 3.24 mm inner diameter. Water pressure was monitored before and after the coil with pressure gauges and the flow rate was measured with a Proteus Industries 804PN2 flow meter that was manually calibrated. The water source was domestic water at an initial pressure of approximately 45 psi. The flow rate was varied
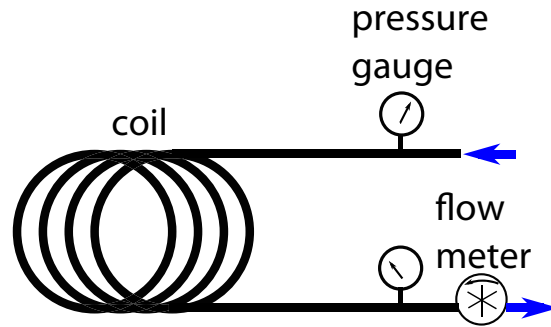
Figure 5.6: Diagram of the test setup for measuring the water pressure drop and fluid flow through a test coil.

(a) with burrs

(b) burrs removed
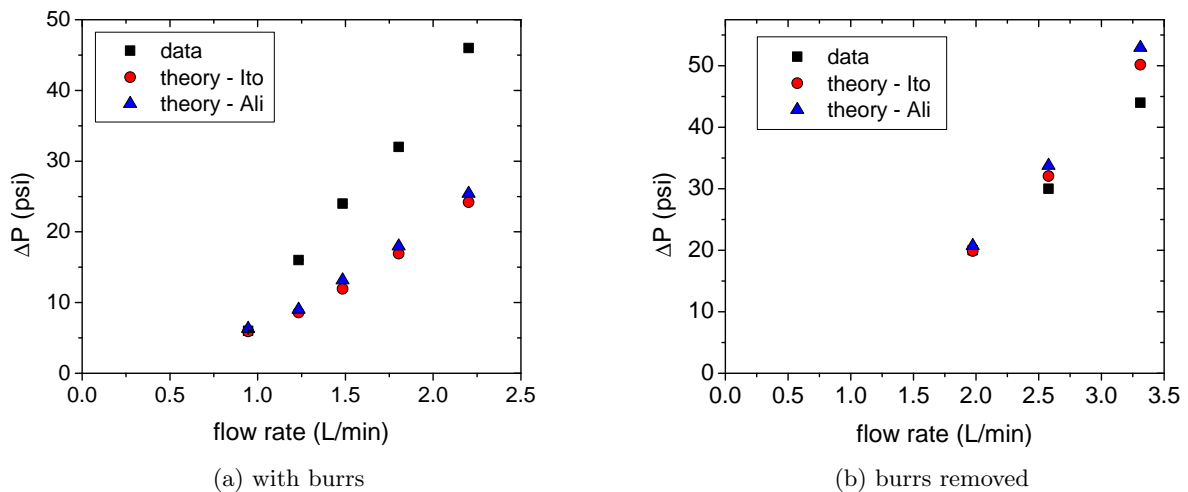
Figure 5.7: Measured pressure drops and flow rates through the test setup. Initially the ends of test coil had burrs left after cutting the copper tubing. After filing the burrs, the measured pressure drops more closely follow the phenomenological theories of Ali [1] and Ito [81].

by throttling a valve before the coil. Shown in Fig. 5.7 are two attempts to verify the results of Ref. [1]. Fig. 5.7a shows marked disagreement with the predictions of Ref. [1] and another prediction by Ref. [81]. In the case of Fig. 5.7a, both ends of the coil had small burrs that resulted in a much larger pressure drop. Fig. 5.7b is after the burrs were removed and exhibits better agreement with the predictions of Refs. [81, 1] and so the predictions can be trusted.

Another issue is the question of heat transfer from the current carrying coil to the cooling
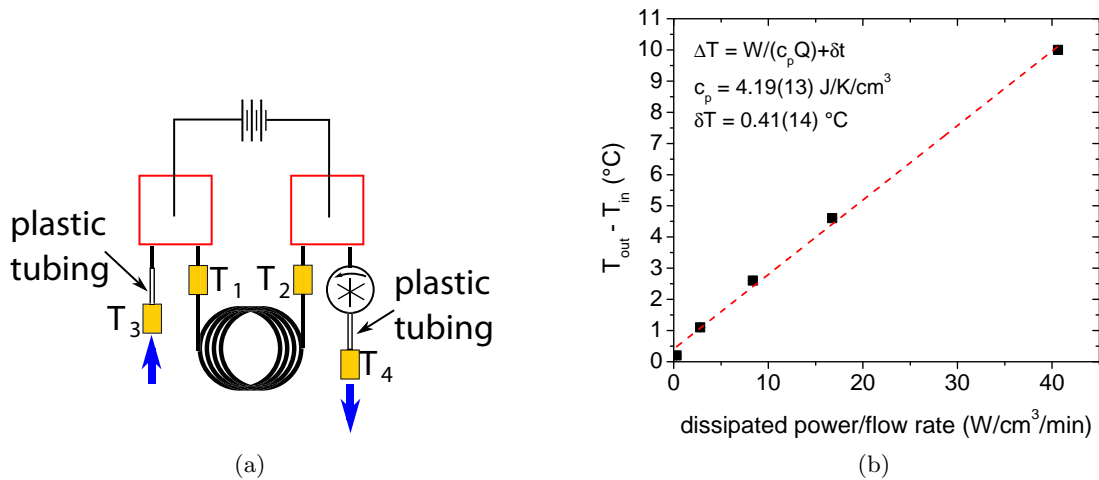
Figure 5.8: a) Setup for measuring heat transfer from the coil to the cooling water. Thermocouples (indicated by T_i) were attached to brass tubing connectors, and covered with insulation, to measure fluid temperature. The temperature increase of the fluid was measured from $T_4 - T_3$, which were isolated thermally from the coil with a segment of plastic tubing, while passing current through the test coil and measuring the fluid flow rate with the flow meter. b) Measured fluid temperature increase versus the power/flow rate ratio.

water. The test setup for measuring heat transfer is shown in Fig. 5.8a. The test coil used in this case was a bias coil used in an old magnetic trap from S1B05; the coil is roughly 9.5 cm in diameter with four turns per layer and four layers and a total resistance of $\approx 11m\Omega$. The coil had been in use for an extended period of time with domestic water and so the inside of the tubing was oxidized. Water and electrical power were connected to the coil through two copper cooling plates drawn as the red hollow squares in Fig. 5.8a. Water connections were made with brass connectors onto which thermocouples were attached (denoted T_1 through T_4) and then covered with insulation. Thermocouples T_3 and T_4 were isolated thermally and electrically from coil by small segments of plastic tubing and therefore measure the incoming and outgoing water temperature, respectively. The flow rate was measured using the manually calibrated flow meter from above.

The fluid temperature increase $(T_4 - T_3)$ as a result of power dissipated in the test coil is shown in Fig. 5.8b for currents up to 200 A. The temperature increase was fit to $\Delta T = \frac{W}{c_p Q} + \delta T$, where W is the dissipated power in Watts, Q the volumetric flow rate, c_p the specific heat capacity

including reduction due to power heat transfer [6] , and δT an offset due to calibration offsets between the two thermocouples. The value of the specific heat capacity from the fit, shown in Fig. 5.8b, is $c_p = 4.19(13)$ J/K/cm^3 (error bar is purely statistical), which is consistent with water ($c_p = 4.186$ J/K/cm^3 [110]) indicating that the heat conduction from the coil to the water is not substantially hampered by the oxide layer on the inner wall of the tubing.

Now that we know what flow rate to expect and that the oxide layer inside the copper tubing does not significantly impair heat transfer for coils of the size used for the trap, we can decide on an inner diameter for the tubing. The upper limit on the temperature for the coils is 45°C, which is the glass-liquid transition temperature [7] for the epoxy used to bind the turns of the coils together [99]. The chilled water that will be used to cool the trap is maintained at a temperature of 10° and differential pressure of 65 psi. We want to choose the inner diameter for the tubing such that we stay well below the glass-liquid transition even in a fault condition where the pressure is drastically reduced.

The coils which dissipate the most power are the bias coils which, at their design field of 800G ($I_bias = 241$ A), dissipate roughly 500 W each. Assuming the coils are in parallel hydraulically such that the $\Delta P = 65$ psi for each coil, and using Eqn. (5.2.3) to calculate the flow rates for the bias coils and then calculating the temperature increase, we find that an inner diameter of 0.08 inches should provide a sufficiently safe temperature increase. For $\Delta P = 65$ psi the coils should pass 0.4 L/min each (corresponding to Re = 3200 and thus laminar flow), which will limit the temperature increase to $\Delta T = 13$°C. If the water pressure drops to 32 psi, the then the temperature increase is predicted to be $\Delta T = 22$°C, which keeps the total temperature well below the maximum temperature for the epoxy. Similarly for the pinch coils, which dissipate 310 W total while the trap is running, the calculated flow rates are 0.5 L/min and 0.3 L/min for 65 psi and 32 psi, respectively, assuming that the coils are in series hydraulically. For these flow rates the predicted temperature increases

---

[6] If the heat transfer from the coil to the water is poor, then the measured heat capacity will deviated substantially from the published values for water.

[7] At the glass-liquid transition temperature the epoxy will transition from a glass state to a molten state[5] with reduced mechanical strength [99].

are $\Delta T = 9°C$ and $\Delta T = 15°C$ for 65 psi and 32 psi, respectively. Therefore the coils should be able to safely operate under normal and some abnormal conditions with an inner tubing diameter of 0.08 inches.

5.3   Magnetic trap details

From the considerations in the previous sections we designed bias and pinch coils and the Ioffe bars with the ability to reach 800 G as a design goal for the bias coils in order to reach high magnetic field Feshbach resonances and trap frequencies comparable to our existing IP trap: $f_{radial} = 125$ Hz and $f_{axial} = 25$ Hz. At the currents $I_{bias} = 193.75A$, $I_{pinch} = I_{Ioffe} = 186A$ the new trap is calculated to achieve $f_{radial} = 118Hz$ and $f_{axial} = 18Hz$ with the field minimum of the trap $B_0 = 4$ G. The coils were wound from 0.125" oxygen-free copper square tubing with an inner circular diameter of 0.080". The tubing was purchased from Small Tube Products and then coated in Kapton polyimide tape by S&W Wire. The details of the coils and their field strengths are shown in Table 5.2 and the measured coil resistances are shown in Table 5.3.

For constructing the coils as well as designing and constructing the structure of the magnetic trap, I have Tracy Keep to thank. The trap structure was built from Garolite G-10, a glass phenolic[8]. The bias coils were each wound directly onto each half of the trap structure applying Araldite 2011 epoxy, which has been found to adhere well to Kapton [173]. The trap structure is bolted together with titanium bolts. Given the low thermal expansion of G-10 (it is comparable to titanium) the spacer between the two halves is also made from G-10. Nestled inside the trap structure are the Fast B pair, which consist of two layers with two turns per layer of 17 gauge magnet wire. The pinch coils were each wound onto a separate G-10 structure, which bolts inside of the trap structure. This means that the pinch coils can be removed in the future if the full IP trap is no longer needed. Lastly, the Ioffe bars were wound onto a separate form and inserted through the pinch structure. A photograph of the trap is shown in Fig. 5.9b as well as a CAD rendering of the new trap with

---

[8] Earlier traps were constructed from Garolite G-11, but, as noted by Tracy Keep, this material tends to delaminate when it is machined.

coil	$R_{measured}$ (mΩ)	$R_{expected}$ (mΩ)
North Bias	9.3(2)(10)	10.8
South Bias	9.2(2)(10)	10.8
North Pinch	6.1(2)(10)	6.2
South Pinch	6.1(2)(10)	6.2
Upper Ioffe bar	1.50(2)(100)	0.7
Lower Ioffe bar	1.38(2)(100)	0.7
North Fast B	15.1(6)	16
South Fast B	16.4(6)	16

Table 5.3: Measured and predicted magnet coil resistances. Measurement of the trap coils was subject to a $\sim 1m\Omega$ due to uncertainties in the lead length, which is represented by the second error bar. The measured values of the coils resistances agree with the calculated values within the error bars with the exception of the bias coils. The resistances were calculated from the resistivity of copper (1.71 $\mu\Omega$-m) and the dimensions of the tubing and coils.

our existing vacuum chamber and Quadrupole trap coils in Fig. 5.9a. In Figs. 5.9b and 5.9a the sliding stage onto which the trap attaches is visible. This stage will allow the trap to be easily positioned over the science cell (not shown) and then locked into position.

Since the square tubing has a relatively small inner diameter, which impedes water flow, the square tubing is mated to standard round copper tubing as soon as it can be parted from the trap structure. The square tubing was mated to the round tubing by crimping the round tubing onto the square tubing and then soldering the joint. The square tubing was strain relieved against the trap structure to reduce stress on the joints. The round tubing was then coated in heat shrink tubing to provide electrical insulation and then routed to an electrical power and water junction.

Optical access to the atoms is greatly improved compared to our existing IP trap on two fronts.

The first improvement is the increased access for imaging lenses. A 25mm diameter aperture was cut between the bias coils (it can be seen in Fig. 5.9b) allowing for optics to be inserted as close as 2.7 cm from the center of the trap. This aperture limits the numerical aperture[9] to NA = 0.26. Smaller optics (up to 14 mm in outer diameter) can be inserted in this direction with unobstructed access to the science cell. The maximum numerical aperture is then limited by the dimensions of the science cell to NA = 0.62. Additionally, small, custom-made lens tubes can be bolted into the trap in between the Ioffe bars from either side, or from below the trap, and allows for 1/2 inch optics to be positioned as close as 1.35 cm from the IP trap center allowing a maximum numerical aperture of 0.39.

The openings also allows horizontal beams to enter the science cell through the pinch coils (in the z-direction from Fig. 5.4d) at up to 22 ° in the zx-plane (limited by the pinch coil form) off of normal to the science cell and 13 ° (limited by the Ioffe bars) in the yz-plane. For beams entering the science cell from above between the bias coils in the xy-plane, the system accommodates beams up to 1 mm in diameter at the science cell at an angle 45° off of the normal to the science cell.

Currently the new IP trap is assembled and being tested. Control electronics for the IP trap current have been built and will allow for the high current transistors to be tested to check that they perform as specified. Once the electronics are ready, and the experiment is at a good point for a major upgrade, then the new IP trap will be installed.

---

[9] The numerical aperture is defined NA = $n \sin(\theta)$ where n is the index of refraction and θ is half of the maximum angle of light that transmits through the aperture from a point source at some distance.
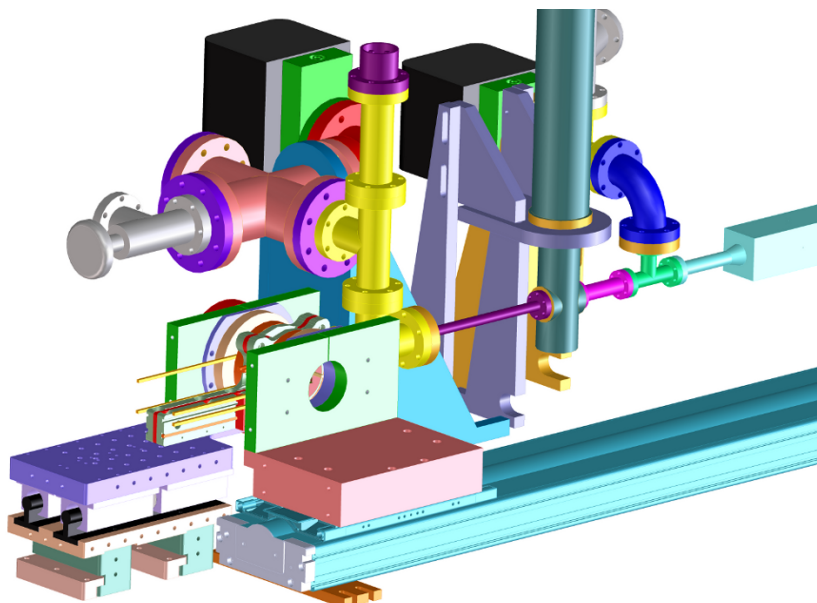
(a)
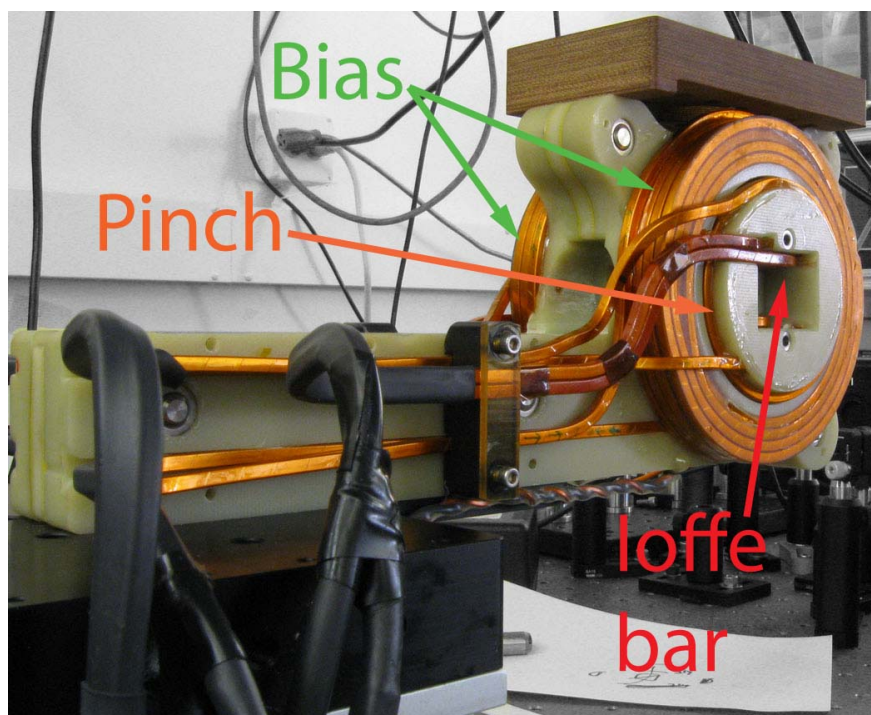
(b)

Figure 5.9: a) CAD rendering of the vaccuum chamber with the new trap installed and aligned with the Quadrupole coils on the cart track. b) Photograph of the assembled Ioffe-Pritchard trap with the visible coils labeled. The trap structure is made from Garolite G-10, which is the light green material in the photograph. The coils are made from Kapton coated square tubing (the amber-colored tubing in the photo), which is mated to standard round tubing by crimping and soldering the tubes together and then the round tubing is covered in heat shrink resulting in the black tubes shown in the foreground.

Chapter 6

Conclusions and future directions

6.1   Conclusions

In this thesis I have described the various upgrades to the apparatus and our understanding that enabled the study of Feshbach molecule formation as well as Efimov physics in our ultracold atomic mixture, ^{40}K – ^{87}Rb. The overall stability of the system was aided with the replacement of the old K laser system, which replaced a K slave laser maintained at $-40°$C and a master laser maintained at $-10°$ with a tapered amplifier and master laser maintained at temperatures just under room temperature. Studies of the performance of the Fast B were detailed, which was an integral part of the apparatus for the studies of Feshbach molecule formation and Efimov physics. Additionally I detailed the new Rb microwave setup and systematics and calibrations of our atom number measurements.

I have presented measurements of Feshbach molecule magneto-association in our Bose-Fermi mixtures system in terms of formation in the limit of fast magnetic-field sweep (perturbative limit) and the limit slow magnetic-field sweeps (saturated limit). In the perturbative limit, the initial molecule creation rate was shown to be determined the Fano-Feshbach resonance parameters and the density overlap of the boson and fermion atom clouds. In the saturated limit, the governing parameter is the phase-space density of the clouds and not just the spatial density. Here I presented measurements of the molecule creation efficiency as a function of the atomic T/T_F and fit the measurements to the phenomenological SPSS model. The SPSS model only allows molecule formation between two atoms that are "close enough" in phase-space, where "close enough" is defined by the

sole adjustable parameter of the model. The molecule creation efficiency data were fit to the SPSS model, and the value of the adjustable parameter agreed with similar measurements in homonuclear systems. Measurements of the molecular expansion energy were also presented and were found to be in excess of what the SPSS model would have predicted. The task of minimizing the molecular quantum degeneracy was explored using the SPSS model in the limit of the majority atom being the fermion where no method to create a degenerate molecular gas was uncovered.

Measurements of three-body recombination rates for Bose-Bose-Fermi collisions, as well as atom-molecule collision rates, were presented in order to study Efimov physics in ^{40}K – ^{87}Rb. This study was prompted by the discovery of universality in the three-body parameter(which sets the location of Efimov resonances) for Efimov physics in homonuclear systems and the discovery of Efimov resonances in ^{41}K – ^{87}Rb. In homonuclear systems, the three-body parameter was found to set the location of the first Efimov resonance in three-body recombination at $a_-^{(1)} = -9.1 r_{vdW}$, and since the van der Waals lengths between ^{40}K – ^{87}Rb and ^{41}K – ^{87}Rb are very similar, we expected to find resonances at nearly the same scattering lengths as ^{41}K – ^{87}Rb. However, we did not find evidence for Efimov resonances in three-body recombination within the accessible range of scattering lengths, in stark contrast with the results of ^{41}K – ^{87}Rb. A feature in atom-molecule collisions was observed in the the Rb+molecule collisions that was absent in collisions between K atoms and molecules, as well as distinguishable atoms and molecules, in agreement with Efimov physics. Since we did not observe features in the same locations as ^{41}K – ^{87}Rb, we found no evidence for universality in the three-body parameter for heteronuclear systems. Observations in other heteronuclear systems will help resolve this issue.

6.2   Future work

The field of Efimov physics and many-body collisions has a few options for further study. One important question to answer is why did we not observe an a_- feature in ^{87}Rb – ^{87}Rb – ^{40}K collisions, whereas in ^{87}Rb – ^{87}Rb – ^{41}K one was observed? This can be addressed by either repeating the measurements done in ^{41}K – ^{87}Rb or by measuring three-body recombination rates in
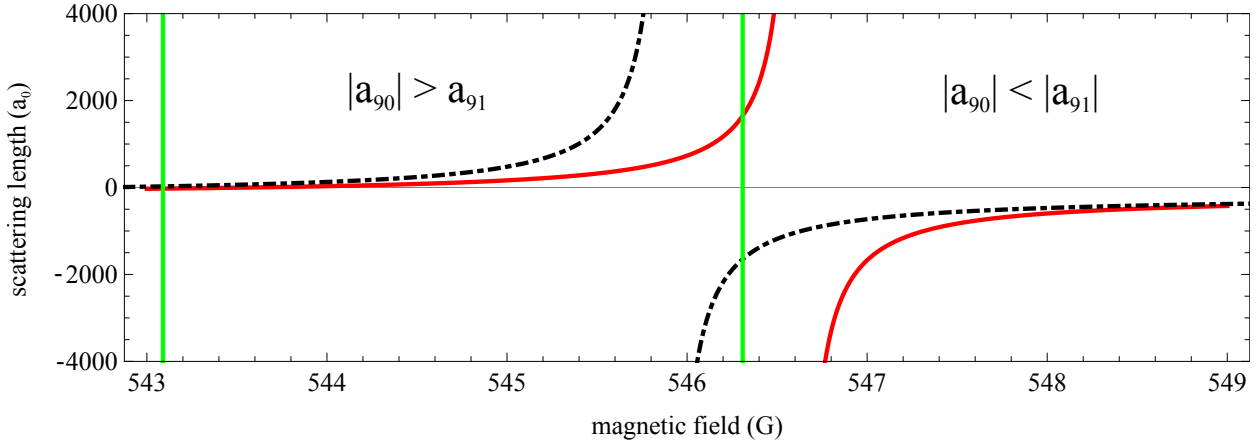
Figure 6.1: Interspecies scattering length for the 545.9G Feshbach resonance between K in the $|9/2, -9/2\rangle$ hyperfine state and Rb in the $|1, 0\rangle$ state (a_{90}, dash-dotted curve) and the 546.618 G resonance between K in the $|9/2, -9/2\rangle$ and Rb in the $|1, 1\rangle$ state (a_{91}, solid curve). In the region between the vertical lines, a_{90} is the dominant interspecies scattering length, whereas to the right of the right-most vertical line, a_{91} is dominant.

other isotopic mixtures. Amongst the published Feshbach resonances in all the other KRb isotopic mixtures, the only two that are borderline entrance-channel dominated are in ^{41}K-^{85}Rb: the theoretically predicted resonances at 185.2 G and 672.19 G [140] have $s_{res} = 3.6$ and $s_{res} = 5.5$, respectively. However, this mixture would be quite challenging to realize at ultracold temperatures without a third atomic species in the mixture given ^{41}K's small background scattering length ($a_{bg} \approx 60a_0$ [103]) and ^{85}Rb's large negative background scattering length ($a_{bg} = -443a_0$ [24]). If we expand our search to include Feshbach resonances which are borderline closed-channel dominated, then one candidate is the 317.9 G resonance in ^{39}K-^{87}Rb [140]. This resonance has a magnetic-field width of 7.6 G and $s_{res} \approx 0.7$. Another is the 78.9 G resonance in ^{41}K $- ^{87}$Rb used by LENS which has $s_{res} = 0.8$. Both of these resonances are at easily accessible magnetic fields.

Another interesting theoretical proposal involves measuring three-body recombination in unequal mass systems with overlapping Feshbach resonances [42]. This reference predicts the scattering length dependence for various three-body collision processes for the case of three distinguishable particles with only two resonant scattering lengths. In ^{40}K $- ^{87}$Rb there is another 3 G wide s-wave Feshbach resonance at 545.9 G [140] between the spin states $|9/2, -9/2\rangle$ in K and $|1, 0\rangle$ in Rb. The

degree to which this Feshbach resonance overlaps with the one used in Chapters 3 and 4 is shown in Fig. 6.1. Ref. [42] predicts that the event rate coefficient for recombining into deeply bound molecules changes from simple a^4 scaling to $a_{90}^2 a_{91}^2$ in the limit where one scattering is much larger than the other. The recombination rate into Feshbach molecules is also predicted to scale as $a_{90}^2 a_{91}^2$.

Other topics in many-body collisions to explore involve exploring Efimov physics with closed-channel dominated s-wave Feshbach resonances, where r_{eff} becomes of considerable magnitude compared to r_{vdW}. For systems of three identical bosons in the recombination rates are predicted to depend upon r_{eff} as well as the scattering length: for $|a| \gg r_{\text{eff}}$, three-body recombination scales as a^4, but for $|a| \ll r_{\text{eff}}$ recombination scales as $a^{9/2} r_{\text{eff}}^{1/2}$ [128]. It is also predicted that near closed-channel dominated resonances, inelastic processes leading to deeply bound molecules are suppressed for bosons and enhanced for fermions [156] in contrast to what is seen with entrance-channel dominated resonances.

Since our three-body recombination spectra in the range of accessible scattering lengths was devoid of Efimov resonances, we can also consider venturing into many-body physics territory. One promising direction is to examine the effects of strong Bose-Fermi interactions on the boson condensation temperature, T_c. Ref. [59], the authors predict a reduction in T_c as a consequence of the boson-fermion interaction leading to the vanishing of T_c at a small positive scattering length. Examining the quantum phase diagram of a strongly interacting Bose-Fermi mixture also is a rich avenue to take. Ref. [102] predicts the presence of first- and second-order quantum phase transitions as well as path dependent (in terms of varying the scattering length) quantum phases. This hysteretic effect would manifest itself in terms of a jump in the condensate number. An additional route of research is to examine the BEC-BCS cross over in the presence of bosonic impurity; this creates the possibility of new physics as well as a reliable thermometer.

Bibliography

[1] S. Ali. Pressure drop correlations for flow through regular helical coil tubes. *Fluid Dynamics Research*, 28(4):295–310, Apr. 2001.

[2] R. D. Amado and J. V. Noble. Efimov's Effect: A New Pathology of Three-Particle Systems. II. *Phys. Rev. D*, 5(8):1992–2002, 1972.

[3] M. H. Anderson, J. R. Ensher, M. R. Matthews, C. E. Wieman, and E. A. Cornell. Observation of Bose-Einstein Condensation in a Dilute Atomic Vapor. *Science*, 269(5221):198–201, 1995.

[4] M. R. Andrews, C. G. Townsend, H.-J. Miesner, D. S. Durfee, D. M. Kurn, and W. Ketterle. Observation of Interference Between Two Bose Condensates. *Science*, 275(5300):637–641, 1997.

[5] C. A. Angell. Formation of glasses from liquids and biopolymers. *Science*, 267(5206):1924–1935, 1995.

[6] M. A. Baranov, M. S. Mar'enko, V. S. Rychkov, and G. V. Shlyapnikov. Superfluid pairing in a polarized dipolar Fermi gas. *Phys. Rev. A*, 66:013606, Jul 2002.

[7] G. Barontini, C. Weber, F. Rabatti, J. Catani, G. Thalhammer, M. Inguscio, and F. Minardi. Observation of Heteronuclear Atomic Efimov Resonances. *Phys. Rev. Lett.*, 103(4):043201, July 2009.

[8] G. Barontini, C. Weber, F. Rabatti, J. Catani, G. Thalhammer, M. Inguscio, and F. Minardi. Erratum: Observation of Heteronuclear Atomic Efimov Resonances [Phys. Rev. Lett. 103, 043201 (2009)]. *Phys. Rev. Lett.*, 104(5):059901, Feb. 2010.

[9] Q. Beaufils, A. Crubellier, T. Zanon, B. Laburthe-Tolra, . Marchal, L. Vernac, and O. Gorceix. Radio-frequency association of molecules: an assisted Feshbach resonance. *Eur. Phys. J. D*, 56:99–104, 2010. 10.1140/epjd/e2009-00269-3.

[10] P. F. Bedaque, E. Braaten, and H.-W. Hammer. Three-body Recombination in Bose Gases with Large Scattering Length. *Phys. Rev. Lett.*, 85(5):908–11, July 2000.

[11] T. Bergeman, G. Erez, and H. J. Metcalf. Magnetostatic trapping fields for neutral atoms. *Phys. Rev. A*, 35:1535–1546, Feb 1987.

[12] M. Berninger, A. Zenesini, B. Huang, W. Harm, H.-C. Nägerl, F. Ferlaino, R. Grimm, P. S. Julienne, and J. M. Hutson. Universality of the Three-Body Parameter for Efimov States in Ultracold Cesium. *Phys. Rev. Lett.*, 107(12):120401, 2011.

[13] H. A. Bethe. Theory of the effective range in nuclear scattering. *Phys. Rev.*, 76:38–50, Jul 1949.

[14] M. J. Bijlsma, B. A. Heringa, and H. T. C. Stoof. Phonon exchange in dilute Fermi-Bose mixtures: Tailoring the Fermi-Fermi interaction. *Phys. Rev. A*, 61:053601, Apr 2000.

[15] S. Blatt. *Ultracold Collisions and Fundamental Physics with Strontium*. PhD thesis, University of Colorado - Boulder, 2011.

[16] S. N. Bose. Plancks gesetz und lichtquantenhypothese. *Z. Phys.*, 26(1):178–181, 1924. 10.1007/BF01327326.

[17] E. Braaten and H.-W. Hammer. Three-Body Recombination into Deep Bound States in a Bose Gas with Large Scattering Length. *Phys. Rev. Lett.*, 87(16):160407, Oct. 2001.

[18] E. Braaten and H.-W. Hammer. Universality in few-body systems with large scattering length. *Phys. Rep.*, 428(5-6):259–390, June 2006.

[19] E. Braaten, H.-W. Hammer, and M. Kusunoki. Universal equation for Efimov states. *Phys. Rev. A*, 67(2):022505, Feb. 2003.

[20] B. H. Bransden and C. J. Joachain. *Physics of Atoms and Molecules*. Prentice Hall, second edition, 2003.

[21] E. A. Burt, R. W. Ghrist, C. J. Myatt, M. J. Holland, E. A. Cornell, and C. E. Wieman. Coherence, Correlations, and Collisions: What One Learns about Bose-Einstein Condensates from Their Decay. *Phys. Rev. Lett.*, 79(3):337–340, 1997.

[22] Q. Chen, J. Stajic, S. Tan, and K. Levin. BCS-BEC crossover: From high temperature superconductors to ultracold superfluids. *Physics Reports*, 412(1):1 – 88, 2005.

[23] C. Chin. Universal scaling of Efimov resonance positions in cold atoms systems. arXiv:1111.1484v2.

[24] C. Chin, R. Grimm, P. Julienne, and E. Tiesinga. Feshbach resonances in ultracold gases. *Rev. Mod. Phys.*, 82(2):1225–1286, Apr. 2010.

[25] J. Chwedeńczuk, K. Góral, T. Köhler, and P. S. Julienne. Molecular Production in Two Component Atomic Fermi Gases. *Phys. Rev. Lett.*, 93:260403, 2004.

[26] P. Courteille, R. S. Freeland, D. J. Heinzen, F. A. van Abeelen, and B. J. Verhaar. Observation of a feshbach resonance in cold atom scattering. *Phys. Rev. Lett.*, 81:69–72, Jul 1998.

[27] T. D. Cumby, J. D. Perreault, R. A. Shewmon, M. Hu, and D. S. Jin. Feshbach molecule formation in a bose-fermi mixture. *Phys. Rev. A (in preparation)*.

[28] T. D. Cumby, R. A. Shewmon, M. Hu, and D. S. Jin. *Phys. Rev. Lett. (in preparation)*.

[29] F. Dalfovo, S. Giorgini, L. P. Pitaevskii, and S. Stringari. Theory of Bose-Einstein condensation in trapped gases. *Rev. Mod. Phys.*, 71(3):463–512, Apr 1999.

[30] B. Damski, L. Santos, E. Tiemann, M. Lewenstein, S. Kotochigova, P. Julienne, and P. Zoller. Creation of a dipolar superfluid in optical lattices. *Phys. Rev. Lett.*, 90:110401, Mar 2003.

[31] K. B. Davis, M. O. Mewes, M. R. Andrews, N. J. van Druten, D. S. Durfee, D. M. Kurn, and W. Ketterle. Bose-Einstein Condensation in a Gas of Sodium Atoms. *Phys. Rev. Lett.*, 75:3969–3973, Nov 1995.

[32] M. Debatin, T. Takekoshi, R. Rameshan, L. Reichsöllner, F. Ferlaino, R. Grimm, R. Vexiau, N. Bouloufa, O. Dulieu, and H.-C. Nägerl. Molecular spectroscopy for ground-state transfer of ultracold RbCs molecules. *Phys. Chem. Chem. Phys.*, 18926-18935, Aug. 2011.

[33] B. DeMarco. *Quantum Behavior of an Atomic Fermi Gas.* PhD thesis, University of Colorado - Boulder, 2000.

[34] B. DeMarco and D. S. Jin. Onset of Fermi Degeneracy in a Trapped Atomic Gas. *Science*, 285(5434):1703–1706, 1999.

[35] B. DeMarco, H. Rohner, and D. S. Jin. An enriched ^{40}K source for fermionic atom studies. *Rev. Sci. Instrum.*, 70(4):1967–1969, 1999.

[36] A. Derevianko, W. R. Johnson, M. S. Safronova, and J. F. Babb. High-precision calculations of dispersion coefficients, static dipole polarizabilities, and atom-wall interaction constants for alkali-metal atoms. *Phys. Rev. Lett.*, 82(18):3589–3592, May 1999.

[37] C. D'Errico, M. Zaccanti, M. Fattori, G. Roati, M. Inguscio, G. Modugno, and A. Simoni. Feshbach resonances in ultracold ^{39} K. *New J. Phys.*, 9(7):223, July 2007.

[38] F. Deuretzbacher, K. Plassmeier, D. Pfannkuche, F. Werner, C. Ospelkaus, S. Ospelkaus, K. Sengstock, and K. Bongs. Heteronuclear molecules in an optical lattice: Theory and experiment. *Phys. Rev. A*, 77(3):032726, Mar. 2008.

[39] I. Di Piazza and M. Ciofalo. Numerical prediction of turbulent flow and heat transfer in helically coiled pipes. *International Journal of Thermal Sciences*, 49(4):653–663, Apr. 2010.

[40] K. Dieckmann, C. A. Stan, S. Gupta, Z. Hadzibabic, C. H. Schunck, and W. Ketterle. Decay of an Ultracold Fermionic Lithium Gas near a Feshbach Resonance. *Phys. Rev. Lett.*, 89:203201, Oct 2002.

[41] J. P. D'Incao and B. D. Esry. Mass dependence of ultracold three-body collision rates. *Phys. Rev. A*, 73(3):030702, Mar. 2006.

[42] J. P. D'Incao and B. D. Esry. Ultracold Three-Body Collisions near Overlapping Feshbach Resonances. *Phys. Rev. Lett.*, 103(8):083202, Aug. 2009.

[43] J. P. D'Incao, H. Suno, and B. D. Esry. Limits on Universality in Ultracold Three-Boson Recombination. *Phys. Rev. Lett.*, 93(12):123201, Sept. 2004.

[44] P. A. M. Dirac. On the theory of quantum mechanics. *Proc. R. Soc. A*, 112(762):661–677, 1926.

[45] B. Dobrescu and V. Pokrovsky. Production efficiency of Feshbach molecules in fermion systems. *Phys. Lett. A*, 350(1-2):154–158, Jan. 2006.

[46] E. A. Donley, N. R. Claussen, S. T. Thompson, and C. E. Wieman. Atom-molecule coherence in a Bose-Einstein condensate. *Nature*, 417(6888):529–533, May 2002.

[47] S. Dürr, T. Volz, A. Marte, and G. Rempe. Observation of molecules produced from a bose-einstein condensate. *Phys. Rev. Lett.*, 92(2):020406, Jan. 2004.

[48] V. Efimov. Energy levels arising from resonant two-body forces in a three-body system. *Phys. Lett. B*, 33(1):563–564, 1970.

[49] V. Efimov. Energy levels of three resonantly interacting particles. *Nucl. Phys. A*, 210(1):157–188, Aug. 1973.

[50] D. V. Efremov and L. Viverit. *p*-wave Cooper pairing of fermions in mixtures of dilute Fermi and Bose gases. *Phys. Rev. B*, 65:134519, Mar 2002.

[51] A. Einstein. Quantentheorie des einatomigen idealen gases. *Sitzungsber. Kgl. Preuss. Akad. Wiss.*, pages 261–267, 1924.

[52] A. Einstein. Quantentheorie des einatomigen idealen gases. 2. *Sitzungsber. Kgl. Preuss. Akad. Wiss.*, pages 3–14, 1925.

[53] B. D. Esry, C. H. Greene, and J. P. Burke. Recombination of three atoms in the ultracold limit. *Phys. Rev. Lett.*, 83(9):1751–1754, Aug. 1999.

[54] F. Ferlaino, C. D'Errico, G. Roati, M. Zaccanti, M. Inguscio, G. Modugno, and A. Simoni. Erratum: Feshbach spectroscopy of a K-Rb atomic mixture [Phys. Rev. A 73, 040702 (2006)]. *Phys. Rev. A*, 74(3):039903, Sept. 2006.

[55] F. Ferlaino, C. D'Errico, G. Roati, M. Zaccanti, M. Inguscio, G. Modugno, and A. Simoni. Feshbach spectroscopy of a K-Rb atomic mixture. *Phys. Rev. A*, 73(4):040702, Apr. 2006.

[56] F. Ferlaino, S. Knoop, M. Berninger, W. Harm, J. P. D'Incao, H.-C. Nägerl, and R. Grimm. Evidence for Universal Four-Body States Tied to an Efimov Trimer. *Phys. Rev. Lett.*, 102(14):140401, Apr. 2009.

[57] F. Ferlaino, A. Zenesini, M. Berninger, B. Huang, H. Nägerl, and R. Grimm. Efimov resonances in ultracold quantum gases. *Few-Body Syst.*, 51(2-4):113–133, 2011.

[58] E. Fermi. Zur quantelung des idealen einatomigen gases. *Z. Phys.*, 36:902–912, 1926. 10.1007/BF01400221.

[59] E. Fratini and P. Pieri. Pairing and condensation in a resonant bose-fermi mixture. *Phys. Rev. A*, 81(5):051605, May 2010.

[60] J. M. Goldwin. *Quantum Degeneracy and Interactions in the ^{87}Rb -^{40}K Bose-Fermi Mixture.* PhD thesis, University of Colorado, 2005.

[61] M. Greiner, C. A. Regal, and D. S. Jin. Emergence of a molecular BoseEinstein condensate from a Fermi gas. *Nature*, 426:537–540, December 2003.

[62] M. Greiner, C. A. Regal, and D. S. Jin. Probing the Excitation Spectrum of a Fermi Gas in the BCS-BEC Crossover Regime. *Phys. Rev. Lett.*, 94(7):070403, Feb 2005.

[63] G. F. Gribakin and V. V. Flambaum. Calculation of the scattering length in atomic collisions using the semiclassical approximation. *Phys. Rev. A*, 48(1):546, 1993.

[64] N. Gross, Z. Shotan, S. Kokkelmans, and L. Khaykovich. Observation of Universality in Ultracold ^{7}Li Three-Body Recombination. *Phys. Rev. Lett.*, 103(16):163202, Oct. 2009.

[65] N. Gross, Z. Shotan, S. Kokkelmans, and L. Khaykovich. Nuclear-Spin-Independent Short-Range Three-Body Physics in Ultracold Atoms. *Phys. Rev. Lett.*, 105(10):103203, Sept. 2010.

[66] N. Gross, Z. Shotan, O. Machtey, S. Kokkelmans, and L. Khaykovich. Study of Efimov physics in two nuclear-spin sublevels of ^{7}Li. *Comptes Rendus Physique*, 12(1):4–12, Jan. 2011.

[67] G. J. Hanna and D. Blume. Energetics and structural properties of three-dimensional bosonic clusters near threshold. *Phys. Rev. A*, 74(6):063604, Dec. 2006.

[68] T. M. Hanna, T. Köhler, and K. Burnett. Association of molecules using a resonantly modulated magnetic field. *Phys. Rev. A*, 75(1):013606, Jan. 2007.

[69] C. V. Heer. Feasibility of containment of quantum magnetic dipoles. *Review of Scientific Instruments*, 34(5):532–537, 1963.

[70] H. Heiselberg, C. J. Pethick, H. Smith, and L. Viverit. Influence of induced interactions on the superfluid transition in dilute fermi gases. *Phys. Rev. Lett.*, 85:2418–2421, Sep 2000.

[71] K. Helfrich and H. Hammer. On the Efimov Effect in Higher Partial Waves. *J. Phys. B*, 44(21):215301, 2011.

[72] K. Helfrich, H.-W. Hammer, and D. S. Petrov. Three-body problem in heteronuclear mixtures with resonant interspecies interaction. *Phys. Rev. A*, 81(4):042715, Apr. 2010.

[73] M.-S. Heo, T. T. Wang, C. A. Christensen, T. M. Rvachov, D. A. Cotta, J.-H. Choi, Y.-R. Lee, and W. Ketterle. Formation of ultracold fermionic nali feshbach molecules. *Phys. Rev. A*, 86:021602, Aug 2012.

[74] J. Herbig, T. Kraemer, M. Mark, T. Weber, C. Chin, H.-C. Nägerl, and R. Grimm. Preparation of a pure molecular quantum gas. *Science*, 301(5639):1510–1513, Sept. 2003.

[75] E. Hodby, S. T. Thompson, C. A. Regal, M. Greiner, A. C. Wilson, D. S. Jin, E. A. Cornell, and C. E. Wieman. Production efficiency of ultracold feshbach molecules in bosonic and fermionic systems. *Phys. Rev. Lett.*, 94(12):120402, 2005.

[76] W. F. Holmgren, M. C. Revelle, V. P. A. Lonij, and A. D. Cronin. Absolute and ratio measurements of the polarizability of Na, K, and Rb with an atom interferometer. *Phys. Rev. A*, 81(5):053607, May 2010.

[77] J. H. Huckans, J. R. Williams, E. L. Hazlett, R. W. Stites, and K. M. O'Hara. Three-Body Recombination in a Three-State Fermi Gas with Widely Tunable Interactions. *Phys. Rev. Lett.*, 102(16):165302, Apr. 2009.

[78] S. Inouye, M. R. Andrews, J. Stenger, H. J. Miesner, D. M. Stamper-Kurn, and W. Ketterle. Observation of Feshbach resonances in a Bose-Einstein condensate. *Nature*, 392:151–154, 1998.

[79] S. Inouye, J. Goldwin, M. L. Olsen, C. Ticknor, J. L. Bohn, and D. S. Jin. Observation of heteronuclear Feshbach resonances in a mixture of Bosons and Fermions. *Phys. Rev. Lett*, 93(18):183201, 2004.

[80] M. S. Ioffe and R. I. Sobolev. Confinement of a plasma in a trap formed by a combined magnetic field. *J. Nucl. Energy, Part C Plasma Phys.*, 7(5):501, 1965.

[81] H. Ito. Friction Factors for Turbulent Flow in Curved Pipes. *Journal of Basic Engineering*, 81:123–134, 1959.

[82] S. Jochim, M. Bartenstein, A. Altmeyer, G. Hendl, C. Chin, J. H. Denschlag, and R. Grimm. Pure Gas of Optically Trapped Molecules Created from Fermionic Atoms. *Phys. Rev. Lett.*, 91(24):240402, Dec. 2003.

[83] K. Jones, E. Tiesinga, P. Lett, and P. Julienne. Ultracold photoassociation spectroscopy: Long-range molecules and atomic scattering. *Rev. Mod. Phys.*, 78(2):483–535, May 2006.

[84] P. S. Julienne. Ultracold molecules from ultracold atoms: a case study with the KRb molecule. *Faraday Discussions*, 142:361–388, 2009.

[85] W. Ketterle and D. E. Pritchard. Trapping and focusing ground state atoms with static fields. *Appl. Phys. B*, 54(5):403–406, 1992. 10.1007/BF00325386.

[86] C. Klempt, T. Henninger, O. Topic, M. Scherer, L. Kattner, E. Tiemann, W. Ertmer, and J. J. Arlt. Radio-frequency association of heteronuclear Feshbach molecules. *Phys. Rev. A*, 78(6):061602, Dec. 2008.

[87] C. Klempt, T. Henninger, O. Topic, J. Will, W. Ertmer, E. Tiemann, and J. Arlt. ^{40}K-^{87}Rb Feshbach resonances: Modeling the interatomic potential. *Phys. Rev. A*, 76(2):020701, Aug. 2007.

[88] S. Knoop, F. Ferlaino, M. Mark, M. Berninger, H. Schöbel, H.-C. Nägerl, and R. Grimm. Observation of an Efimov-like trimer resonance in ultracold atom-dimer scattering. *Nature Physics*, 5(3):227–230, Feb. 2009.

[89] T. Köhler, K. Góral, and P. S. Julienne. Production of cold molecules via magnetically tunable feshbach resonances. *Rev. Mod. Phys.*, 78(4):1311–1361, Dec. 2006.

[90] T. Köhler, K. Góral, and P. S. Julienne. Production of cold molecules via magnetically tunable feshbach resonances. *Rev. Mod. Phys.*, 78(4):1311–1361, 2006.

[91] E. Komatsu, K. M. Smith, J. Dunkley, C. L. Bennett, B. Gold, G. Hinshaw, N. Jarosik, D. Larson, M. R. Nolta, L. Page, D. N. Spergel, M. Halpern, R. S. Hill, A. Kogut, M. Limon, S. S. Meyer, N. Odegard, G. S. Tucker, J. L. Weiland, E. Wollack, and E. L. Wright. Seven-year Wilkinson Microwave Anisotropy Probe (WMAP) Observations: Cosmological Interpretation. *The Astrophysical Journal Supplement Series*, 192(2):18, 2011.

[92] T. Kraemer, M. Mark, P. Waldburger, J. G. Danzl, C. Chin, B. Engeser, A. D. Lange, K. Pilch, A. Jaakkola, H.-C. Nägerl, and R. Grimm. Evidence for Efimov quantum states in an ultracold gas of caesium atoms. *Nature*, 440(7082):315–318, Mar. 2006.

[93] K.-J. Kügler, W. Paul, and U. Trinks. A magnetic storage ring for neutrons. *Physics Letters B*, 72(3):422 – 424, 1978.

[94] A. D. Lange, K. Pilch, A. Prantner, F. Ferlaino, B. Engeser, H.-C. Nägerl, R. Grimm, and C. Chin. Determination of atomic scattering lengths from measurements of molecular binding energies near Feshbach resonances. *Phys. Rev. A*, 79(1):013622, Jan. 2009.

[95] C. Langmack, D. H. Smith, and E. Braaten. The Avalanche Mechanism for Atom Loss near an Atom-Dimer Efimov Resonance. arXiv:1205.2683v1.

[96] J. Leigh. *Control Theory*. The Institution of Engineering and Technology, 2nd edition, 2004.

[97] J. Leinaas and J. Myrheim. On the theory of identical particles. *Il Nuovo Cimento B (1971-1996)*, 37:1–23, 1977. 10.1007/BF02727953.

[98] H. J. Lewandowski. *Coherences and correlations in an ultracold Bose gas*. PhD thesis, University of Colorado - Boulder, 2002.

[99] H. I. LLC. Araldite 2011 datasheet, 2007.

[100] T. Loftus, C. A. Regal, C. Ticknor, J. L. Bohn, and D. S. Jin. Resonant control of elastic collisions in an optically trapped fermi gas of atoms. *Phys. Rev. Lett.*, 88:173201, Apr 2002.

[101] T. Lompe, T. B. Ottenstein, F. Serwane, A. N. Wenz, G. Zürn, and S. Jochim. Radio-Frequency Association of Efimov Trimers. *Science*, 330(6006):940–944, Nov. 2010.

[102] D. Ludwig, S. Floerchinger, S. Moroz, and C. Wetterich. Quantum phase transition in Bose-Fermi mixtures. *Phys. Rev. A*, 84(3):033629, Sept. 2011.

[103] M. Lysebo and L. Veseth. Feshbach resonances and transition rates for cold homonuclear collisions between ^{39}K and ^{41}K atoms. *Phys. Rev. A*, 81(3):032702, Mar. 2010.

[104] O. Machtey, D. A. Kessler, and L. Khaykovich. Universal Dimer in a Collisionally Opaque Medium: Experimental Observables and Efimov Resonances. *Phys. Rev. Lett.*, 108:130403, 2012.

[105] O. Machtey, Z. Shotan, N. Gross, and L. Khaykovich. Association of Efimov Trimers from a Three-Atom Continuum. *Phys. Rev. Lett.*, 108:210406, 2012.

[106] M. R. Matthews, B. P. Anderson, P. C. Haljan, D. S. Hall, C. E. Wieman, and E. A. Cornell. Vortices in a Bose-Einstein Condensate. *Phys. Rev. Lett.*, 83:2498–2501, Sep 1999.

[107] H. J. Metcalf and P. van der Straten. *Laser Cooling and Trapping*. Springer, 1999.

[108] A. L. Migdall, J. V. Prodan, W. D. Phillips, T. H. Bergeman, and H. J. Metcalf. First observation of magnetically trapped neutral atoms. *Phys. Rev. Lett.*, 54:2596–2599, Jun 1985.

[109] A. J. Moerdijk, B. J. Verhaar, and A. Axelsson. Resonances in ultracold collisions of ^{6}Li, ^{7}Li, and ^{23}Na. *Phys. Rev. A*, 51(6):4852–4861, 1995.

[110] D. B. Montgomery. *Solenoid Magnet Design: The Magnetic and Mechanical Aspects of Resistive and Superconducting Systems*. Wiley-Interscience, 1969.

[111] S. Nakajima, M. Horikoshi, T. Mukaiyama, P. Naidon, and M. Ueda. Measurement of an Efimov Trimer Binding Energy in a Three-Component Mixture of ^{6}Li. *Phys. Rev. Lett.*, 106(14):143201, Apr. 2011.

[112] M. Naraschewski and D. M. Stamper-Kurn. Analytical description of a trapped semi-ideal Bose gas at finite temperature. *Phys. Rev. A*, 58(3):2423–2426, Sep 1998.

[113] K. K. Ni, S. Ospelkaus, M. H. G. de Miranda, A. Pe'er, B. Neyenhuis, J. J. Zirbel, S. Kotochigova, P. S. Julienne, D. S. Jin, and J. Ye. A High Phase-Space-Density Gas of Polar Molecules. *Science*, 322(5899):231, 2008.

[114] E. Nielsen and J. Macek. Low-Energy Recombination of Identical Bosons by Three-Body Collisions. *Phys. Rev. Lett.*, 83(8):1566–1569, Aug. 1999.

[115] K. M. O'Hara, S. L. Hemmer, S. R. Granade, M. E. Gehm, J. E. Thomas, V. Venturi, E. Tiesinga, and C. J. Williams. Measurement of the zero crossing in a Feshbach resonance of fermionic ^{6}Li. *Phys. Rev. A*, 66:041401, Oct 2002.

[116] M. L. Olsen. *Experiments with Feshbach molecules in a Bose-Fermi mixture*. PhD thesis, University of Colorado, 2008.

[117] M. L. Olsen, J. D. Perreault, T. D. Cumby, and D. S. Jin. Coherent atom-molecule oscillations in a Bose-Fermi mixture. *Phys. Rev. A*, 80(3):030701(R), 2009.

[118] R. Onofrio, C. Raman, J. M. Vogels, J. R. Abo-Shaeer, A. P. Chikkatur, and W. Ketterle. Observation of superfluid flow in a bose-einstein condensed gas. *Phys. Rev. Lett.*, 85:2228–2231, Sep 2000.

[119] C. Ospelkaus, S. Ospelkaus, L. Humbert, P. Ernst, K. Sengstock, and K. Bongs. Ultracold Heteronuclear Molecules in a 3D Optical Lattice. *Phys. Rev. Lett.*, 97(12):120402, Sept. 2006.

[120] C. Ospelkaus, S. Ospelkaus, K. Sengstock, and K. Bongs. Interaction-Driven Dynamics of ^{40}K-^{87}Rb Fermion-Boson Gas Mixtures in the Large-Particle-Number Limit. *Phys. Rev. Lett.*, 96:020401, Jan 2006.

[121] S. Ospelkaus, C. Ospelkaus, L. Humbert, K. Sengstock, and K. Bongs. Tuning of heteronuclear interactions in a quantum-degenerate Fermi-Bose mixture. *Phys. Rev. Lett.*, 97(12):120403, July 2006.

[122] T. B. Ottenstein, T. Lompe, M. Kohnen, A. N. Wenz, and S. Jochim. Collisional Stability of a Three-Component Degenerate Fermi Gas. *Phys. Rev. Lett.*, 101(20):203202, Nov. 2008.

[123] S. B. Papp and C. E. Wieman. Observation of Heteronuclear Feshbach Molecules from a ^{85}Rb $-^{87}$Rb Gas. *Phys. Rev. Lett.*, 97(18):180404, 2006.

[124] R. Pathria. *Statistical Mechanics*. Elsevier, second edition, 1996.

[125] W. Pauli. Über den zusammenhang des abschlusses der elektronengruppen im atom mit der komplexstruktur der spektren. *Z. Phys.*, 31:765–783, 1925. 10.1007/BF02980631.

[126] W. Petrich, M. H. Anderson, J. R. Ensher, and E. A. Cornell. Stable, tightly confining magnetic trap for evaporative cooling of neutral atoms. *Phys. Rev. Lett.*, 74:3352–3355, Apr 1995.

[127] D. S. Petrov. Three-body problem in fermi gases with short-range interparticle interaction. *Phys. Rev. A*, 67(1):010703, Jan. 2003.

[128] D. S. Petrov. Three-Boson Problem near a Narrow Feshbach Resonance. *Phys. Rev. Lett.*, 93(14):143201, Sept. 2004.

[129] S. E. Pollack, D. Dries, and R. G. Hulet. Universality in three- and four-body bound states of ultracold atoms. *Science*, 326(5960):1683–1685, Dec. 2009.

[130] D. E. Pritchard. Cooling neutral atoms in a magnetic trap for precision spectroscopy. *Phys. Rev. Lett.*, 51:1336–1339, Oct 1983.

[131] C. Raman, R. Onofrio, J. M. Vogels, J. R. Abo-Shaeer, and W. Ketterle. Dissipationless Flow and Superfluidity in Gaseous Bose-Einstein Condensates. *Journal of Low Temperature Physics*, 122:99–116, 2001. 10.1023/A:1004864820016.

[132] C. Regal. *Experimental realization of BCS-BEC crossover physics with a Fermi gas of atoms.* PhD thesis, University of Colorado - Boulder, 2006.

[133] C. Regal and D. Jin. Experimental realization of the bcs-bec crossover with a fermi gas of atoms. volume 54 of *Advances In Atomic, Molecular, and Optical Physics*, pages 1 – 79. Academic Press, 2006.

[134] C. A. Regal, C. Ticknor, J. L. Bohn, and D. S. Jin. Creation of ultracold molecules from a Fermi gas of atoms. *Nature*, 424:47–50, 2003.

[135] J. L. Roberts. *Bose-Einstein Condensates with Tunable Atom-atom Interactions: The First Experiments with ^{85}Rb BECs.* PhD thesis, University of Colorado - Boulder, 2001.

[136] B. P. Ruzic and J. L. Bohn. private communication.

[137] J. J. Sakurai. *Modern Quantum Mechanics.* Addison-Wesley, revised edition, 1994.

[138] R. Schmidt, S. P. Rath, and W. Zwerger. Efimov physics beyond universality. arXiv:1201.4310v3.

[139] F. Schreck, L. Khaykovich, K. L. Corwin, G. Ferrari, T. Bourdel, J. Cubizolles, and C. Salomon. Quasipure Bose-Einstein Condensate Immersed in a Fermi Sea. *Phys. Rev. Lett.*, 87:080403, Aug 2001.

[140] A. Simoni, M. Zaccanti, C. D'Errico, M. Fattori, G. Roati, M. Inguscio, and G. Modugno. Near-threshold model for ultracold krb dimers from interisotope feshbach spectroscopy. *Phys. Rev. A*, 77(5):052705, May 2008.

[141] P. Soldán, M. T. Cvitaš, and J. M. Hutson. Three-body nonadditive forces between spin-polarized alkali-metal atoms. *Phys. Rev. A*, 67(5):054702, May 2003.

[142] F. M. Spiegelhalder, A. Trenkwalder, D. Naik, G. Kerner, E. Wille, G. Hendl, F. Schreck, and R. Grimm. All-optical production of a degenerate mixture of ^{6}Li and ^{40}K and creation of heteronuclear molecules. *Phys. Rev. A*, 81(4):043637, Apr. 2010.

[143] D. A. Steck. Rubidium 87 D Line Data, December 2010. revision 2.1.4.

[144] K. E. Strecker, G. B. Partridge, and R. G. Hulet. Conversion of an Atomic Fermi Gas to a Long-Lived Molecular Bose Gas. *Phys. Rev. Lett.*, 91(8):080406, Aug. 2003.

[145] N. Syassen, D. M. Bauer, M. Lettner, D. Dietze, T. Volz, S. Dürr, and G. Rempe. Atom-molecule rabi oscillations in a mott insulator. *Phys. Rev. Lett.*, 99(3):033201, 2007.

[146] T. Takekoshi, M. Debatin, R. Rameshan, F. Ferlaino, R. Grimm, H.-C. Nägerl, C. R. Le Sueur, J. M. Hutson, P. S. Julienne, S. Kotochigova, and E. Tiemann. Towards the production of ultracold ground-state RbCs molecules: Feshbach resonances, weakly bound states, and the coupled-channel model. *Phys. Rev. A*, 85:032506, Mar 2012.

[147] S. T. Thompson, E. Hodby, and C. E. Wieman. Ultracold molecule production via a resonant oscillating magnetic field. *Phys. Rev. Lett.*, 95(19):190404, 2005.

[148] A. G. Truscott, K. E. Strecker, W. I. McAlexander, G. B. Partridge, and R. G. Hulet. Observation of Fermi Pressure in a Gas of Trapped Atoms. *Science*, 291(5513):2570–2572, 2001.

[149] V. V. Vladimirskii. Magnetic mirrors, channels and bottles for cold neutrons. *Soviet Physics JETP*, 12(4):740–746, 1961.

[150] A.-C. Voigt, M. Taglieber, L. Costa, T. Aoki, W. Wieser, T. W. Hänsch, and K. Dieckmann. Ultracold Heteronuclear Fermi-Fermi Molecules. *Phys. Rev. Lett.*, 102(2):020405, Jan. 2009.

[151] J. von Stecher. Weakly bound cluster states of Efimov character. *J. Phys. B*, 43(10):101002, May 2010.

[152] J. von Stecher. Universal Five- and Six-Body Droplets Tied to an Efimov Trimer. arXiv:1106.2319v1.

[153] J. von Stecher, J. P. D'Incao, and C. H. Greene. Signatures of universal four-body phenomena and their relation to the Efimov effect. *Nature Physics*, 5(6):417–421, Apr. 2009.

[154] V. Vuletić, A. J. Kerman, C. Chin, and S. Chu. Observation of low-field feshbach resonances in collisions of cesium atoms. *Phys. Rev. Lett.*, 82:1406–1409, Feb 1999.

[155] J. Wang, J. P. D'Incao, B. D. Esry, and C. H. Greene. Origin of the Three-body Parameter Universality in Efimov Physics. pages 1–11, arXiv:1201.1176v2.

[156] Y. Wang, J. D'Incao, and B. Esry. Ultracold three-body collisions near narrow Feshbach resonances. *Phys. Rev. A*, 83(4):042710, Apr. 2011.

[157] Y. Wang and C. H. Greene. private communication.

[158] S. Watabe and T. Nikuni. Conversion efficiencies of heteronuclear Feshbach molecules. *Phys. Rev. A*, 77(1):013616, Jan. 2008.

[159] C. Weber, G. Barontini, J. Catani, G. Thalhammer, M. Inguscio, and F. Minardi. Association of ultracold double-species bosonic molecules. *Phys. Rev. A*, 78(6):061601, Dec. 2008.

[160] T. Weber, J. Herbig, M. Mark, H.-C. Nägerl, and R. Grimm. Three-Body Recombination at Large Scattering Lengths in an Ultracold Atomic Gas. *Phys. Rev. Lett.*, 91(12):123201, Sept. 2003.

[161] E. W. Weisstein. "Polylogarithm." From MathWorld–A Wolfram Web Resource., 2012.

[162] E. W. Weisstein. "Spheroid." From MathWorld–A Wolfram Web Resource., 2012.

[163] A. N. Wenz, T. Lompe, T. B. Ottenstein, F. Serwane, G. Zürn, and S. Jochim. Universal trimer in a three-component Fermi gas. *Phys. Rev. A*, 80(4):040702(R), Oct. 2009.

[164] J. E. Williams, N. Nygaard, and C. W. Clark. Theory of Feshbach molecule formation in a dilute gas during a magnetic field ramp. *New J. Phys.*, 8(8):150, Nov. 2006.

[165] J. R. Williams, E. L. Hazlett, J. H. Huckans, R. W. Stites, Y. Zhang, and K. M. O'Hara. Evidence for an Excited-State Efimov Trimer in a Three-Component Fermi Gas. *Phys. Rev. Lett.*, 103(13):130404, Sept. 2009.

[166] W. H. Wing. On neutral particle trapping in quasistatic electromagnetic fields. *Prog. Quant. Electr.*, 8(3-4):181 – 199, 1984.

[167] M. Wouters, J. Tempere, and J. T. Devreese. Resonant dynamics in boson-fermion mixtures. *Phys. Rev. A*, 67(6):063609, June 2003.

[168] C.-H. Wu, J. W. Park, P. Ahmadi, S. Will, and M. W. Zwierlein. Ultracold Fermionic Feshbach Molecules of ^{23}Na^{40}K. arXiv:1206.5023v1.

[169] K. Xu, T. Mukaiyama, J. R. Abo-Shaeer, J. K. Chin, D. E. Miller, and W. Ketterle. Formation of quantum-degenerate sodium molecules. *Phys. Rev. Lett.*, 91(21):210402, Nov. 2003.

[170] M. Zaccanti, B. Deissler, C. D'Errico, M. Fattori, M. Jona-Lasinio, S. Müller, G. Roati, M. Inguscio, and G. Modugno. Observation of an Efimov spectrum in an atomic system. *Nature Physics*, 5(8):586–591, July 2009.

[171] M. Zaccanti, C. D'Errico, F. Ferlaino, G. Roati, M. Inguscio, and G. Modugno. Control of the interaction in a Fermi-Bose mixture. *Phys. Rev. A*, 74(4):041605, Oct. 2006.

[172] C. Zener. Non-adiabatic crossing of energy levels. *Proc. R. Soc. London, Ser. A*, 137(833):696, 1932.

[173] J. Zirbel. *Ultracold Fermionic Feshbach Molecules*. PhD thesis, University of Colorado - Boulder, July 2008.

[174] J. J. Zirbel, K.-K. Ni, S. Ospelkaus, T. L. Nicholson, M. L. Olsen, P. S. Julienne, C. E. Wieman, J. Ye, and D. S. Jin. Heteronuclear molecules in an optical dipole trap. *Phys. Rev. A*, 78(1):013416, 2008.

Appendix A

Myriad details of the SPSS model

In this Appendix we discuss the finer details of our implementation of the SPSS model. We begin in Secs. A.1, A.2, and A.3 with discussion of the Monte Carlo algorithm implemented to generate random Bose-Einstein and Fermi-Dirac distributions in position and momentum space, which are used as the atom distributions inputted into the SPSS model. Following this, we show that the generated distributions do indeed faithfully reproduce the Bose-Einstein or Fermi-Dirac distributions in Sec. A.5. Next we discuss scaling the atom numbers and their effects on the fit of the SPSS to our data in Sec. A.5. Lastly, in Sec. A.6 we discuss signatures of edge-effects in the model and the dependence of simulated molecule conversion fraction on factors other than T/T_c and T/T_F.

A.1   Accept-reject Monte Carlo algorithm

Monte Carlo algorithms are a widely used computation method for calculating probability distributions using random numbers and some knowledge of the desired probability distribution. In the case of the Fermi-Dirac, or Bose-Einstein, probability distribution, we can directly sample the probability distribution, which makes the generation reasonably simple. This process generates a list of particle locations and momenta that has either a Bose-Einstein probability distribution, or a Fermi-Dirac distribution. Our atom generation loops through position space and momentum space volumes (shells to be exact) and the Monte Carlo algorithm decides whether a particle should be placed within a particular shell. This accept-reject algorithm adds a particle at the given location
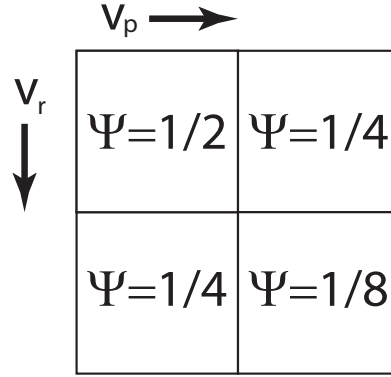
Figure A.1: Boxes in position and momentum whose probability of occupation, Ψ, is shown.

if

$$u \leq \Psi(v_r, v_p) \tag{A.1.1}$$

where u is a pseudo-random number drawn from a uniform distribution whose possible values span 0 to 1, and $\Psi(v_r, v_p)$ is the known probability of a particle existing in the position space volume v_r and momentum space volume v_p (defined in Sec. A.2). Once a particle is added, its location in position and momentum is randomly offset within the position and momentum volume.

To understand why this algorithm can faithfully reproduce the Bose-Einstein or Fermi-Dirac distribution we first focus on the uniform distribution. For this uniform distribution with u $\in [0, 1]$, the conditional probability that a number randomly chosen is less than or equal to a particular value, X, is

$$Prob(u \leq X) = \int_0^X dy = X. \tag{A.1.2}$$

Now, imagine we have a series of boxes whose probability of being populated is known a priori, as shown in Fig. A.1. For the lower right box, we know that that box will be populated 1/8 of the time. Additionally, if we draw a uniform random number whose value $u \leq 1/8$, we also know that the probability of that happening is also 1/8. Therefore, if $u \leq \Psi$, then a particle should be added at that location in position and momentum space. The only restriction is that we must

make small steps in position and momentum space such that the probability of a given box being occupied is $\Psi \ll 1$ in order faithfully reproduce the Bose-Einstein or Fermi-Dirac distribution.

A.2   Fermionic atom generation

This Monte Carlo algorithm requires that we know what the probability is for a fermion existing at a given shell in position and momentum space. To calculate this probability, we begin with the number of fermions as determined by the Fermi-Dirac distribution [124]:

$$N_F = \frac{1}{h^3} \int \cdots \int \frac{1}{z^{-1} e^{(KE+PE)/(k_B T)} + 1} d^3x\, d^3p \qquad \text{(A.2.1)}$$

where h is Planck's constant, z is the fugacity, k_B is Boltzman's constant, and T is the temperature. The kinetic energy (KE) and potential energy (PE) for a harmonically trapped gas is

$$PE = \frac{1}{2} m\, \omega_r^2\, x^2 + \frac{1}{2} m\, \omega_r^2\, y^2 + \frac{1}{2} m\, \omega_z^2\, z^2 \qquad \text{(A.2.2)}$$

$$KE = \frac{p_x^2}{2m} + \frac{p_y^2}{2m} + \frac{p_z^2}{2m} \qquad \text{(A.2.3)}$$

for a particle of mass m. Here we assume that the trap frequencies in the x- and y-direction are given by $\omega_x = \omega_y = \omega_r$ and the trap frequency in the z-direction is ω_z. Next, we make the following coordinate system change

$$\sqrt{\frac{m\omega_r^2}{2k_B T}}\, x = X \qquad \sqrt{\frac{m\omega_r^2}{2k_B T}}\, y = Y \qquad \sqrt{\frac{m\omega_r^2}{2k_B T}}\, \lambda z = Z$$

$$\sqrt{\frac{1}{2mk_B T}}\, p_x = P_x \qquad \sqrt{\frac{1}{2mk_B T}}\, p_y = P_y \qquad \sqrt{\frac{1}{2mk_B T}}\, p_z = P_z$$

where $\lambda = \omega_z/\omega_r$, and then the fermion number is

$$N_F = \frac{1}{h^3} \left(\frac{2k_B T}{m\omega_r^2} \right)^{3/2} (2mk_B T)^{3/2} \int \cdots \int \frac{1}{z^{-1} e^{X^2+Y^2+Z^2+P_x^2+P_y^2+P_z^2} + 1} d^3X\, d^3P$$

$$= \frac{(4\pi)^2}{h^3} \left(\frac{2k_B T}{\omega_r^2} \right)^3 \frac{1}{\lambda} \int_0^\infty \int_0^\infty \frac{R^2 P^2}{z^{-1} e^{P^2+R^2} + 1} dR\, dP \qquad \text{(A.2.4)}$$

where in the last line we have change to spherical coordinates with $R^2 = X^2 + Y^2 + Z^2$, $P^2 = P_x^2 + P_y^2 + P_z^2$ and evaluated the angular integral, which yielded the $(4\pi)^2$ factor. The probability,

Ψ, of a fermion existing at a given value of R and P within a 6-d shell of thickness $\Delta R \Delta P$ is determined by the integrand of the previous equation:

$$\Psi = \frac{16\pi^2}{h^3} \left(\frac{2k_BT}{\omega_r} \right)^3 \frac{1}{\lambda} \frac{R^2P^2}{z^{-1}e^{P^2+R^2}+1} \Delta R\, \Delta P. \tag{A.2.5}$$

We prefer to express Ψ in terms of $\mathrm{T}/\mathrm{T_F}$ and atom number. The fermion atom number integrals can be solved analytically when rewritten in terms of density of states and energies. The number of fermions relates to the Fermi temperature by:

$$N_F = \frac{1}{6} \left(\frac{k_B\mathrm{T_F}}{\hbar\omega_r} \right)^3 \frac{1}{\lambda} \tag{A.2.6}$$

If we use this to rewrite our expression for Ψ, we arrive at the expression used in the Monte Carlo after a few steps:

$$\begin{aligned}
\Psi &= \frac{N_F}{N_F} \frac{16\pi^2}{h^3} \left(\frac{2k_BT}{\omega_r} \right)^3 \frac{1}{\lambda} \frac{R^2P^2}{z^{-1}e^{P^2+R^2}+1} \Delta R\Delta P \\
&= N_F \frac{\frac{16\pi^2}{h^3} \left(\frac{2k_BT}{\omega_r} \right)^3 \frac{1}{\lambda}}{\frac{1}{6} \left(\frac{k_B\mathrm{T_F}}{\hbar\omega_r} \right)^3 \frac{1}{\lambda}} \frac{R^2P^2}{z^{-1}e^{P^2+R^2}+1} \Delta R\Delta P \\
&= N_F \frac{96}{\pi} \left(\frac{T}{T_F} \right)^3 \frac{R^2P^2}{z^{-1}e^{P^2+R^2}+1} \Delta R\Delta P.
\end{aligned} \tag{A.2.7}$$

where in the Monte Carlo code, the parameter $T1 = \mathrm{T}/\mathrm{T_F}$. The volume variables that the code loops over are defined as:

$$v_r = \frac{1}{3}R^3 \qquad\qquad v_p = \frac{1}{3}P^3 \tag{A.2.8}$$

$$\Delta v_r = R^2\Delta R \qquad\qquad \Delta v_p = P^2\Delta P \tag{A.2.9}$$

where the last line is the volume of the position space and momentum space shells.

Finally, we'd like to have a sensible way to set the step size in phase-space such that we avoid the situation where our step size is large enough to have allowed for multiple particles. In fact we would actually prefer to have the maximum probability, $max_p \ll 1$ such that the Monte Carlo algorithm more faithfully reproduces the Fermi-Dirac distribution[1] . If we let $R = P$, we can find

---

[1] A value of $max_p = 0.05$ is sufficient for most calculations with fermions or bosons.

the maximum with the following:

$$\frac{d}{dP}\frac{P^4}{z^{-1}e^{2P^2}+1} = \frac{4P^3 z\left(z - e^{2P^2}(P^2-1)\right)}{\left(e^{2P^2}+z\right)^2} = 0$$

$$\Rightarrow \left(z - e^{2P^2}(P^2-1)\right) = 0.$$

The value of P which maximizes the probability depends roughly on z as $\sqrt{\ln z}$ and varies between $P = 1$ for $z = 0$ and $P \approx 7$ for $z = 2.6 \times 10^{43}(\mathrm{T}/\mathrm{T_F} = 0.01)$. So, we arbitrarily chose to set $P = 1$ and arrive at an expression for max_p

$$max_p = N_F \frac{96}{\pi}\left(\frac{T}{T_F}\right)^3 \frac{1}{z^{-1}e^2+1}\Delta R\Delta P \tag{A.2.10}$$

Solving for the shell thickness $\Delta R\Delta P$ gives the step size (in v_r and v_p) for the algorithm as

$$(\text{step size})^2 = \Delta R\Delta P = \frac{max_p}{N_F}\frac{\pi}{96}\left(\frac{T}{T_F}\right)^{-3}(z^{-1}e^2+1). \tag{A.2.11}$$

A.3   Bosonic atom generation

The derivation for the boson algorithm expressions follows a similar logic as the fermions. The number of bosons can be calculated from the Bose-Einstein distributions, which yields

$$N_B = \frac{1}{h^3}\int\cdots\int \frac{1}{z^{-1}e^{(KE+PE)/(k_BT)}-1}d^3x\,d^3p$$
$$= \frac{(4\pi)^2}{h^3}\left(\frac{2k_BT}{\omega_r^2}\right)^3\frac{1}{\lambda}\int_0^\infty\int_0^\infty \frac{R^2P^2}{z^{-1}e^{P^2+R^2}-1}dR\,dP \tag{A.3.1}$$

after making the same coordinate system change as in the fermionic case. The probability of a given shell in position and momentum space is then

$$\Psi = \frac{16\pi^2}{h^3}\left(\frac{2k_BT}{\omega_r}\right)^3\frac{1}{\lambda}\frac{R^2P^2}{z^{-1}e^{P^2+R^2}-1}\Delta R\,\Delta P. \tag{A.3.2}$$

Using the definition of T_c, we can rewrite Ψ in terms of N_B and T/T_c, which yields

$$\Psi = N_B\frac{16}{\pi\zeta(3)}\left(\frac{T}{T_c}\right)^3\frac{R^2P^2}{z^{-1}e^{P^2+R^2}-1}\Delta R\,\Delta P, \tag{A.3.3}$$

where ζ is the Riemann zeta function, for which $\zeta(3) \approx 1.20206$.

(a) Spatial density distribution

(b) Momentum distribution

(c) Spatial density residual
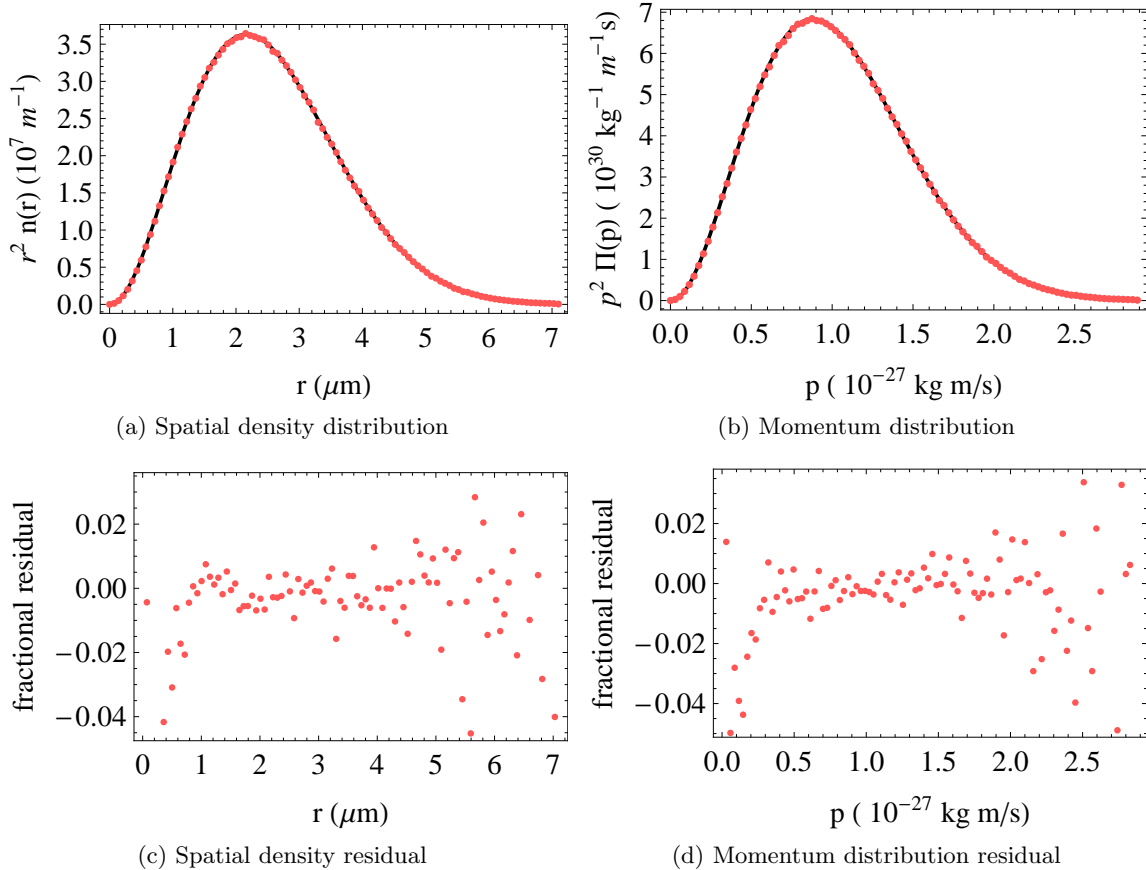
(d) Momentum distribution residual

Figure A.2: Comparison of a Bose distribution generated with the Monte Carlo (red points) with the ideal Bose gas distribution (black curve). The distributions were generate for $N_{boson} = 10^5$ and $T/T_c = 1.05$ for a harmonic trap with radial trap frequency $\omega_r = 2\pi\,448$ Hz and trap aspect ratio $\lambda = 0.013$. The momentum and spatial density distributions are the result 24 runs of the Monte Carlo simulation with $max_p = 0.05$. c) and d) Fractional residuals for a) and b), respectively, where the fractional residual is defined as the Monte Carlo result divided by Eqn. (A.4.1) or (A.4.2) minus 1.

Following the analysis of the fermionic case, the step size for loops in the Monte Carlo algorithm is then:

$$(\text{step size})^2 = \Delta R \Delta P = \frac{max_p}{N_B} \frac{\pi \zeta(3)}{16} \left(\frac{T}{T_C}\right)^{-3} (z^{-1}e^2 - 1). \qquad (A.3.4)$$

A.4   Verifying Monte Carlo atom density and momentum distributions

Before the SPSS model can be applied, an ensemble of atoms with the correct density and momentum distributions is generated. To demonstrate that our Monte Carlo code produces dis-

tributions that, on average, agree with either the Bose-Einstein or Fermi-Dirac distribution, we average an ensemble of Monte Carlo distributions and compare with the ideal distributions. In Figs. A.2 and A.3 the Monte Carlo spatial (solid circles) and momentum (open circles) density distributions are shown for the Bose and Fermi gas simulations, respectively. We also plot the harmonically trapped ideal Bose and Fermi gas spatial and momentum density distributions. The harmonically trapped Bose gas spatial[2] $(n_{\mathrm{Boson}}(r))$ and momentum densities $(\Pi_{\mathrm{Boson}}(p))$ are given by

$$n_{\mathrm{boson}}(r) = \frac{\lambda N}{(2\pi)^{3/2}\sigma_r^3} Li_{3/2}\left(ze^{-r^2/2\sigma_r^2}\right)/Li_3(z) \tag{A.4.1}$$

$$\Pi_{\mathrm{boson}}(p) = \frac{N}{(2\pi)^{3/2}\sigma_p^3} Li_{3/2}\left(ze^{-p^2/2\sigma_p^2}\right)/Li_3(z) \tag{A.4.2}$$

where z is the fugacity, $Li_n(z)$ is the polylogarithm function[3] , $\sigma_r^2 = \dfrac{k_B T}{m\omega_r^2}$ for atomic mass m, $\sigma_p^2 = mk_B T$, and $r^2 = x^2 + y^2 + \lambda^2 z^2$. Similarly for a harmonically trapped fermions, the spatial and momentum densities are

$$n_{\mathrm{fermion}}(r) = \frac{\lambda N}{(2\pi)^{3/2}\sigma_r^3} Li_{3/2}\left(-ze^{-r^2/2\sigma_r^2}\right)/Li_3(-z) \tag{A.4.3}$$

$$\Pi_{\mathrm{fermion}}(p) = \frac{N}{(2\pi)^{3/2}\sigma_p^3} Li_{3/2}\left(-ze^{-p^2/2\sigma_p^2}\right)/Li_3(-z). \tag{A.4.4}$$

The plots of Eqn. (A.4.1) and Eqn. (A.4.2) for Bosons and Eqn. (A.4.3) and Eqn. (A.4.4) for Fermions used the same harmonic trap parameters and fugacities as with the Monte-Carlo calculation. The Monte-Carlo distributions were generated for a 'cigar-shaped' harmonic trap with an aspect ratio of $\lambda = = 0.013$, where ω_z is the axial trap frequency, and with radial trap frequency $\omega_r = 2\pi$ 448 Hz and 627 Hz for the bosons and fermions, respectively. For both the boson and fermion distribution, approximately 10^5 atoms were generated at a moderately high degeneracy (T/T$_c$ = 1.05, T/T$_F$ = 0.11) in order to look for any problems with undersampling. The

---

[2] These densities are found by integrating the right-hand side of Eqn. A.3.1 over just momentum to calculate $n_{\mathrm{Boson}}(r)$ or just position to calculate $\Pi_{\mathrm{Boson}}(p)$.

[3] The polylogarithm is related to the Bose-Einstein integrals on the right-hand side of Eqn. A.3.1 by [161] $\int_0^\infty \dfrac{k^s dk}{z^{-1}e^k - 1} = \Gamma(s+1) Li_{1+s}(z)$, where $\Gamma(z)$ is the gamma function. The relation for the integrals on the right-hand side of Eqn. A.2.1 by $\int_0^\infty \dfrac{k^s dk}{z^{-1}e^k + 1} = -\Gamma(s+1) Li_{1+s}(-z)$.
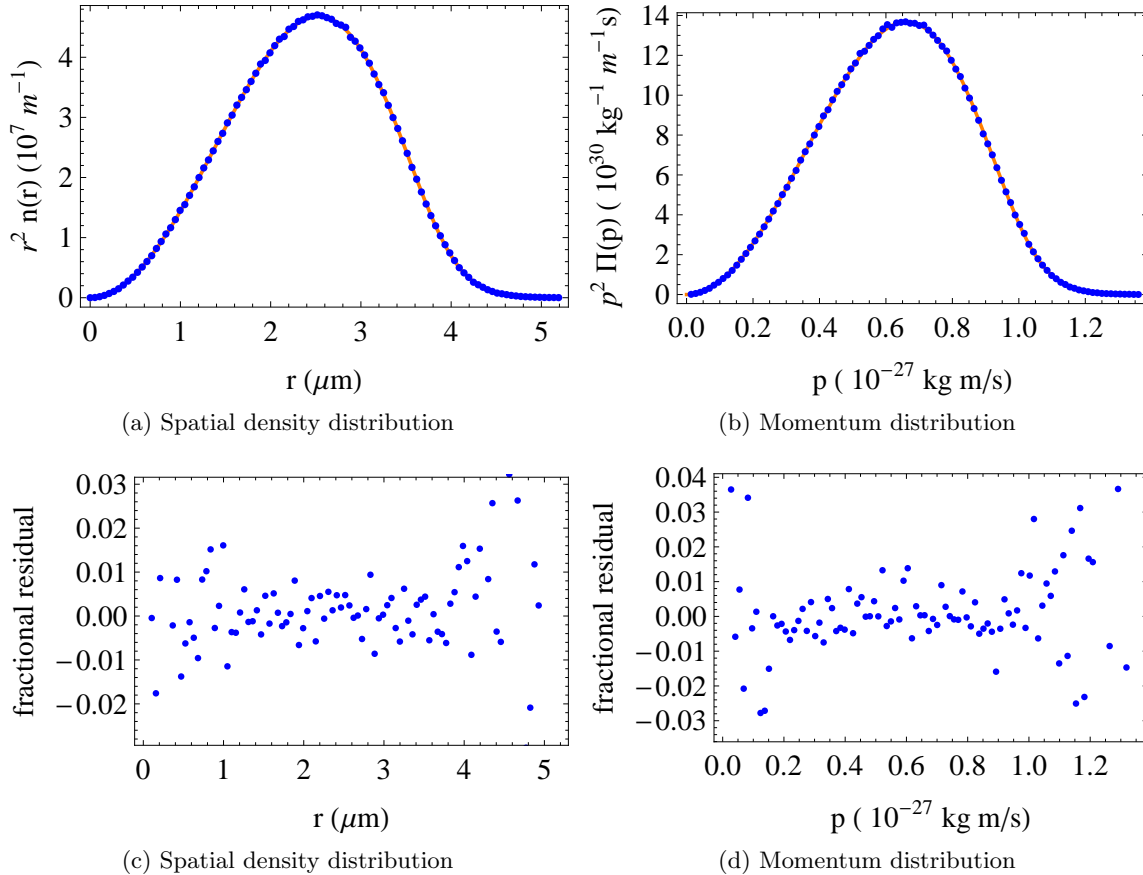
Figure A.3: Comparison of a Fermi distribution generated with the Monte Carlo (blue points) with the ideal Fermi gas distribution (gray curve). The distributions were generate for $N_{fermion} = 10^5$ and $T/T_F = 0.11$ for a harmonic trap with radial trap frequency $\omega_r = 2\pi\,627$ Hz and trap aspect ratio $\lambda = 0.013$. The momentum and spatial density distributions are the average of 24 runs of the Monte Carlo simulation with $max_p = 0.05$. c) and d) Fractional residuals for a) and b), respectively.

excellent agreement between the Monte-Carlo results and the ideal Bose and Fermi gas distributions indicates that the Monte-Carlo simulation reproduces the appropriate distributions faithfully.

An additional check of the distributions generated by the Monto-Carlo code is to check that the Virial theorem is upheld. The Virial theorem is a relation between the average kinetic energy of a sample and the forces acting on each particle in the system. Classical systems, as well as quantum mechanical systems, follow the Virial theorem. The Virial theorem is given by [124]

$$\left\langle \sum_i r_i \dot{p}_i \right\rangle = -2\left\langle K \right\rangle, \tag{A.4.5}$$

where the brackets represent an ensemble average, K is the kinetic energy, and $\dot{p}_i$ is the time-

derivative of the momentum of particle i at the position r_i. If the particles are assumed to be non-interacting and trapped in a potential of the form $U(r) = A\,r^n$ (A is a constant), then the Virial theorem simplifies to

$$n \; \langle U \rangle \; = \; 2 \; \langle K \rangle, \qquad\qquad (A.4.6)$$

where $\langle U \rangle$ is the ensemble average potential. This result simplifies to $\langle U \rangle = \langle K \rangle$ for the harmonically trapped case (n=2).

To test that the Virial theorem is obeyed, twenty distributions were generated by the Monte-Carlo over a range of temperatures for both bosons and fermions and the average potential and kinetic energies were computed. The results are plotted in Fig. A.4, where the error bars are the standard errors of the mean of the twenty distributions for each temperature. The good agreement with the Virial theorem provides further evidence that the distributions generated by the Monte-Carlo are faithfully reproducing the ideal Fermi and Bose distributions.
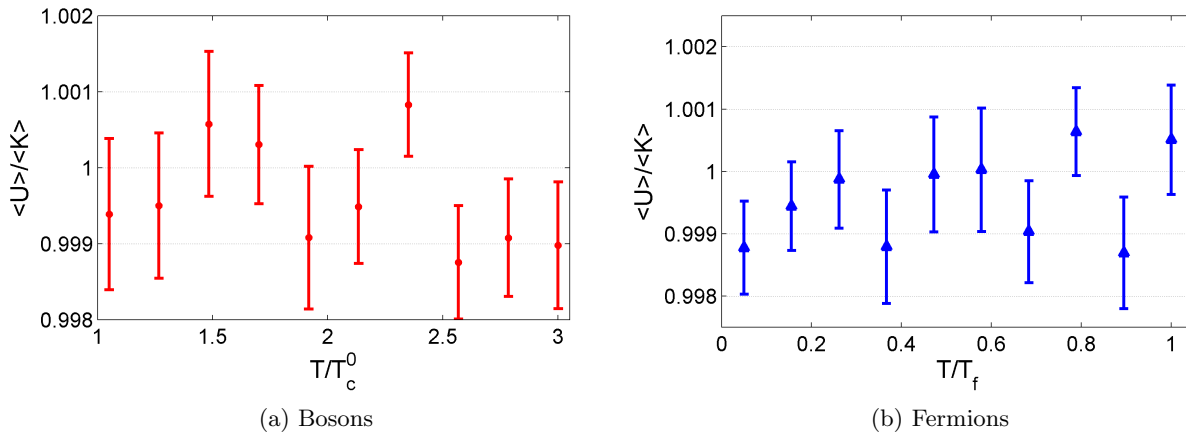

(a) Bosons

(b) Fermions

Figure A.4: Checking the Virial theorem for Bose and Fermi distributions generated by the Monte-Carlo code. Each point is an average of the ratio $\langle U \rangle / \langle K \rangle$ for twenty distributions at a given temperature. The error bars at the standard error of the mean.

A.5   Fitting the SPSS model

Fitting the SPSS model to atom data where the atom numbers are of order 10^5 to 10^6 is a computationally intensive process. One way to speed up the fitting process is to scale the

atom number down in a sensible fashion such that the T/T_F (or T/T_c) axis is preserved. From Eqn. (2.5.1) $T_c \propto \bar{\omega} N^{1/3}$, where $\bar{\omega} = (\omega_r^2 \omega_z)^{1/3}$ for radial and axial trap frequencies, ω_r and ω_z. The Fermi temperature also has the same dependence on atom number and trap frequency: $T_F \propto \bar{\omega} N^{1/3}$. One scaling method is to scale the atom number and trap frequencies (with fixed aspect ratio $\lambda = \omega_z/\omega_r$) such that $\bar{\omega} N^{1/3}$ is fixed and fix the temperature, as well. The results of this scaling method is shown in Fig. A.5a where the model was fit to the data in Fig. 3.8 for the value of γ from Eqn. (3.5.1) using a range of scaling factors. The solid horizontal lines are the fit results for $^{85}Rb_2$ molecules (upper solid line) and $^{40}K_2$ molecules (lower solid line) from Ref. [75]. As can be seen, the fitted value of γ depends strongly on the value of the scaling factor and therefore scaling the problem in this manner would require corrections to account for the sensitivity to the scaling factor.

An alternative method is to scale the aspect ratio, λ, with the atom number such that $T_F \propto \bar{\omega} N^{1/3} = \omega_r (\lambda N)^{1/3}$ is fixed. This method, in addition to fixing T/T_F and T/T_c also fixes the rms radial cloud size. The results of this scaling method are shown in Fig. A.5b as a function of the scaling factor. For this figure, a scaling factor of 1 corresponds to $\lambda = 0.013$, which describes a prolate spheroid ($\lambda < 1$). As can be seen, this results for γ from the fits asymptotically approach a constant value for low values of the scaling parameter corresponding to prolate spheroids. Additionally, the deviation from the zero scaling factor limit is small upto where the simulation corresponds to a spherical atom cloud (vertical dashed line where $\lambda = 1$). This means that we can reduce the atom number in the simulation by a factor of $1/0.013 = 77$, which will decrease the simulation time by[4] 77^2 without a substantial loss in accuracy.

A.6   Other details of the SPSS model

While the scaling of λ and N provides a substantially better way to scale the model than the method described previously, it may also be a signature of edge effects in the model where atoms at the edges of the cloud are associated at a different efficiency compared to the bulk. If we consider

---

[4] The molecule association algorithm, which is the part of the simulation of longest duration, scales as N^2.
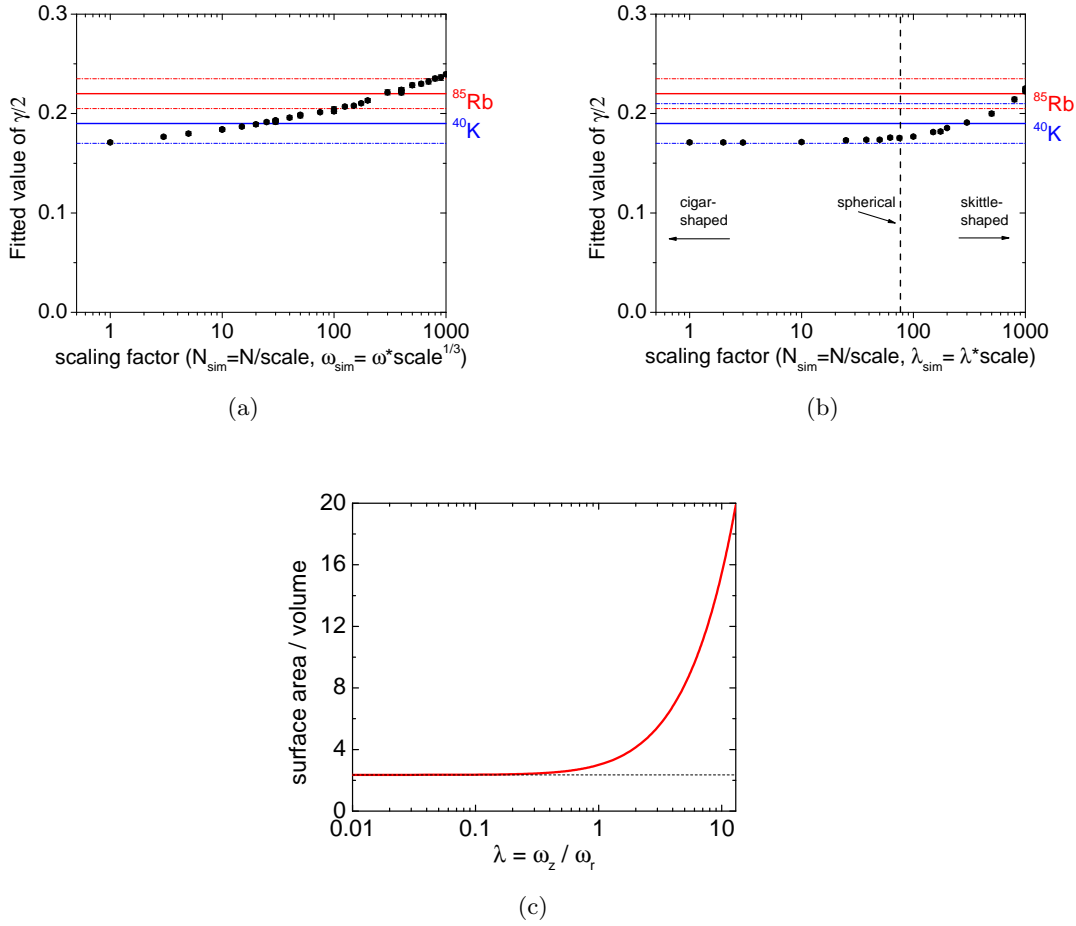
Figure A.5: a) Fitting results where the system was scaled such that the product $\omega^3 N$ was kept constant. b) Fitting results for the model where the system was scaled such that the product $N\lambda$ was kept constant. The vertical dashed line indicates where the aspect ratio $\lambda = 1$. c) Surface area to volume ratio for a spheroid.

the case of constant density, n, distributed throughout a volume, then the number of atoms on the surface at a radius R is $N_S = SA(R) \, n \, dR$, where SA is the surface area and dR is the differential thickness of the surface. The number of atoms in the volume, V, is simply $N_V = n \, V$ and so the ratio $N_S/N_V \propto SA/V$. The surface area to volume ratio tells us the the number of molecules on the edges of the cloud compared to the bulk. In Fig. A.5c the surface area to volume ratio for a spheroid is shown as a function[5] of λ for a fixed radial size of one, and therefore radial trap

---

[5] The trap frequency aspect ratio λ is related to the axial and radial cloud sizes (σ_z and σ_r, respectively) by $\lambda = \sigma_r/\sigma_z$.
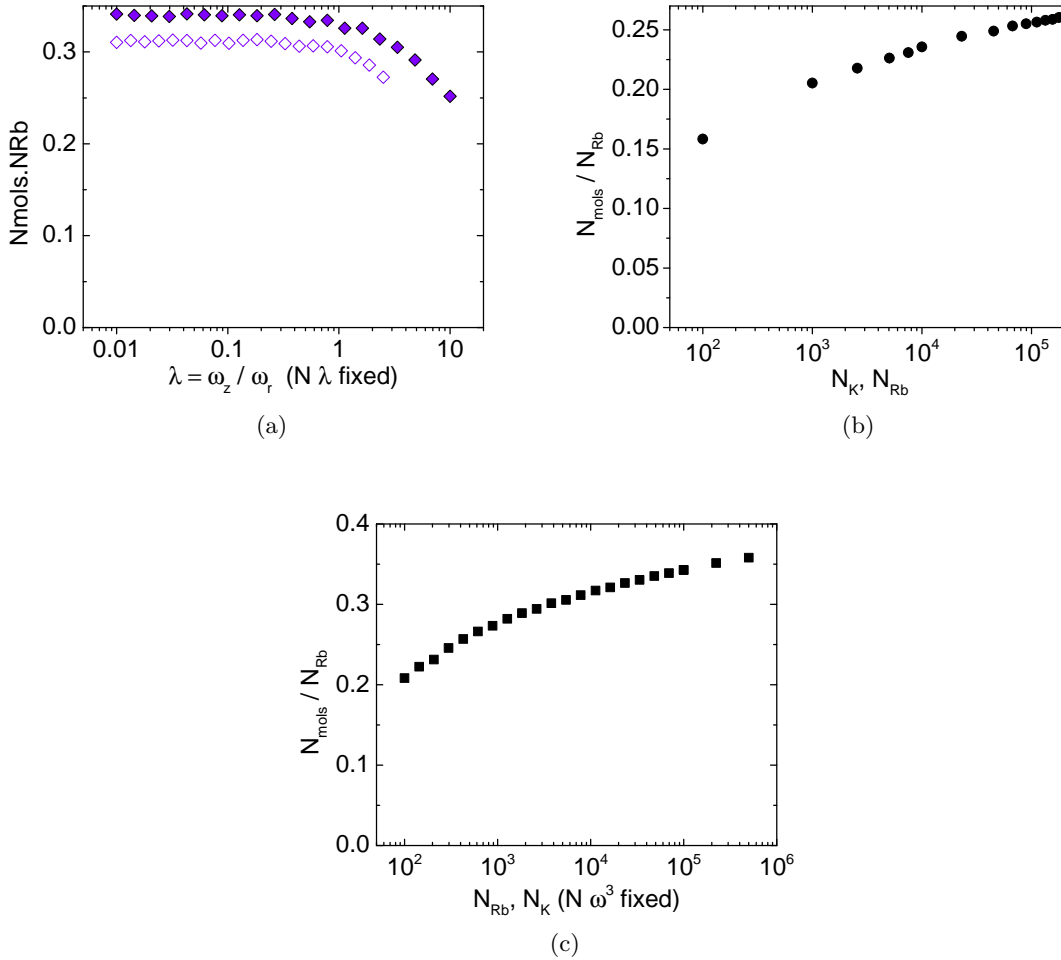
Figure A.6: a) Simulated molecule fraction calculated by varying N and λ such that the product $N\lambda$ was fixed. b) Molecule fraction calculated by varying the atom number with all other input parameters fixed. c) Attempt to calculate the molecule fraction in the thermodynamic limit where $N \to \infty$, $\omega \to 0$, but $N\omega^3$ is constant.

frequency, from equations in Ref. [162].

Shown in Fig. A.6a is the simulated molecule creation fraction where the atom number, N, and λ was varied with the product $N\lambda$ fixed for $\gamma = 0.34$. For this simulation $N_K = N_{Rb}$, $T/T_c = 1.05$, $T/T_F = 0.54$, and the radial trap frequencies were 627 Hz for K and 448 Hz for Rb. As a consequence of all these fixed parameters, the atom temperatures in this simulation is also fixed, as well as the radial cloud sizes. In this figure the solid points have the $N\lambda$ product for which $\lambda = 0.01$ corresponds to $N = 10^5$; for the hollow points $\lambda = 0.01$ corresponds to $N = 10^4$. This

model predicts, in addition to the dependence on T/T_c and T/T_F, that the molecule conversion efficiency also depends on the aspect ratio of the trap. Additionally, the model predicts that the molecule fraction also depends on the atom number even for fixed ratio of Rb to K atoms, as can be seen from Fig. A.6a, as well as in Fig. A.6b where the molecule fraction was computed for variable atom number ($N_K = N_{Rb}$) and fixed trap frequencies, $\lambda = 0.013$, T/T_F, and T/T_c. While the atom number in our data range from several 10^4 to a few 10^5 and thus the size of this effect is below our number noise, it is a bit disconcerting that the model predicts a molecule fraction that strictly increases with atom number. If we examine the thermodynamic limit to address the number dependence concern ($N \to \infty, N\omega^3 = $ const, i.e. a fixed average density but increasing system size) for fixed T/T_c and T/T_F, we find that the molecule fraction does not reach an asymptotic value for atom numbers up to $N_K = N_{Rb} = 5 \times 10^5$, as shown in Fig. A.6c. From a theoretical stand-point this is a bit alarming, but perhaps over a narrow range of conditions it is not too terrible of an approximation.